2007

APPLICATIONS OF MULTIWALL CARBON NANOTUBE COMPOSITES: MECHANICAL, ELECTRICAL AND THERMAL PROPERTIES

Matthew Collins Weisenberger
University of Kentucky, matt@caer.uky.edu

ABSTRACT OF DISSERTATION

Matthew Collins Weisenberger

The Graduate School

University of Kentucky

2007

APPLICATIONS OF MULTIWALL CARBON NANOTUBE COMPOSITES:
MECHANICAL, ELECTRICAL AND THERMAL PROPERTIES

ABSTRACT OF DISSERTATION

A dissertation submitted in partial fulfillment of the
requirements for the degree of Doctor of Philosophy in the
College of Engineering at the University of Kentucky

By
Matthew Collins Weisenberger

Lexington, Kentucky

Director: Dr. Eric Grulke, Professor of Chemical and Materials Engineering

Lexington, Kentucky

2007

ABSTRACT OF DISSERTATION

APPLICATIONS OF MULTIWALL CARBON NANOTUBE COMPOSITES:
MECHANICAL, ELECTRICAL AND THERMAL PROPERTIES

Carbon nanotubes have now been a subject of intense research for approaching two decades. Although a short time relative to most conventional materials, much hype about the intrinsic properties of this material has now been substantiated by experiment. The results are conclusive that carbon nanotubes are truly phenomenal materials with highly desirable mechanical, electrical and thermal properties. Furthermore, multiwall carbon nanotubes (MWNTs) have emerged as the most economically viable and abundant form of carbon nanotubes, and therefore the most likely candidate for application. The key materials engineering challenge remains in effectively transferring their properties to macro-scale materials in the form of composites. It is here that research merges with application. This dissertation has therefore been directed to focus on carbon nanotube composites in an applied sense. Here, the state of the art is reviewed, and experimental results of carefully selected composite systems, studied in detail for (1) mechanical, (2) electrical and (3) thermal properties, are presented and discussed. In terms of mechanical properties, the effects of MWNTs for augmentation of the tensile properties of PAN-based carbon fiber, and fatigue performance of poly(methyl methacrylate) are investigated and reported. In MWNT composite PAN-based carbon fiber, the formation of an ordered interphase layer sheathing the nanotubes was observed in fracture surfaces, which indicated a clear importance of their function to template the growth of carbon formation in the PAN-based matrix fiber. These structures open up a route to nano-scale tailorability of the crystallographic morphology of the composite fibers. Large improvements in fatigue performance were observed in MWNT/PMMA composites compared to MWNT/chopped carbon fiber composites, and attributed to the nanometer scale dimensions of the MWNTs enabling them to mitigate submicron damage such as polymer crazing. In terms of electrical and thermal properties, MWNT/epoxy composites were superior to MWNT/carbon black composites. Furthermore, extremely large improvements in the thermal conductivity of epoxy were observed for epoxy-infiltrated aligned MWNT arrays. The alignment of the MWNTs was shown to play a dominant role in enabling the improvement. Finally, these results, in concert with the literature are discussed in terms of the application of carbon nanotubes in engineering materials.

_____Matthew C. Weisenberger_____

_____November 26, 2007_____

APPLICATIONS OF MULTIWALL CARBON NANOTUBE COMPOSITES:
MECHANICAL, ELECTRICAL AND THERMAL PROPERTIES

By

Matthew Collins Weisenberger

_____Dr. Eric Grulke_____
(Director of Dissertation)

_____Dr. Douglass Kalika_____
(Director of Graduate Studies)

_____November 26, 2007_____

RULES FOR THE USE OF DISSERTATIONS

<u>Name</u>   <u>Date</u>

_____

_____

_____

_____

_____

_____

_____

_____

DISSERTATION

Matthew Collins Weisenberger

The Graduate School

University of Kentucky

2007

APPLICATIONS OF MULTIWALL CARBON NANOTUBE COMPOSITES:
MECHANICAL, ELECTRICAL AND THERMAL PROPERTIES

DISSERTATION

A dissertation submitted in partial fulfillment of the
requirements for the degree of Doctor of Philosophy in the
College of Engineering at the University of Kentucky

By
Matthew Collins Weisenberger

Lexington, Kentucky

Director: Dr. Eric Grulke, Professor of Chemical and Materials Engineering

Lexington, Kentucky

2007

for Nana

ACKNOWLEDMENTS

TABLE OF CONTENTS

LIST OF TABLES

LIST OF FIGURES

LIST OF FILES

File 1: Dissertation-MWeisenberger.pdf

1.1 Introduction

Incorporating carbon nanotubes into polymeric matrices to form carbon nanotube (CNT) composite materials is an area of significant scientific interest, and a topic of numerous research programs. The universal goal is quite simple: develop CNT composites that out-perform current materials. It is a goal that is both motivated and taunted by the incredible properties of carbon nanotubes. The motivation lies in the fact that CNTs are incredibly strong, stiff, and tough, while simultaneously being excellent conductors of electricity and heat. With a low density and a high aspect ratio, they represent the ultimate multifunctional material. Their industrial application as advanced additives in polymeric composites is highly anticipated. The taunting lies in the fact that, although CNTs can now be produced in large quantities relatively inexpensively, translation of their properties to practical size composite materials with proportionate increases in properties has been challenging. However, great strides forward are happening, and the literature continues to report an ever-increasing array of CNT composite applications. Throughout this chapter, from processing to properties, the fundamentals of CNT composites will be explored. Particular emphasis will be given to experimentally measured properties of CNT composites.

Carbon nanotubes*[1, 2]* have been the subject of intense investigation in both fundamental and applied sciences*[3]*. Using single crystal graphite and fullerenes as a starting point, great strides have been made in understanding the properties of these materials at the nano-scale: the nature by which they transport electrons*[4, 5]*, and heat*[6, 7]*, and how they respond to applied forces and fields*[8, 9]*. Results of these computations and experiments have demonstrated truly remarkable properties, and have placed CNTs at the forefront of nanotechnology development. Apart the spectacular mechanical, electrical, and thermal properties (Table 1.1), it is simply the nanometer size-scale of CNTs that is fundamentally interesting. The surface area per volume of these nano-scale materials is much higher than typical micron-scale materials. In the case of carbon fibers versus carbon nanotubes, this effect is a strong function of decreasing CNT diameter, as shown in Figure 1-1. For CNTs, high surface area to volume ratios coupled with large aspect ratios are fundamental motivators for fabricating high performance composites. The former equates to enhanced area of interface available for interaction with the surrounding contiguous matrix. The latter, predominantly a geometric consideration, is ideally suited for stress transfer and internal network formation for electron and heat transport. Here, intrinsic properties, interfacial area and geometry team up to ideally suit the sorts of applications in which CNT-polymer composites are envisioned: as mechanically reinforced, and as electrically and thermally conductive polymer composites. Furthermore, the small size of CNTs enables them to be dispersed into polymeric fluids allowing for simple bulk processing.

With this regard, transferring the unique properties of CNTs to macro-scale composites has proven to be a complex issue. It is a multi-faceted problem in which a number of factors must be considered, including: CNT purity, diameter, length, orientation,

concentration, interfacial adhesion, crystalline defects and dispersion. Understanding how these factors affect composite properties will enable their optimization. These issues will be discussed within the scope of the recent literature, highlighting the state of CNT-polymer composites.
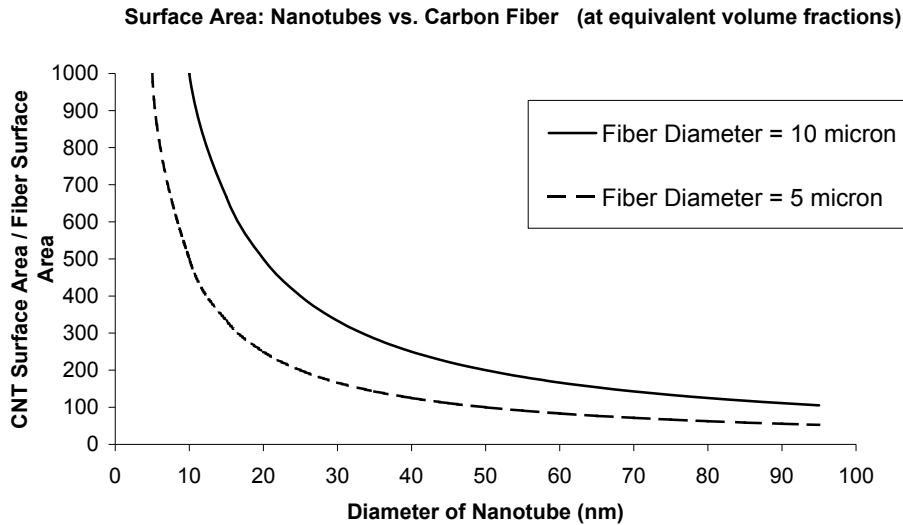
Figure 1-1 CNT surface area
Increases in the ratio of CNT surface area to carbon fiber surface area as a function of the CNT diameter at identical volume fractions. Two typical carbon fiber diameters are compared.
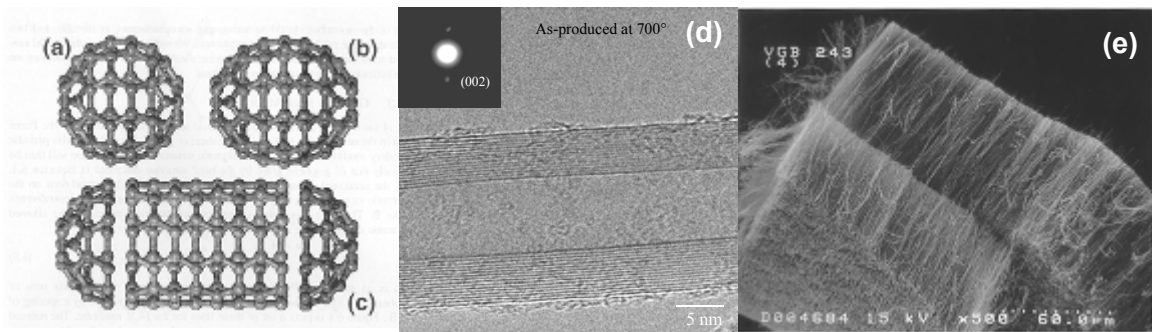
Figure 1-2 Fullerenes, SWNTs and MWNTs
Closed cage carbon fullerenes are shown in a) C60 and b) C70 c) 'Extended' C60 forming a single wall carbon nanotube (SWNT) d) High resolution TEM imaging of a multiwall carbon nanotube (MWNT) shows the lattice fringes of the concentrically nested shells of carbon. e) Low magnification SEM imaging of carpets of aligned MWNTs.

Carbon Nanotubes: Properties and Types

The structure and properties of CNTs can be approached in many ways. Chemists and physicists may prefer to think of CNTs as linearly extended fullerenes. In fact, the most ideal carbon nanotube, a perfect, isolated single wall carbon nanotube (SWNT) is exactly that (Figure 1-2). But CNTs, at a less magnified scale, are not so simple, and tend to form in a range of morphologies from bundles of SWNTs*[10]*, carpets of multiwall

2

nanotubes (MWNT)*[11]* (MWNTs are concentrically nested SWNTs), to less-fullerene-like morphologies including carbon nanofibers (CNFs) approaching micron diameter vapor grown carbon fibers*[12]*.

CNTs are synthesized by various methods including electric arc discharge*[1]*, laser ablation*[13]*, and chemical vapor deposition*[1, 8, 11, 14]*, each yielding nanotubes with various characteristics such as diameter, defect density, length, and self-entanglement. Just as different types of carbon fibers yield different composite properties, different CNT types yield varying CNT composite properties. Typical reported properties of various CNT types are listed in Table 1.1. It must be acknowledged that CNTs, like oriented graphite, are very anisotropic materials. Their most impressive properties correspond along the direction parallel to the nanotube axis.

Table 1.1 On-axis properties of CNTs and graphitic materials.

Material Type	Young's Modulus (GPa)	Break Stress (GPa)	Strain to Failure (%)	Electrical Conductivity (S/cm)	Thermal Conductivity (W/mK)
SWNT	**1250 ± 400**[15] **~1000**[16]	**~100**[17] **10-52**[18]	**10 -15** [19] **5.3** [18]	**10-200**[20] **10^3**[5]	**3000 -6000** [21]
SWNT Bundle	**1250**[22]	**> 45 ± 7** [22]	**1-6** [22]		
MWNT	**1800 ± 900**[23] **270 – 950**[24] **910** [25]	**11-63**[24] **150**[25] **109**[26]	**5 -12** [24, 25, 27]	**10^3** [5, 28, 29]	**600** [30] **650 - 830**[31]
Carbon Nanofiber	**~100**[32] **400**[33]	**2.7**[33]	**~ 1** [33]		
Graphite Whisker	**700 – 1000** [34]	**19.6**[34]	**~ 2** [34]		**940-2000**[35]
High Strength Carbon Fiber	**220 – 580** [36, 37]	**4.3 – 6.4** [36, 37]	**1.5 – 2.2** [36, 37]	**550**[38]	**8**[38]

The high strain to failure of nanotubes allows for very high break strengths.
Selected experimental mechanical testing methods reported for CNTs:
[23] In-situ TEM imaging of thermal vibrations of cantilevered MWNTs
[15] In-situ TEM imaging of thermal vibrations of cantilevered SWNTs
[25] In-situ TEM tensile testing of MWNTs
[18, 24] In-situ SEM tensile testing of SWNTs and MWNTs

1.2 Processing

Dispersing Carbon Nanotubes

Materials scientists interested in using CNTs in composites often consider CNTs essentially as ultra-fine, high aspect ratio, discontinuous carbon fibers. In light of as-

synthesized CNT morphologies, a primary objective in fabricating CNT composites is separating or dispersing the CNTs such that they can be *individually* loaded or form a conducting network in a polymer composite. Bundled SWNTs due to relatively strong inter-tube Van der Waals attractive forces, and entangled or "birds nest" MWNTs, a result of synthesis, are difficult to individually disperse into matrices[39]. Aligned, non-entangled MWNTs grown on substrates are more easily individually dispersed[40]. Furthermore, due to processing efficiency and cost, CVD-produced MWNTs will likely be the most industrially viable[41].

Typical methods for dispersing CNTs into thermoplastic polymers are high-shear melt mixing[42], or similarly, circulation of a nanotube/polymer blends though an extruder fitted with mixing screws[43]. Invariably, the shearing forces generated during the flow of viscous molten polymer through confined spaces is used to disperse the nanotubes[44]. Nanotubes, however, are known to increase the viscosity of fluids due to their large aspect ratio, high stiffness, and degree of entanglement[45-47]. Therefore, achieving high loadings of well-dispersed CNTs in polymer melts is difficult even at high temperatures (~10-20 wt.% is a commonly reported upper limit to uniform dispersion attained with melt mixing[48]). Another method of CNT dispersion particularly suited for solution processable polymers is sonication, which uses high frequency sound waves to induce cavitation in low viscosity solvents. In the presence of CNT agglomerates, the energy released upon cavity collapse breaks up the agglomerates dispersing the nanotubes into the solvent[49-51]. Matrix polymer can then be dissolved into the CNT/solvent dispersion rendering a solvent-processable dispersion. Alternatively, matrix polymer can be introduced by *in-situ* polymerization of miscible liquid monomer in the presence of the CNT dispersion[52-54]. The viscosity of the final dispersion can be adjusted with both heat and solvent addition or evaporation making higher concentrations of well-dispersed CNTs in the final, solidified polymer possible. Loadings of up to 60wt.% CNTs have been reported in PVA composite fibers using this method of dispersion[55]. Recently the use of calendaring for dispersing CNTs in epoxy resins have be reported[56, 57]. In almost every case, it has been shown that the quality of CNT dispersions has a profound impact on the resulting composite properties. Initial mechanical property enhancements at low loadings, ~1wt.% CNTs, often saturate or are reduced at higher loadings[43, 58, 59]. Agglomerates of CNTs can act as a stress concentrating points, which reduce the mechanical properties of the matrix[60], or as weakly bonded particles which slide apart under shear offering no reinforcement to the matrix. The significance of these observations is important for nano-reinforced composites in general. However its understanding is obscured due to the difficulty in quantitatively evaluating the homogeneity of billions of CNTs throughout a macroscale composite. Recent reports have made progress in this assessment[61, 62]. Nevertheless, once dispersed in polymer melts or solutions, dispersions of CNTs can be processed into composite parts via conventional polymer processing techniques such as injection molding, film casting, or fiber spinning, from which test specimens can be fashioned, and the composite properties determined.

Factors Influencing CNT Dispersion

The homogeneity of CNT dispersions, either via shear mixing or sonication, is not only a critical factor affecting composite properties, but an important parameter in the quality and stability of composite processing as well. The three most influential factors affecting the quality of the dispersion are the amount of dispersive energy input into the system, the degree of the initial entanglement of the bulk CNT material, and the interaction of the CNT surface with the continuous phase. The first factor was investigated by Andrews[11] regarding melt mixing MWNTs into various thermoplastics. Dispersion quality was assessed via optical microscopy of relatively large areas of the composites (100 x 100µm), and the observed homogeneity was correlated to the amount of mechanical energy input by the high shear melt mixer. A minimum value of approximately 1 kJ/ml, was found to effectively disperse a range of MWNT concentrations up to 5.0 vol.%. Higher loadings required higher amounts of mixing energy, and their homogeneity was questionable. Given that such a large amount of energy was used to disperse the MWNTs, a certain degree of mechanical damage to them can be expected. A corresponding reduction in MWNT length was found to accompany shear mixing, but CNT aspect ratios of 200+ remained. CNT shortening is an unavoidable result in all dispersive processes, including sonication, given the forces that the CNTs are subjected to, and may in fact serve to enhance the dispersibility of the CNTs themselves as their ability to entangle diminishes with decreasing aspect ratio. However, excessive reduction of the CNT length may negatively impact its reinforcing capacity. Kearns and Shambaugh[63] report an optimum sonication time of 2hr. at 40kHz for a nanotube loading of 1wt.%; a compromise between achieving sufficient dispersion and minimizing CNT damage. The use of ultrasonic induced cavitation to disperse CNTs into low viscosity fluids is somewhat dependent on the frequency used. Ultrasonic instruments using a frequency of ~20kHz have been shown to disperse MWNT mats very well[49]. Higher frequency sonication instruments, such as ultrasonic cleaning baths at ~40kHz, have also shown to be effective[63]. The efficiency of ultrasonic dispersion depends upon an inverse relationship between frequency and particle size. Thus, it may be advantageous to employ a program of progressively increasing frequency to sequentially reduce bulk agglomerates of CNTs into individual tubes[64]. The degree of CNT shortening is likely also to depend on the defect density within the tubes themselves. TEM and SEM analysis of the dimensions of CVD grown MWNTs post sonication enabled Yang to deduce an empirical relation between the resulting aspect ratio as a function of sonication energy per volume of dispersion[65].

$$(1\text{-}1) \quad \left(\frac{l}{d}\right)_{MWNT} = 1455\left(\frac{E}{V}\right)^{-0.27}$$

E = watts of 20kHz sonicating wand x sonication time; V= m^3 of dispersion

The second factor affecting CNT dispersion, the initial state of CNT entanglement, has been shown to severely limit the homogeneity of dispersion[66]. "Bird's nest", or highly entangled CNTs produced from floating catalyst CVD processes or bundles of SWNTs are very difficult to individually disperse by shear or sonication alone. MWNTs grown

on substrates in aligned arrays with virtually no entanglement have been shown to be more easily dispersed[66].

Surface Treatment of CNTs

The third factor affecting CNT dispersion, the interaction of the CNT surface with the continuous phase, has been more commonly investigated in terms of surface treatment of CNTs. The ability to produce a homogeneous dispersion of CNTs in a polymer matrix or solution can be enhanced by chemically altering the nanotube surface to augment the solvent-nanotube or polymer-nanotube interactions. The natural surface of graphite is hydrophobic. Dispersing neat CNTs into polar and oxygenated environments is thus facilitated by surface treatment. This may be accomplished by a variety of methods including the use of surfactants, chemical functionalization, and *in-situ* polymerization. Treatment of SWNTs with a non-ionic surfactant was shown to enhance the dispersion and resulting mechanical properties of epoxy-matrix composites relative to un-treated SWNTs[67]. Other examples of CNT dispersions benefiting from the use of surfactants have been reported[55, 68, 69]. Above all, oxidative treatments of CNTs have been widely reported as a means to improve dispersion[45, 46], including the use of strong oxidizing agents such as nitric/sulfuric acids, $KMnO_4$[70] and H_2O_2[71], and by subjection to oxygen plasmas[72]. One of the most popular methods is the sonication or refluxing of CNTs in a 3:1 solution of sulfuric:nitric acid[45, 46, 73-75], which has its roots in eletrophilic substitution of small aromatic hydrocarbons. The resulting oxygenated groups on the CNT surface, including hydroxyl and carboxylic groups counteract the Van der Waals attractive forces between CNTs and enhance interaction with hydrophilic matrix phases thus improving dispersion. Kim[73] reports that sonication of MWNTs for 8hrs in 3:1 sulfuric:nitric acid, resulted in the addition of carboxylic acid groups at a concentration of approximately 1.3×10^{-3} mol/g. Tethering and/or wrapping of polymer chains to CNT surfaces by polymerizing monomers *in-situ* with the CNTs has been shown to be effective in improving both dispersion quality and composite properties[52, 70, 76]. Eitan[76] demonstrated evidence of epoxide functionalization of oxidized MWNTs, which can be used to covalently crosslink CNTs into epoxy matrices. Similarly others have reported amine functionalized CNTs for crosslinking epoxy matrices[77-79]. In other reports, uniform dispersion and significantly enhanced moduli were observed using PMMA-grafted MWNTs in bulk PMMA matrix composites[52, 54]. Other methods of chemically functionalizing CNTs include the use of diazonium salts[80], radical species[81], photochemistry[82] and others[83, 84] to derivitize a wide variety of organo-CNTs.

Processing CNT-Polymer Dispersions: Composite Films

CNT-polymer composites are commonly produced in the form of films for mechanical, electrical and thermal property analysis. The thicknesses of these films range from millimeters to electron-transparent TEM samples. Once a suitable level of CNT dispersion is achieved in the matrix, films are processed by pressing CNT-polymer melts, casting CNT-polymer solutions/thermosets into molds, or spinning films. Test specimens of precise dimensions can be cut or machined from these composite films for testing.

Pressing CNT-thermoplastic films is well described in the literature and is a simple method of producing composite specimens[11, 60, 71, 85-87]. Polymer containing dispersed CNTs is typically crushed or pelletized, placed between heated platens, and pressed at a pressure in the range of 10-30MPa[85, 86] such that molten CNT composite polymer flows outward constrained to some predetermined thickness by shims or a mold[11]. Upon solidification, test specimens are then cut from the film. For CNT-polymer solutions and CNT-thermoset matrices, composite films are typically processed utilizing a casting technique. Well-dispersed CNT-polymer fluids are transferred to molds and heated to evaporate the solvent or cure the thermoset[17, 52, 88-91]. In a similar method, dispersed CNTs in a polymer solution are deposited dropwise onto substrates, and the solvent is evaporated. This process is repeated to build up to the desired thickness of film[39, 40, 92-94]. To produced ultra thin CNT-polymer composite films (thickness = 200nm)[95] for TEM, spin casting is used in which suspensions of CNTs in low viscosity polymer solutions are deposited dropwise to the center of a rotating substrate. Spinning for 20 to 30 seconds at 3000 rpm has been reported to produce electron-transparent films[96]. Fabrication of continuous CNT-polymer composite films has been demonstrated by extrusion of CNT composite thermoplastic through a slit die followed by take-up onto a chilled roller[97]. Other techniques include resin infiltration into dry CNT preforms[27, 98-100], polymer intercalation of aligned MWNT mats[101-103] and SWNT "buckypaper"[104], as well as complete *in-situ* polymerization of thermoplastic matrices[70, 105].

The orientation of embedded CNTs relative to the composite principal directions, as in all fiber composites, has an effect on the properties that are measured. The process of shear-mixing or sonication results in 3-D random orientation of the CNTs throughout the polymer matrix, which can be preserved throughout processing given the absence of strong shear or elongational flows. For most CNT-polymer film processing, the CNT orientations are random relative to the *xy* plane of the film. Exceptions occur when any degree of stretching or drawing of the film is implemented, which forces embedded CNTs into alignment with the direction of flow[71, 88, 91, 97, 106]. The highest degrees of CNT alignment within a polymer matrix are achieved by spinning dispersions of CNTs in polymer fluids into fibers.

Processing CNT-Polymer Dispersions: Composite Fibers

Another enabling advantage of the small size of CNTs is that homogeneous dispersions of CNTs in viscoelastic polymer fluids can be spun into composite fibers. That is, the nanofibers themselves can be co-spun with the matrix to form a highly oriented composite fiber. Melt spun, solution spun, and electro-spun CNT composite fibers have been produced. These methods have been shown to be very effective in aligning the CNTs with the fiber axis. This class of oriented CNT composites is of particular interest since direct axial loading of the CNTs is possible. It is in this fashion that high-strength, light-weight CNT composites are envisioned. However, the ability to sustain stable CNT-polymer composite fiber spinning is largely dependent on the homogeneity of the dispersion. CNT agglomerates can disrupt the flow as fiber attenuation is applied leading to breakage during processing, or in the case of large agglomerates, complete blockage of the small diameter orifices from which the fibers are extruded can occur. Achieving

7

large attenuations or draw ratios, which serve to orient both the CNTs and the matrix polymer chains with the fiber axis resulting in increased fiber properties, is primarily dependent on the quality of the initial CNT dispersion.

Melt spinning of CNT/thermoplastic composite fibers has been investigated for numerous polymers including poly(methyl methacrylate)[43, 44, 71], polypropylene[63, 107, 108], polystyrene[11], polyamide[66], and engineering thermoplastics such as polyimide[42], and poly(ether ether ketone)[32]. In a typical process, the CNTs are dispersed in the molten polymer using a high shear mixer followed by extrusion through a cylindrical die orifice or spinnerette. Before the composite fiber cools and solidifies, attenuation is induced by accelerating the extruded fiber onto a rotating spool. Testing of the fibers can then be performed using a variety of techniques, including single filament tensile testing. CNT composite fibers spun from polymer solutions often involve a coagulation process to solidify the fibers. Reported solution spun CNT composite fibers include poly(vinyl alcohol)[55, 109-111], poly(acrylonitrile)[49, 112-114] (an important precursor to commercially produced carbon fiber), regenerated cellulose[115], ultra-high molecular weight polyethylene[116] and poly(p-phenylene benzobisoxazole)[117] (PBO). Electro-spun fibers are produced by generating a high voltage between a negatively charged spinning solution and a conductive collector. The advantage of this technique is the production of ultra-fine fibers (<100nm) as very fine jets of polymer are accelerated towards the collector, but unlike melt or solution spinning, the production of continuous filament is difficult. Fibers have been electrospun from dispersions of CNTs in poly(vinly alcohol)[118], poly(acrylonitrile)[119], and poly(vinylidene fluoride)[120]. Recently fibers spun from pure CNTs (no matrix) have also been reported[121-123].

CNT Orientation in Films and Fibers

As previously emphasized, the orientation of embedded fibers has a major impact on the measured properties. Composites containing fibers oriented in the direction of loading will display the highest mechanical properties. An out-of-plane misalignment of 10° reduces the effective modulus of single crystal graphite from 1020GPa to 120GPa[43]. Measuring of the degree of orientation of embedded CNTs relative to a principal axis is therefore an important consideration. The use of azimuthal or phi scanning x-ray scattering and polarized micro-Raman spectroscopy have been shown to be effective in quantifying the CNT alignment within composite structures[114]. The x-ray technique, analyzes the two symmetrically diffracted arcs by the CNT interlayer spacing d_{002}, about the azimuthal angle, and is thus well-suited for MWNTs with preferred 1-D alignment (Figure 1-3). The integrated intensity of these diffracted arcs as a function of the azimuthal angle results in peaks. The breadth of a peak at half its maximum (FWHM) is inversely proportional to the degree of CNT alignment. That is, very sharp peaks correspond to a very high degree of alignment. This process is described by Lucas and Vigolo[124] regarding the degree of orientation of CNTs in solution spun PVA composite fibers, and by Kumar[112, 114, 117] to evaluate CNT alignment in PAN and PBO composite fibers, by Shaffer[32, 66] in polyamide and PEEK composite fibers and by Zhou[125] in drawn poly(hydroxyaminoether) films.
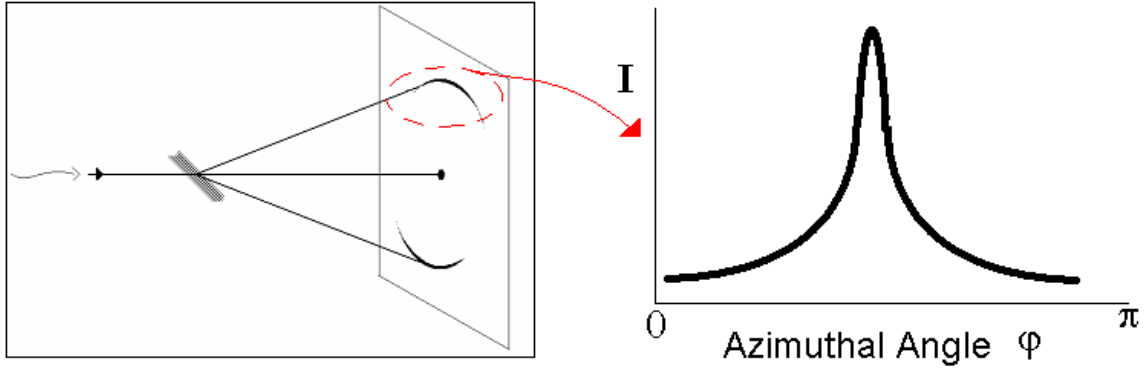
Figure 1-3 2-D x-ray scattering from aligned MWNTs

X-ray orientation data is often used in conjunction with the Herman-Stein orientation factor[126] (equation 2) which describes the average angle between the CNTs and the fiber axis, ϕ (f = 1 → perfect alignment; f = 0 → random alignment, f = -0.5 → perpendicular alignment).

(1-2) $$f = \frac{3\langle\cos^2\phi\rangle - 1}{2} \qquad \langle\cos^2\phi\rangle = \frac{\int_0^{\frac{\pi}{2}} I(\phi)\cos^2\phi\sin\phi d\phi}{\int_0^{\frac{\pi}{2}} I(\phi)\sin\phi d\phi}$$

Similarly, determination of CNT orientation by polarized micro-Raman spectroscopy is well described by Fischer[127], and is based on the analysis of the intensities of the Raman D and G bands as a function of the angle between the polarized beam and the composite fiber axis[42, 71]. Another technique of micro-Raman spectroscopy utilizes the principle of peak shifting as a function of the induced strain in the CNTs. This technique is useful for elucidating the degree of stress transfer to the CNTs themselves[90, 116, 128, 129]. As the bonds between the carbon atoms of the nanotube are strained, the Raman peak shifts. This technique was used to by Gao and indicate MWNT slippage at 1.5% strain in UHMWPE fiber[116]. More efficient transfer of composite strain to axial strain in the CNTs manifests itself in higher degrees of peak shift, and thus better interfacial stress transfer. Other techniques to probe CNT orientation include light scattering microscopy to investigate alignment of CNTs in shear fields[130, 131]. However, in practice, limitations to perfect uniaxial orientation of CNTs, even in highly drawn fiber matrices, have been observed, and attributed in part to intrinsic 'waviness' or graphitic misalignment within the CNT structures themselves[66].

1.3 Mechanical Properties

Enhancement of Elastic Modulus and Break Strength

The application of CNTs as reinforcing fibers within polymer matrices is an idea that is profoundly motivated by both CNT mechanical properties, and CNT nano-fiber morphology. In concept, this is the nanometer-scale analogue to conventional carbon fiber composites, offering exciting possibilities for materials design given that CNTs

have been measured to be more than 15 times stronger than the best available carbon fiber, have elastic moduli of basal plane graphite, and yet remain extremely flexible with aspect ratios of greater than 1000.

Enhancing the elastic modulus of a polymer reflects the transfer of stress from the polymer matrix to the high-modulus embedded CNTs. Thus, strong interfacial adhesion between the polymer and CNT is preferred for stiffening the composite. This implies that if enhancements are not observed, weak bonding between the CNTs and matrix exists.

Table 1.2 Published mechanical properties

Matrix	Fiber	Loading Wt.%	Form	E_c GPa	σ_c MPa	T_c J/g	Ref.
PEEK	CNFs	10	Fibers	+20%	+20%		[32]
PVA	SWNT	60	Fibers		1800*	600*	[132]
	MWNT	< 1	Films	+370%	+430%	+170%	[92]
	DWNT	0.16	Films	+200%	+100%		[51]
	MWNT	1	Films	+400%			[59]
	SWNT	50	Fibers		1500*	50	[133]
PVC	f-MWNT	1	Films	+60%	+100%	+450%	[134]
Cl-PP	MWNT	< 1	Films	+310%	+390%	+440%	[92]
PAN	SWNT	10	Fibers	+100%			[112]
	MWNT	3	Fibers	+36%	+31%	+80%	[49]
	MWNT	5	Fibers	+75%		+230%	[114]
	MWNT	1.9	Fibers	+393%			[135]
PP	SWNT	1			+45%		[107]
	SWNT	1	Fibers	+55%	+40%		[63]
	CNFs	5		+50%	+100%		[108]
	CNFs	15	Films	+90%			[60]
	MWNT	0.5	Fibers	+27%	+100%		[136]
	f-SWNT	10	Fibers	+134%	+173		[53]
PBO	SWNT	10	Fibers		+50%		[117]
PMMA	MWNT	30 20	Films	+140% +1100%			[86] [52]
	f-MWNT	1	Films	+90%	+370%	+1270%	[54]
PMEA	MWNT	1	Films	+200%			[68]
PS	MWNT	5	Films Drawn Films	+10 % +49%			[97]
		20	Films	+50%	+ 0%		[11]
	f-MWNT	0.5	Films	+60%	+50%	+63%	[134]
UHMWPE	MWNT	1	Drawn Films	+25%	+48%	+150%	[90]
	MWNT	5	Fibers		+19%	+44%	[116]
Polyurethane	MWNT	18	Fibers	+170%			[75]
HDPE	CNFs	8	Films	+60%			[85]
Rubbery Epoxy	f-MWNTs	0.1	Films	+28%	+200%		[79]
PC	SWNT	0.06	Films	+29%			[137]

Mechanical property enhancements of nano-composite materials are shown.
E_c = composite modulus; σ_c = composite break strength; T_c = composite toughness
* These are absolute values not increases compared to neat polymer, f = functionalized

Increases in break or yield strength also reflects strong interaction between the CNT and polymer, but are profoundly affected by the presence of defects such as voids or

agglomerate inclusions, which serve to initiate failure by stress concentration. Therefore, processing can have a major impact on the measured strength, but less of an effect on the measured modulus. Namely, poor CNT dispersion can be detrimental to strength, which is often observed at higher concentrations of CNT and attributed to agglomeration*[51, 75, 115, 134]*. Table 1.2 contains numerous reported increases in the elastic modulus and break strength of CNT-polymer composites for various polymer matrices.

Figure 1-4 represents a graphical interpretation of Table 1.2, plotting the relative increase in the polymer matrix modulus (fibers and films) with CNT concentration as reported in the literature. Two separate trends in the data are observed; one with rather modest increases in modulus, and the other with significant increases. The fundamental reason for their difference lies in the nucleation of crystallinity. More specifically almost all of the top four performing composites are reported by Coleman et. al, in a poly(vinyl alcohol) (PVA) matrix. Central to each of these increases is the observation of polymer coatings on the embedded CNTs, which is a result of crystallization nucleated at their surfaces. PVA has repeatedly shown this high affinity to the CNT surface*[39, 92, 138]*. Due to the high surface area to volume of CNTs, significant enhancements in matrix crystallinity can and have been realized at low fractions of filler. Furthermore, composites that produce these large increases in modulus are typically accompanied by large increases in break strength as shown in Table 1.2.
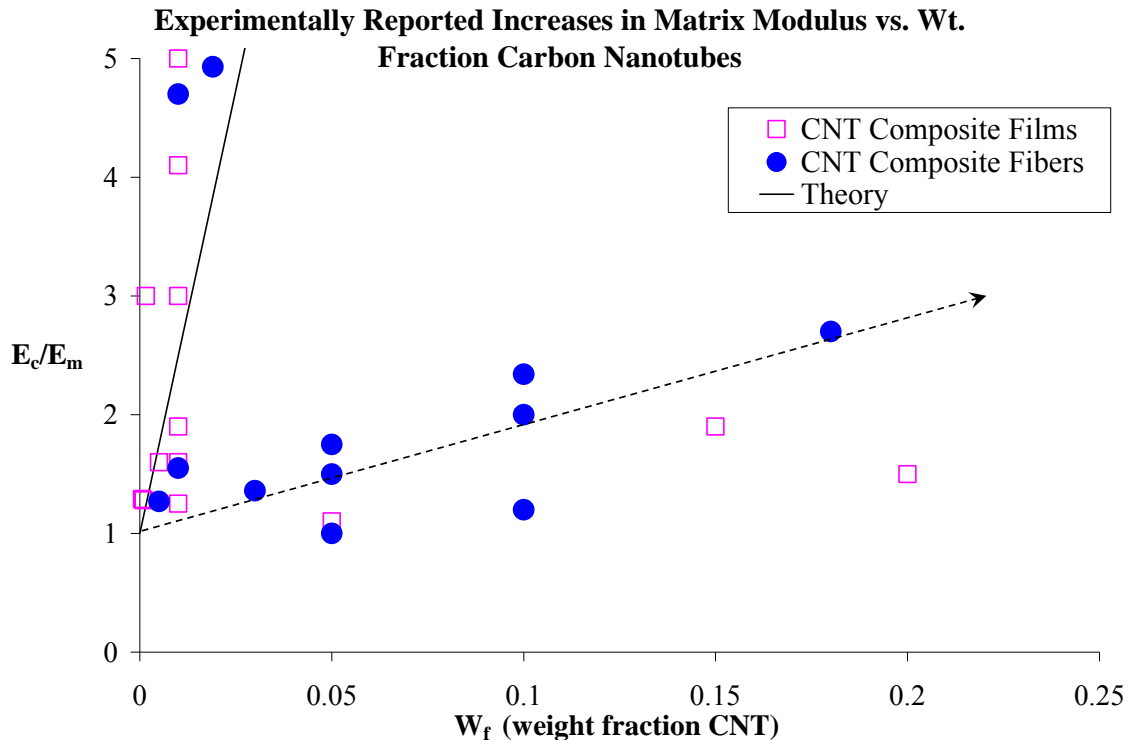
Figure 1-4 Published CNT composite modulus enhancements
Enhancements in composite modulus reported in the literature are plotted as function of CNT concentration. Most groups report relatively modest increases for CNT composite films and fibers. However some report drastic improvements, which turn out to be related to the nucleation of polymer crystallization at the CNT interface.

In the case of most polymers, the yield strength defines the practical limit to their ability to be stressed and remain useful. After yielding the polymer will flow, permanently deforming, and finally rupture. One can think of the yield stress as the limit of elastic strain. However, the break stress of polymers usually occurs at strains well beyond the elastic limit. In the plastic regime, polymer chains (and CNTs) are flowing to relieve the stress and accommodate the large strain. Polymers often strain-harden as a result of this flow, due to the polymer chains (and CNTs) aligning with the direction of load. Therefore, an increase in polymer modulus with increasing strain is observed. The polymer stress then continues to increase as the plastic modulus increases, which is amplified as the cross section of the polymer contracts. Finally, a drastic reduction in cross-sectional area occurs called necking immediately followed by complete rupture. In polymers this rupture is often caused by a process known as crazing. Micro-voids, initially present throughout the material, are forced into motion under plastic flow. These micro-voids then coalesce as they grow and contact each other. As the voids expand, the degree to which they concentrate stress along their boundaries increases. Finally, a critical crack tip will propagate from one of these large voids resulting in rapid coalescence of other, nearby voids. This, in effect, dooms the material to failure as macroscale coalescence of voids not only significantly reduces the cross-sectional area of the material, but provides a mechanism of stress reduction that self-accelerates resulting in complete material rupture. The effect that dispersed CNTs can have on polymer crazing can be significant[139]. Some recent improvements in CNT composite strength are noteworthy simply due to their magnitude. These include CNT composite gel spun UHMWPE fibers with a reported break strength of 4.2GPa[116], hot drawn CNT composite PVA fibers at 1.5GPa[133], and pure CNT fibers at 1.9GPa[123].

Enhancement of Toughness, Fatigue and Creep

Qian *et. al.*[140] using in-situ TEM straining of MWNT/polystyrene demonstrated that nanotubes function to bridge crack opening by spanning the separating surfaces in the crack wake. Wagner[141] reported similar findings. At crack separations of ~800nm, the MWNTs were observed to pull out of the crack face, especially those aligned perpendicular to the separating faces, indicative of nanotube/matrix interfacial failure[140]. Tube fracture was observed to occur for defective tubes, such as at catalyst inclusions, or for tubes aligned parallel to the crack.

The mechanism of CNT crack bridging has been credited with enhancing the toughness of polymers primarily by increasing the strain to break of the material. This effect was shown by Lozano[85]. Increases of 220% in elongation translated into a 290% increase in toughness, which was attributed to the embedded carbon nanofibers (CNFs) in HDPE arresting crack propagation from coalesced voids. Gorga and Cohen[44] report a similar result augmented by the presence of aligned MWNTs in PMMA fiber matrices. Increases in the toughness of 800% were reported in composite fiber containing 1 and 3wt.% MWNTs, and attributed to the nanotubes bridging crazes and subsequent cracks in the matrix under uniaxial tension.

CNT pull-out provides energy dissipation by frictional slipping thus benefiting material toughness. Therefore aligned CNT systems, in agreement with Qian's observed pull-out of orthogonally oriented tubes, may provide for significantly enhanced toughnesses. Recently this effect was clearly shown by Ko for aligned MWNTs embedded in electrospun polyacrylonitrile fibers[139]. TEM imaging of elongated fibers provided further compelling evidence that CNTs serve to bridge crazes. CNTs are small enough to bridge micro-voids before they coalesce and grow to a failure-causing size. Likewise CNTs may also function to pin void motion, effectively slowing void coalescence. Indeed many other researchers have reported significant increases in toughness of aligned CNT composites[42, 49, 55, 117, 132, 133], which may prove useful especially for enhancing the performance of impact resistant materials. In most cases, increases in matrix polymer toughness are accompanied by higher CNT-polymer composite failure strains. Increasing the strain energy (area under the stress-strain curve) is directly proportional to increases in material toughness; but only to a useful limit. Excessive strain can easily nullify huge toughness. For example body armor must absorb the kinetic energy of projectiles at minimal strain to prevent injury to the wearer. PVA-SWNT fibers were shown to dissipate 55 J/g by 11% strain[133], while pure CNT fibers were demonstrated at 8.9 KJ/m^3 by 7% strain[123] (0.005 J/g for 2g/cc fiber).

Other reported effects in CNT-polymer composites are increases in composite fatigue life and creep. Marrs reported significant increases in the fatigue life of MWNT/PMMA-based bone cement composites, an important consideration for the lifetime of prosthetic joint replacements[142]. An enhancement in fatigue performance of over 500% at only 2 wt.% MWNTs was observed[143]. CNTs were also shown to be quite effective in mitigating creep in both epoxy[144] and polypropylene[145] composites. An underlying connection between these inelastic effects is the function of CNTs as craze restrictors in polymer matrices.

Important Factors Influencing CNT-Polymer Composite Mechanical Properties

Shaffer[146] investigated the effect of the type of CNT reinforcement in polyamide fibers and concluded that the use of aligned substrate-grown MWNTs resulted in the best composite properties. An identical result was reached by Gorga[44] for MWNTs in PMMA. The fact that the bulk MWNTs were not initially entangled resulted in better dispersion. Other researchers reported that nanotubes with higher aspect ratios improved composite properties[44, 140]. A recurring inter-relation between processing and properties is dispersion. Many researchers have reported diminishing properties of their CNT composites as the concentration exceeds 1 wt.%[54, 107], or 5-10wt.%[43, 44]. The continuous increase in composite properties predicted by theory does not occur, and is likely due to a lack of homogeneous dispersion. The orientation of the CNTs relative to the load has also been shown to have an effect on the composite properties. Thostenson[97] found a 50% improvement in the tensile modulus of aligned MWNT/PS composites compared to a 10% improvement for randomly oriented MWNT/PS composites. Others have shown that the strength of the interfacial bonding and other interfacial effects in CNT-polymer composites has a profound effect on the composite properties[68, 92, 134]. Nevertheless, dispersion, aspect ratio, orientation, and interfacial shear strength are all significantly important parameters.

Analysis of Experimental Results

Effective Modulus:
The idea of 'effective modulus' has been applied in the case of CNT composite films where effects including random CNT orientation, and inefficient stress transfer are expected to occur. Two popular discontinuous fiber composite theories utilizing this symmetry are the Krenchel Rule of Mixtures[146] and the Halpin-Tsai Equations[147]. Krenchel's is a modified rule of mixtures commonly written as:

(1-3) $E_c = \eta_o \eta_l E_f V_f + E_m(1 - V_f)$

Here the 'effective fiber modulus' (fiber meaning CNT) depends on both a stress-transfer term, η_l, and an additional orientation term η_o. Often these are used as fitting parameters to experimental data, but shear-lag analysis can be used to determine them as first proposed by Cox[148]. However in the case of composite films, the orientation factor varies from (3/8) to 1 as orientation varies from random to perfect alignment. Factors less than (3/8) imply out-of-plane misalignments of the fibers.

The Halpin-Tsai Equations approach the fiber orientation issue as a statistically weighted mix between axial and transverse loading of discontinuous fiber (assuming again rotational symmetry of planar fiber orientations). The stress transfer issue is similar to the Cox shear-lag approach in that it involves both fiber aspect ratio and fiber to matrix modulus ratio (assuming an isotropic matrix $G_m = E_m/2(1-\nu_m)$). They are commonly written as:

$$(1\text{-}4) \quad E_c = \left[\frac{3}{8} \frac{1 + 2\left(\frac{l}{d}\right)_f \eta_l V_f}{1 - \eta_l V_f} + \frac{5}{8} \frac{1 + 2\eta_T V_f}{1 - \eta_T V_f} \right] E_m \quad \eta_l = \frac{\left(\frac{E_f}{E_m}\right) - 1}{\left(\frac{E_f}{E_m}\right) + 2\left(\frac{l}{d}\right)_f} \quad \eta_T = \frac{\left(\frac{E_f}{E_m}\right) - 1}{\left(\frac{E_f}{E_m}\right) + 2}$$

For uni-axial loading of aligned fibers, only the first term in brackets is used weighted with a coefficient of 1, and will condense to the axial rule of mixtures for infinite fiber aspect ratio.

Again, the (3/8) weighting coefficient is used to account for random fiber orientation effects on the longitudinal stiffening, but a second weighted term is added that accounts for composite stiffening from transversely oriented fibers. The two weighting coefficients add to unity. The popularity of the Halpin-Tsai equations especially when applied to non-oriented CNT-polymer composite films is due to their robustness in accounting for several effects while maintaining relative simplicity. Furthermore, the fiber aspect ratio has been used a fitting parameter for experimental data sets providing insight into the efficiency of stress transfer[94].

TEM observations of embedded CNTs have shown that they are not rectilinear but have some degree of waviness[140], which may be due to their crystalline defects and elastic flexibility. Computational analysis has proved insightful in dealing with deviations from straightness of the CNTs themselves. In particular, Brinson[58, 149] addressed the issue of CNT waviness or curvature and its effects on composite properties. A corresponding reduction in the modulus of wavy CNTs was expected due to CNT anisotropy. Finite

14

element analysis was used to calculate the effective modulus of a wavy CNT of wavelength, λ, relative to a straight CNT[58]. A second micromechanical model used this result to predict the properties of a bulk CNT composite considering a distribution of embedded CNT waviness, or amplitude of curvature to wavelength ratio. The results predicted significant reductions in effective modulus for wavy CNTs. For a waviness of 0.1, or a CNT that is 90% straight, a 40-50% reduction in modulus was predicted. This method, applied to experimental results of MWNT/PS composite films, provided a more accurate model than predicted with straight CNTs. This work and others[150, 151] underscore the importance of CNT waviness to composite properties.

The issue of MWNT diameter and its effects on composite properties has been modeled and applied to experimental data by Thostenson[152]. Here, stress was considered to be transferred to the MWNTs through interfacial shear stress between the matrix and the *outer shell* of the MWNT. They considered that although the MWNT acts as a solid fiber in a composite, tensile stress is only carried by the outermost tube wall due to weak inter-wall Van der Waals bonding. Therefore, the effective modulus of the MWNT must account for the excluded volume, or dead space, interior to the outer shell. The modulus of this 'shell' of carbon is identical to the intrinsic MWNT modulus, but since in a composite the interior is considered dead volume, the effective modulus will be reduced in the ratio of the cross-sectional areas of the outer shell thickness to the entire MWNT outer diameter. Assuming the force is carried entirely by the outer shell, the resulting relation is:

$$(1\text{-}5) \quad E_{MWNT}^{eff} = \frac{4t}{d} E_{MWNT} \quad \text{(t is the outer shell thickness, typically 0.34nm, and d is the outer diameter)}$$

Thus larger diameter MWNTs containing many concentric shells, had significantly lower effective reinforcing moduli. Experimental verification of this idea was tested by fabricating drawn films of MWNTs in polystyrene to align the MWNTs. Electron microscopy was used to measure the distribution of MWNT diameters, which was modeled in the composite by partitioning the MWNT volume fraction into discrete diameter ranges. A Halpin-Tsai based model was applied in which the effective moduli of the embedded MWNT diameter distribution were used to yield an overall composite modulus. The model was compared to experimental data for composite films with MWNT concentrations of 5 and 10wt% with very good agreement. Larger diameter MWNTs occupy a larger volume fraction of the composite, display lower effective moduli, and thus make a reduced contribution to the composite properties. However many groups report MWNT composites to be superior to SWNT composites, which is likely due to differences in dispersion and interfacial bonding[66]

Interfacial Bonding:
Perhaps the most important issue in CNT-polymer composites is a good understanding of interfacial bonding between the embedded CNTs and the polymer matrix. Experimental determination of the interfacial shear strength of CNT-polymer composites has recently been demonstrated[153]. Wagner[153] studied this issue by conducting experiments in which a MWNT, attached to an AFM tip, was embedded in a polymer and pulled out. The force versus pull-out length was recorded for a poly(ethylene-co-butene) matrix resulting in an interfacial shear strength of 47MPa. This value is consistent with other

measurements where estimates of ~50MPa for various nanotube types were recorded[39].

1.3.1 Interphase Effects

Shortcomings of the Rule of Mixtures

$$(1\text{-}6) \quad E_c = E_{NT}V_{NT} + E_m\left(1 - V_{NT}\right)$$
(E_{NT} = CNT tensile modulus, E_m = matrix modulus, and V_{NT} = CNT volume fraction)

Below are the underlying assumptions used to arrive at the rule of mixtures, and how they may be inadequate for CNT-polymer composites.

1) *The CNT-matrix interface is strong (continuity of strain)*
This implies no slippage of the CNTs through the matrix occurs. In polymer-CNT composites, significant nanotube pull-out has been verified even at low strain indicating interfacial failure[49].
2) *The CNTs are all aligned parallel with the direction of load*
The fiber modulus, E_f, refers to the modulus of the fiber when loaded in pure tension. Embedded CNTs typically show some measure of curvature[154], waviness[58], and misalignment with any given material direction even for highly drawn matrices[71, 88, 112, 146].
3) *The length of CNTs is sufficient for maximum interfacial shear stress build-up*
This implies the average length of the embedded CNTs is long relative to the load transfer length (length required for complete interfacial shear stress build-up). Embedded lengths of CNTs post sonication were measured to be primarily in the 1-10μm range[155]. Pull-out of these CNTs was confirmed via TEM straining[49].
4) *The CNTs are homogeneously dispersed and homogeneously loaded*
This implies that each individual CNT is loaded homogeneously by stress transfer from the surrounding matrix. (No CNT-CNT interactions). Achieving homogeneous dispersion of CNTs, especially at concentrations > 10wt.% has been shown to be difficult[132].
5) *The composite modulus is linearly related to the moduli of its component phases*
This implies that the modulus of each phase is independent and unchanged by the presence of the others. Nanotubes have been shown to induce polymer matrix crystallization near their surfaces thus altering the matrix[93]. In other words, the interphase matrix potentially has different properties from the neat matrix.

Within the limit of small applied strain, assumptions 1-3 have been addressed primarily in terms of an effective fiber modulus, which is essentially a reduced intrinsic fiber modulus based on aspect ratio, orientation and interfacial bonding. Assumptions 4-5 have recently shed light on issues that better explain the largest increases in mechanical properties of CNT composites. In particular, numerous publications have cited observations of CNT-induced crystallinity, primarily by DSC studies, and SEM imaging[32, 39, 59, 92, 93, 107, 138, 146].

Nucleation of crystallinity at the Polymer-Nanotube Interface

The key to understanding why a few CNT composites perform so much better than others is described well by Coleman*[39, 92, 138]*. They show that the increases in composite modulus could be scaled with the embedded surface area of nanotubes*[39]*. Here it is suggested that each CNT had a discrete crystalline polymer layer associated with it, which was supported by evidence from SEM imaging and DSC thermographs*[92]*. Indeed, others have observed polymer sheathing of CNTs protruding from fracture surfaces*[50]*. Inspection of fracture surfaces of these and other composites*[50, 92]* supports the contention that failure occurs at the interface between a crystalline polymer layer bound to the nanotube surface and the bulk polymer (i.e. not at the interface with the actual MWNT surface). This implies that the MWNTs are not being strained to failure, and that the nanotube interface with the matrix is strong enough to stay intact. It also suggests that the MWNT + crystalline polymer sheath are acting as a single unit, which can be thought of as an effective fiber. After establishing that the MWNTs were not being strained to failure, the application of short fiber composite theory was invoked to model the increase in composite strength. The correlation between the thickness of the adhered polymer coating and composite strength was successfully deduced, and fit the data well*[92]*.

$$(1\text{-}7) \quad \sigma_C = \sigma_{poly} + V_{NT}\left[\frac{\sigma_{shear}l_{NT}}{2R} - \sigma_{poly}\left(1+\frac{b}{R}\right)\right]\left(1+\frac{b}{R}\right)$$

(σ is strength, l is length, R is the nanotube radius, and b is the adhered polymer thickness. The subscripts C, poly, NT, and shear refer to composite, polymer matrix, nanotube and the shear between the bulk polymer and the adhered polymer coating respectively)

Coleman went on to also state that this crystalline PVA coating is itself stronger than the amorphous PVA matrix*[92]*, and the real breakthrough in modeling the composite modulus was in realizing that this new phase of ordered polymer at the CNT surface was itself responsible for much of the increase in the measured composite modulus*[138]*. This led to the double rule of mixtures approach in which the modulus of the ordered coating interphase, or third phase, contributes to the overall composite modulus.

$$(1\text{-}8) \quad E_C = \eta_o E_{NT}^{eff} V_{NT} + (1-V_{NT})E_a + \left(\frac{b^2 + 2Rb}{R^2}\right)(E_\chi - E_a)V_{NT}$$

(E is modulus, V is volume fraction, R is the nanotube radius, and b is the adhered polymer thickness. The subscripts C, NT, χ and a refer to composite, nanotube, ordered coating layer and amorphous bulk layer respectively. For definitions of E_a and E_χ refer to*[138]*)

It was also shown that the composite modulus and the % crystallinity scale together*[51]*. To this end, careful control of the crystallizing conditions of the matrix polymer may be useful for maximizing the formation of the interfacial crystalline layer as well as intentionally combining CNTs of desired diameter in specific polymer matrices*[156]*. Small diameter, easily dispersed multiwall carbon nanotubes grown in aligned arrays have been cited numerous times as being efficient at mechanical reinforcement, and may thus fill this role*[39, 40, 44, 146]*.

Apart from nucleation of matrix crystallinity for reinforcement, which is matrix-dependent, significant work is ongoing to optimize the bonding of CNTs to industrially important polymers. Here, efforts are focused on functionalizing the CNT surface for optimal interfacial bonding, as well as improving the degree of dispersion.

1.4 Electrical Conductivity

Conductive polymer composites continue to expand in application as the electronics industry thrives. The typical method of transforming insulating polymers into conductive composites is straightforward, and simply involves filling them with a sufficiently high volume fraction of conductive particles as to impart the desired final conductivity. Highly conductive polymer composites, such as epoxy solders, are traditionally filled with finely milled metal particles of silver or copper, and find application as solder in electronics and as electro-magnetic interference (EMI) shielding coatings. Moderately conductive polymer composites are often filled with carbon black, and are useful in anti-static electronic packaging materials, and in some cases, EMI shielding material. Although both fillers function well, both have drawbacks. For metals, their high densities make them heavy, and they tend to require concentrations greater than 50 wt.% to achieve the desired conductivity. Furthermore, they are expensive. For carbon black (CB), the maximum conductivity attainable is much lower, and highly filled CB-polymers can become brittle. The fundamental interest in using CNTs as conductive fillers in polymers is due to a combination of their aspect ratio and intrinsic conductivity.

The concentration of conductive filler necessary to invoke a sharp decrease of several orders of magnitude in resistivity is known as the percolation threshold. A good review of percolation in composites can be found by Lux*[157]*. For electrical conduction, percolation is the event that corresponds to the formation of a conductive pathway through the polymer matrix. It is often quantified as the concentration of filler necessary to step-wise reduce the resistivity of the composite by several orders of magnitude. In the case of CB or carbon nanotube (CNT) filled polymers, the resistivity typically drops from approximately 10^{15} to $<10^6$ Ωcm at a small increment in weight percent filler. This concentration of filler, which corresponds to this drop in resistivity, is the percolation threshold. Table 1.3 shows typical percolation thresholds of CB and CNT-filled polymers.

For polymer composites, minimizing the percolation threshold is desirable, not only for reduced cost, but because minimally filled polymers are easier to process and tend to be less brittle. Mathematical percolation theory is founded in statistical probabilities. From this point of view, fillers treated as geometric entities, are scattered in some defined 3-dimensional space. Here, the aspect ratio of the filler has been shown to dominate the onset of inter-particle connectivity, hence the percolation threshold. Up to 16 vol% spherical particles are needed for percolation, whereas less than 1 vol% are needed for particles of aspect ratio greater than 100*[57]*. These results have encouraged researchers to investigate the use of high aspect ratio CNTs as a sort of high-performance carbon black (which is often considered spherical). In practice, things are much more complicated. Dispersed carbons tend to flocculate into agglomerates due to Van der

Waals attractive forces, which are often not considered by percolation theories, and enable percolation to occur at much lower-than-predicted concentrations. Essentially the formation of conductive networks is a by-product of the natural tendency for carbon particles to agglomerate. CNTs, however, may offer the benefit to CB of forming higher conductive, less brittle composites at equivalent concentrations, and may in some cases be suitable, lightweight replacements for metallic-filled composites.

Table 1.3 Electrical properties of carbon-filled composites

Matrix	Filler	Percolation Threshold p_c (Wt.%)	Percolation Resistivity ρ_c (Ω-cm)	Minimum Resistivity ρ_{min} (Ω-cm)	Filler Loading at ρ_{min} (Wt.%)	Ref.
Epoxy	MWNT	0.1 high shear	10^3 (DC)	200	1.0	[158]
		0.011 low shear	10^5 (DC)			
Epoxy	MWNT	0.1	10^6 (DC)	10 -100	5.0	[56]
Epoxy	MWNT	0.0025	10^6 (AC)	200	0.5	[30]
	SWNT	0.05	10^6 (AC)	100	0.5	
Epoxy	SWNT	0.5	10^4 (DC)	100	3.0	[100]
Epoxy	MWNT	0.05	$<10^8$ (AC)	100	0.5	[57]
	CB	0.75		2×10^5	1.5	
Epoxy	MWNT	0.04	5×10^3 (AC)	100	6.0	[28]
Epoxy	MWNT	0.004	$<10^8$ (AC)	1×10^5	0.01	[159]
PMMA	MWNT	0.004	10^3 (DC)	1	30	[160]
PMMA	CB	0.5 dry mix	$<10^7$ (AC)	100	12	[161]
		5.0 soln mix		1×10^5	12	
PET	CB	2.2	10^3 (DC)	10	10	[162]

The electrical properties of several composites systems reported in the literature are shown. The values are approximate. DC and AC reflect measurements made by standard four-point DC and AC impedance spectroscopy methods respectively.

Table 1.3 shows that extremely low concentrations of CNTs can induce electrical percolation in epoxies. For most cases, less than 0.1 wt% of MWNTs are needed for percolation. Even CB percolates at very low concentrations commonly less than 1.0 wt%. Both are well below that predicted by percolation theory, and are a result of flocculation. Shaffer pointed out the sensitivity of the percolation threshold in epoxies to the temperature and mixing conditions both during processing and curing, and suggested aspects of dynamic colloid theory, such as flocculation, to explain them[159]. The onset of flocculation was coincident with the addition of the amine hardener, and could further be controlled by changing the conditions of pre-cure mixing (shear) and temperature (viscosity). Lower viscosity and "softer" mixing enabled more efficient agglomeration of the MWNTs leading to a lower percolation threshold. Harder mixing tended to break up the agglomerates, which led to higher percolation thresholds. Here, the formation of agglomerates improves electrical performance while their formation reduces mechanical performance, especially when the agglomerates become appreciable in size.

Mechanism of Charge Transfer
Beyond the percolation threshold, the electrical conductivity of CNT (and CB) composites has been shown to scale with the concentration by[28, 30]:

(1-9) $\sigma = \sigma_0 (p - p_c)^t$

Where σ is the composite conductivity, p is the mass or volume fraction of filler, p_c is the percolation threshold and σ_0 and t are constants. Theoretically, t should be 2 (for 3-dimensional percolation), and σ_0 should be the conductivity of the filler phase. Many of the reports found t values quite close to 2. However, σ_0 was typically much lower, which is attributed to high contact resistances between the filler particles (between CNTs). At the macro-scale, concentrations higher than the percolation threshold increase the number of conductive pathways, which enables more current to flow within the same cross-sectional area under constant potential. This increase in conductivity, however, approaches an upper limit as the increasing pathways are balanced by the increasing number of contacts with high contact resistances. Table 1.3 shows that by 1.0 wt.%, MWNT composites typically have resistivities on the order of 100 Ωcm, whereas CB composites tend to have much higher resistivities (resistivity is the inverse of conductivity). Given the intrinsic resistivity of MWNTs to approximately 10^{-3} Ωcm (Table 1.1), one may expect that much higher composite conductivities could be achieved with sufficient loading/orientation, or by surface treatment of the MWNTs.

At the micro-scale, electrons in the graphitic π orbitals are set in motion by the applied field, but must transfer from particle to particle or CNT to CNT. Macroscopically this sets up a contact resistance. But at the quantum level, the definition of inter-particle contact becomes a bit vague. In 3 dimensions, the average gap width between conductive particles is inversely proportional to the cube root of the volume fraction of particles. The conductivity of a single tunnel junction is proportional to this gap width[28]. Numerous reports conclude the mechanism of charge transfer in CNT composites to be an effect of quantum mechanical tunneling of electrons through potential barriers imposed by thin layers of polymer between CNTs[57, 100, 158]. In all cases a plot of ln σ vs $p^{-1/3}$ was linear, indicating tunneling limited electron transport. This serves as a basis for the overall contact resistance. Furthermore, Yoon reported that functionalizing the CNT surface or otherwise increasing its affinity to the insulating matrix, reduced the overall conductivity measured due to polymer wrapping of the tube increasing the gap width[28].

Conner further investigated the mechanism of charge transport in CB/PET composites by measuring the AC conductivity as a function temperature[162]. They found that at temperatures greater than 45K, thermal fluctuation induced tunneling was the mechanism for charge transport. Thermal fluctuation refers to changes in the potential barrier for tunneling according to $\varepsilon_0 \pm kT$. At lower temperatures conventional tunneling dominated as the fluctuations become smaller in magnitude.

1.5 Thermal Conductivity

Polymers are notoriously poor conductors of heat (<1 W/mK). Combined with their tendency to soften or creep at moderate temperatures, this represents a major limiting factor in their application. Increasing the thermal conductivity of polymers by fabricating CNT composites is in many ways an analogue to increasing the electrical conductivity.

However, even though the formation of a conductive network through the polymer matrix occurs, verified by the stark increase in electrical conductivity, no such analogue in the thermal conductivity occurs. Many have reported modest increases in thermal conductivity for randomly dispersed CNT composites (Table 1.4). Combined with the large intrinsic thermal conductivities of CNTs (Table 1.1), this suggests the mechanism for thermal energy transport in CNT composites is very inefficient.

Table 1.4 Thermal properties of carbon-filled composites

Matrix	Filler	Loading Wt.%	k_c (W/mK)	R_k (m^{2}K/W)	Ref.
PMMA	SWNT	10	+250%		[163]
Epoxy	MWNT	0.5	+14%		[30]
	SWNT	0.5	-6%		
PMMA	SWNT	2	+20%		[100]
Epoxy (infiltrated)	SWNT	2.3	+220%		
Phenolic resin (carbonized)	MWNT	10	+57%		[164]
Epoxy	SWNT	1.0	+125%		[165]
	VGCF	1.0	+45		
Epoxy	MWNT	0.3	+4%		[57]
	CB	0.3	+1%		
Epoxy (aqueous)	SWNT	10	+64%	2.6×10^{-8}	[166]
Epoxy (DMF)		0.5	+27%	2.4×10^{-9}	
Water	CNT			8.3×10^{-8}	[167]
Graphite	MWNT interface	N/A	+363%		[168]
Aluminum		N/A	+385%		
Si Wafer	MWNT interface	N/A		+357%	[169]

Increases in thermal conductivity and the interfacial thermal resistance for several composites systems are shown.

Modest increases in the bulk thermal conductivity for randomly dispersed CNT composites have prompted some to investigate the thermal properties of aligned MWNT arrays as heat conductors for macro-scale interfaces (Table 1.4). Here CVD- synthesized aligned MWNT arrays may prove particularly useful due to the fact that when sandwiched in an interface, they are inherently positioned to conduct heat along their axes where transport is favorable due to anisotropic considerations.

Mechanism of Heat Transport
Unlike electron transport, tunneling of heat does not occur. Transport of thermal energy through CNT polymer composites occurs by phonon transfer[163, 166]. Here, the limiting step is transferring the vibrational energy in the polymer matrix to the embedded CNTs. The disparity between CNT and polymer moduli imparts a significant acoustic mismatch between the phonon frequencies. Primarily low frequency acoustic phonons dominate in the polymer phase heat transfer process, and must be transferred to the embedded CNTs across the interface. CNTs, then, although capable of efficiently transporting heat via higher frequency phonons, are limited by weak coupling to the polymer by only a few low frequency phonon modes[163]. This serves as a basis for the overall thermal resistance at the interface.

An effective medium approach (EMA) has proven useful to model CNT-polymer composite thermal conductivity, and to probe the effect of interfacial thermal resistance. Nan used such an approach to model the effect of interfacial thermal resistance in CNT polymer composites[21]. For small loadings of CNTs (negligible CNT-CNT interaction), with the thermal conductivities of the CNTs much higher than that of the polymer matrix, and with high aspect ratios of the embedded CNTs (p>1000), the thermal conductivity of a polymer composite containing randomly dispersed CNTs can be modeled as:

$$(1\text{-}10) \quad \frac{K_e}{K_m} = \frac{3 + f(\beta_x + \beta_z)}{3 - f\beta_x} \qquad \text{with } \beta_x = \frac{2(K_{11}^c - K_m)}{K_{11}^c + K_m} \qquad \beta_z = \frac{K_{33}^c}{K_m} - 1$$

K_e is the effective thermal conductivity of the composite, K_m is the matrix thermal conductivity, and f is the volume fraction of CNTs. If the CNTs are assumed to be coated with a thin layer of polymer, which induces an interfacial thermal resistance, K_{11}^c and K_{33}^c are the transverse and axial thermal conductivities of the coated CNT respectively and can be written as:

$$(1\text{-}11) \quad K_{11}^c = \frac{K_c}{1 + \dfrac{2a_K}{d}\dfrac{K_c}{K_m}} \qquad \text{and} \qquad K_{33}^c = \frac{K_c}{1 + \dfrac{2a_K}{L}\dfrac{K_c}{K_m}}$$

Here K_c is the axial CNT thermal conductivity, and d and L are the CNT diameter and length respectively. a_K is called the Kapitza radius, and is determined by the interfacial (or Kapitza) thermal resistance, R_K through:

$$a_K = R_K K_m$$

The effective thermal conductivity of the composite can be simplified in the dilute limit (f < 0.01) by:

$$(1\text{-}12) \quad \frac{K_e}{K_m} = 1 + \left(\frac{fp}{3}\right)\left(\frac{\dfrac{K_c}{K_m}}{p + \dfrac{2a_K}{d}\dfrac{K_c}{K_m}}\right)$$

The model then takes into account the effects of CNT diameter, aspect ratio, volume fraction, interfacial thermal resistance, and the ratio of the CNT-matrix thermal conductivities. Using values from Table 1.1 and Table 1.4 for the CNT thermal conductivity and interfacial thermal resistance, experimental data have been well-modeled, which underscores the importance of taking the interfacial thermal resistance into account[21]. Other similar models have been developed taking into account the waviness of the embedded CNTs[35].

1.6 Conclusions

CNT-polymer composites are an emerging class of composite materials with unique and promising properties. Considering the issues of CNT dispersion, orientation and processing, significant progress has been made in realizing their potential to enhance the properties of matrices to which they are added. The dependence of the CNT-polymer composite properties on these issues, as well as others such as CNT diameter, length, and interfacial effects, has been recognized and used to develop models to predict and optimize variables for maximum composite performance.

Further understanding of mechanical, thermal and electrical properties of CNT composites promises to result in wide application of truly multifunctional materials. CNT-polymer composites can lead to reinforced polymers that are light, operate at high heat loads, have tunable electrical conductivities, and can shield EMI radiation simultaneously. CNT-polymer composites will undoubtedly advance the engineering capabilities of polymer composites.

Preface of Experimental Work

In the subsequent three chapters, the results of investigations into three separate carbon nanotube composite properties are presented and discussed. Within each composite system, key properties were studied, which in total, represent a majority of envisioned carbon nanotube composite applications.

In Chapters 2 and 3, the application of carbon nanotubes for mechanical reinforcement is explored. More specifically, Chapter 2 deals with the tensile properties of multiwall carbon nanotube (MWNT) composite carbon fibers derived from polyacrylonitrile precursor matrix fibers. Here the effects of the MWNTs on the elastic modulus, break strength, and strain energy density (toughness) of the resulting composite carbon fibers are presented and discussed. In Chapter 3, results of fatigue performance of MWNT composite poly(methyl methactrylate) are presented and discussed. Here, focus was shifted to study the effect of MWNTs in a composite where plastic flow and internal damage dominate the desired properties. Chapter 4 then addresses the electrical and thermal conduction properties of a MWNT-epoxy composite. In this case, the transport of electrons and heat throughout conductive MWNT networks was examined, and key parameters such as the electrical and thermal conductivity are reported and discussed.

Each chapter is dedicated to address the performance of a particular MWNT composite on the properties of interest for the respective material system. In this larger sense, this dissertation, including the introductory literature survey, represents a body of work that specifically targets and addresses the key scientific questions relevant to the application of MWNT composites in engineering materials.

2.1 Introduction

The attention on nanometer-scale carbon filaments has continued to expand from early pioneering work on high strength carbon whiskers by Bacon_[34]_, and vapor grown concentric graphitic micro-fibers by Oberlin and Endo_[170]_, to the current explosion in carbon nanotube research stemming from work by Iijima_[1]_. The extended-fullerene model of the carbon nanotube (CNT) attracted great interest spanning from fundamental physics to composites application_[3, 138]_. Large interest currently remains in successfully demonstrating carbon nanotube composite materials that effectively build on the unique mechanical properties of the CNTs. Specific focus has been on the unprecedented, on-axis, high strain to failure of CNTs; translating directly into extremely high tensile strengths owing to their high moduli. Strength measurements have been carried out separately by Yu et. al._[24]_, Demczyk et. al._[25]_, and recently by Wagner et. al._[26]_. In tensile tests of individual CNTs, Wagner reported a distribution of tensile strengths of individual multiwall carbon nanotubes (MWNTs) with an average of 109 GPa. This magnitude of break strength closely approaches the theoretical limit of carbon materials, and demonstrates the mechanical potential of such materials, especially when compared to commercial high-strength carbon fiber_[171]_, _6.37 GPa_, and graphite whiskers_[34]_, _20 GPa_. However, the distinct disadvantage of CNTs as reinforcement in practical size structural parts includes difficulty in achieving uniform dispersion in the continuous phase and the discontinuous nature of CNT reinforcement.
Meanwhile, the field of continuously processed carbon fiber, particularly high performance pitch- and polyacrylonitrile (PAN)-based carbon fiber, has advanced to the point of common industrial-scale applications in high modulus, high strength, lightweight materials. This chapter reports investigations on combining the mechanical advantages of carbon nanotubes with the practical relevance of high performance, continuous carbon fiber. Specifically the processing and tensile properties of MWNT composite PAN-based carbon fiber are explored.

2.2 Experimental

Throughout this chapter, the details of the carbon fiber processing have been omitted in accordance with Federal Export Control Laws.
In this study, composites were produced by dispersing multiwall carbon nanotubes (MWNTs) homogeneously throughout a polyacrylonitrile (PAN) spinning dope, spinning composite precursor fibers, and converting them into composite carbon fibers by thermal treatments. The mechanical properties of the MWNT-containing composite carbon fibers were compared to control carbon fibers prepared from PAN alone. In this approach the resulting carbon fiber is a composite itself; a continuous matrix of PAN-based carbon filled with aligned, discontinuous nano-filaments of carbon. It is a hierarchical carbon fiber composed of nanometer-scale carbon filaments axially aligned and encapsulated within a micrometer-scale carbon filament. In this way, the desirable on-axis properties of the MWNT could be most efficiently transferred to the continuous matrix fiber, and

the bridging of length-scales towards a useable size structural part could be attained. It was envisioned that enhancement of the matrix carbon fiber could be realized by two mechanisms. The first was that the MWNTs would function as reinforcing nano-fibers enabling on-axis stress transfer from the PAN-based carbon matrix. This gels with classical fiber composite theory in which high modulus, embedded fibers, disproportionately take on the applied stress, in turn, increasing the composite modulus. The second mechanism was that the MWNTs would function as seeds for aligned, templated growth of the carbonizing PAN matrix, or as a nanoscale pre-form for the crystalline structure of the final carbon fiber towards highly curved, long crystalline domains aligned with the fiber axis. It is exactly this crystalline morphology which has been linked to higher strength PAN-based carbon fiber, an effect that is primarily due to increased tortuosity of crack propagation transverse through highly curved graphitic carbon domains which span for long distances uninterrupted down the fiber axis[12]. Given the fact that the ratio of the MWNT modulus to a carbon fiber modulus is in the single digits, and that many have report observing polymer sheathing of MWNTs in composites, this second mechanism was of much higher interest.

2.2.2 Materials

The MWNTs used were produced in-house by the CVD method over quartz substrates using xylene and ferrocene as the major carbon source and catalyst respectively[14]. The MWNTs were further treated to 2800°C to remove residual iron catalyst, and to anneal defects in their graphitic structure[172]. Concentrated PAN solutions or spinning dopes were prepared by the dissolution of commercially available, homopolymer PAN powder in dimethylacetamide (DMAc), forming a homogeneous solution with @wt.% PAN. To make the MWNT composite spinning dopes, the annealed MWNTs underwent a surface treatment process to facilitate homogeneous dispersion followed by ultrasonication in DMAc using a combination of a high power (20kHz) wand sonicator and a low power (40kHz) sonicating bath. PAN powder was later added, and the complete dispersion was mixed using a Silverson laboratory shear mixer. In other cases, the MWNT/DMAc dispersions were allowed to sediment by centrifugation for 1hr at 10**G**, in which case only the supernatant of MWNT/DMAc was used. This was done in an effort to minimize agglomerated MWNTs entering into the spin dope. Each of the dispersions, representing a specific parent spin-dope of known MWNT concentration and/or sedimentation process, was transferred to a glass syringe, heated, and spun into precursor fiber.

2.2.3 MWNT surface treatment

The MWNTs were dispersed ultrasonically in a mixture of 90:10 DMAc to distilled acrylonitrile monomer to which 1% AIBN was added as an initiator. The mixture was then heated under sonication to 60°C to allow the monomer to polymerize in situ with the dispersed MWNTs. The MWNTs were then repeatedly vacuum filtered and washed in DMAc to remove excess, un-bound polymer from the MWNT surfaces. The MWNTs were then carefully dried. TGA analysis indicated less than 2wt% of the MWNTs was polymer, which was barely discernable on the MWNT surfaces by SEM. This process, however, was effective for promoting homogenous dispersion of the MWNTs.

2.2.4 Fiber Processing

PAN dopes were solution spun into precursor fiber using a dry-jet wet spinning method, yielding continuous precursor fiber of kidney-beaned shaped cross-section and approximately 20 μm (equivalent circular area) diameter. The coagulation rates and draw ratios were held as constant as possible between control and MWNT composite dopes as depicted in Figure 2-1.
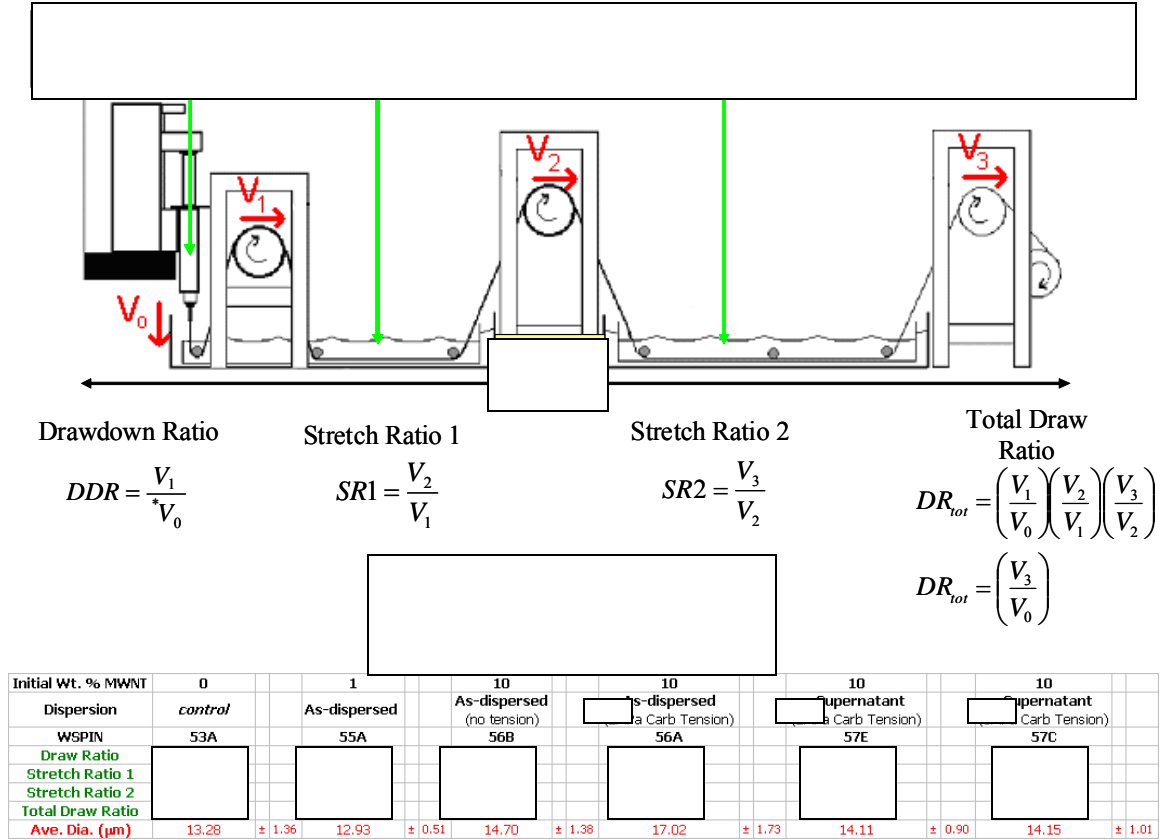

Drawdown Ratio

$$DDR = \frac{V_1}{{}^*V_0}$$

Stretch Ratio 1

$$SR1 = \frac{V_2}{V_1}$$

Stretch Ratio 2

$$SR2 = \frac{V_3}{V_2}$$

Total Draw Ratio

$$DR_{tot} = \left(\frac{V_1}{V_0}\right)\left(\frac{V_2}{V_1}\right)\left(\frac{V_3}{V_2}\right)$$

$$DR_{tot} = \left(\frac{V_3}{V_0}\right)$$

Initial Wt. % MWNT	0		1		10		10		10		10	
Dispersion	control		As-dispersed		As-dispersed (no tension)		As-dispersed (a Carb Tension)		Supernatant (a Carb Tension)		Supernatant (Carb Tension)	
WSPIN	53A		55A		56B		56A		57E		57C	
Draw Ratio												
Stretch Ratio 1												
Stretch Ratio 2												
Total Draw Ratio												
Ave. Dia. (μm)	13.28	± 1.36	12.93	± 0.51	14.70	± 1.38	17.02	± 1.73	14.11	± 0.90	14.15	± 1.01

Figure 2-1 Fiber processing and processing parameters

Spun tows of fiber were collected in bulk as a hoop of intertwined continuously looped single filament, which enabled the hoop to be pulled tight between two rods attached to an adjustable length rack as shown in Figure 2-2. The stretched tows therefore conformed to the shape of two curved ends between which were straight fiber sections. In this way, usable straight sections of the tows were held, under tension (without unraveling), at constant length during the subsequent stabilization step. Stabilization was carried out by heating in a forced air oven at @°C/min to @°C followed by a @hr dwell, then a second heating ramp at @°C/min to a final temperature of @°C. The color of the neat PAN tows changed from shiny-white to shiny-black during stabilization (MWNT composite PAN tows were shiny black as spun).

Figure 2-2 Constant length stabilization rack
On the left are shown MWNT/PAN composite fibers prior to stabilization, and on the right are neat PAN fibers.

Stabilized tows were then transferred to a horizontal tube furnace in which they were again suspended under tension using graphite hooks in a flowing Ar atmosphere as shown in Figure 2-3. One hook was fixed to the inlet cap of the furnace and other to the fiber tow. The second hook was fixed to the remaining end of the tow, then routed through a septum in the outlet cap by a steel wire (outside the hot zone), which in turn was fixed to a stationary force transducer. In this way, force vs. temperature curves were generated, in-situ, during the carbonization of the hoop-tows of fibers. Each tow was heated to @°C at @°C/min for carbonization. The, changes in mass, length, and carbonization tension of each of the tows were recorded.
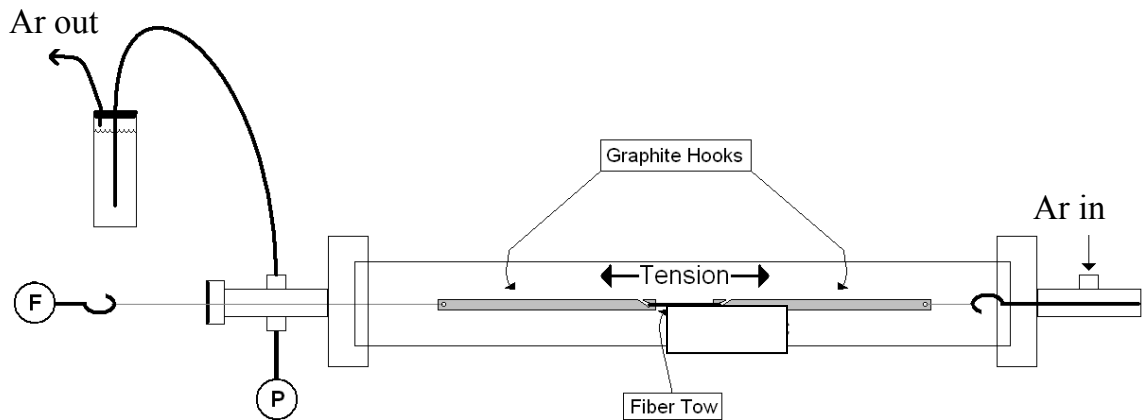

Figure 2-3 Carbonization furnace and tension measurement
During carbonization, the fiber tow was tensioned to a known initial tension. Further tension generated upon fiber shrinkage was recorded with a force transducer in-series with the carbonizing fiber tow

2.2.5 Fiber Testing

Throughout processing, the fiber tows retained their extended hoop shape and kidney-bean cross-sections. Fiber coalescence was not a problem. For tensile testing, a straight section of the carbonized tow was cut, individual fibers were gently removed, mounted on paper cards with cyanoacrylate adhesive, and tested to failure following ASTM D3379-75. A cross-head speed of 0.1 mm/min and a $1.47N_{max}$ load-cell was used for all testing. The kidney-bean shape of the fiber cross-section complicated accurate cross-sectional area measurement of each individual fiber subjected to tensile testing.

Therefore a representative, average cross-sectional area for each tow was used in the tensile testing of that particular tow. Bundles of fiber were cut and imaged end-on by SEM. The length scale generated by the microscope was calibrated with a standard sample. The acquired digital micrographs were then manipulated with an imaging software package (SPOT advanced), which had been calibrated to relate the number of pixels with the actual length scale. This enabled the number of pixels encompassed within the perimeter of individual fibers, viewed end-on, to be converted to square micrometers. The representative cross-sectional area of each of the tows, taken as an average from 30 individual fibers, was then converted to the diameter of an equivalent circle, which simplified comparing the experimental fibers to commercial fibers.

2.3 Results & Discussion

2.3.1 Fiber Structure

Scanning electron microscopy of the fracture surfaces of the MWNT composite carbon fibers revealed a high degree of alignment of the embedded MWNTs with the axis of the matrix carbon fiber as shown in Figure 2-4. Alignment of MWNTs in fibers has been attributed to the large shear and elongational forces imparted to the fiber during the spinning process, and maintained through thermal processing by tension*[114, 173]*. SEM micrographs also indicated the MWNTs were not agglomerated in pockets of high density in the cross-section of the fibers. The homogeneity of the MWNT dispersion in the original spinning dope was maintained through processing. The SEM micrographs also confirmed that the high degree of dispersion homogeneity became locked into the fiber structure, indicating that the MWNTs do not migrate into agglomerates during the conversion of the matrix PAN fiber to carbon.
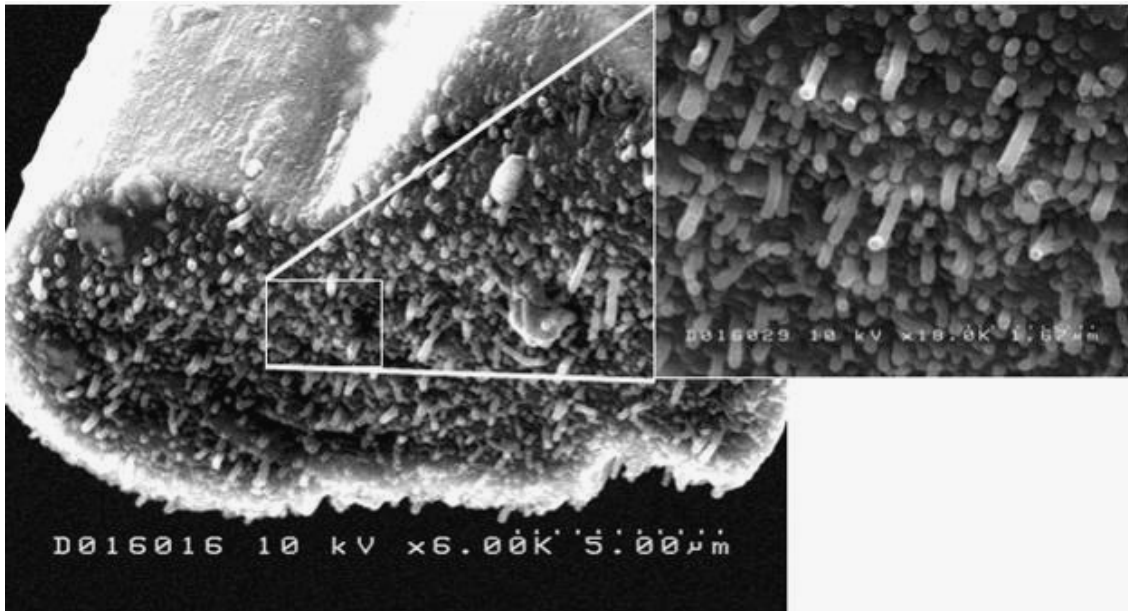

Figure 2-4 SEM of a MWNT composite carbon fiber fracture surface
SEM micrographs show a typical fracture surface of a PAN-based carbon fiber containing approximately 20 wt.% MWNTs. The above fiber began containing 10 wt.% MWNTs, but conversion of the original PAN fiber matrix to carbon is accompanied by approximately a 50% mass loss.

High resolution field emission SEM further revealed interesting smaller features present at the fracture surface of the MWNT composite carbon fibers as shown in Figure 2-5. The presence of both protruding MWNTs and holes indicated that MWNT pull-out during tensile fracture had occurred at numerous sites throughout a given cross-section. The occurrence of pull-out suggested that the interfacial bonding between the MWNTs and the carbonized PAN matrix was not strong. Therefore the MWNTs were not efficiently reinforcing the matrix carbon fiber. However, closer observation revealed that in many cases a thick layer of matrix carbon was adhered to the surface of the MWNTs, and this coating remained intact and bonded to the protruding MWNTs. This effect is circled in yellow in Figure 2-5. The embedded MWNTs at the center of the coatings are also visible. In what may be a related effect, annular rings formed around the holes left behind by pulled out MWNTs. This effect is shown in blue in Figure 2-5. This phenomenon is reminiscent of stress-graphitization, which has been shown to occur at the interfaces of standard diameter carbon fibers and a carbonizable matrix during heat treatment to form carbon/carbon composites[174-176].
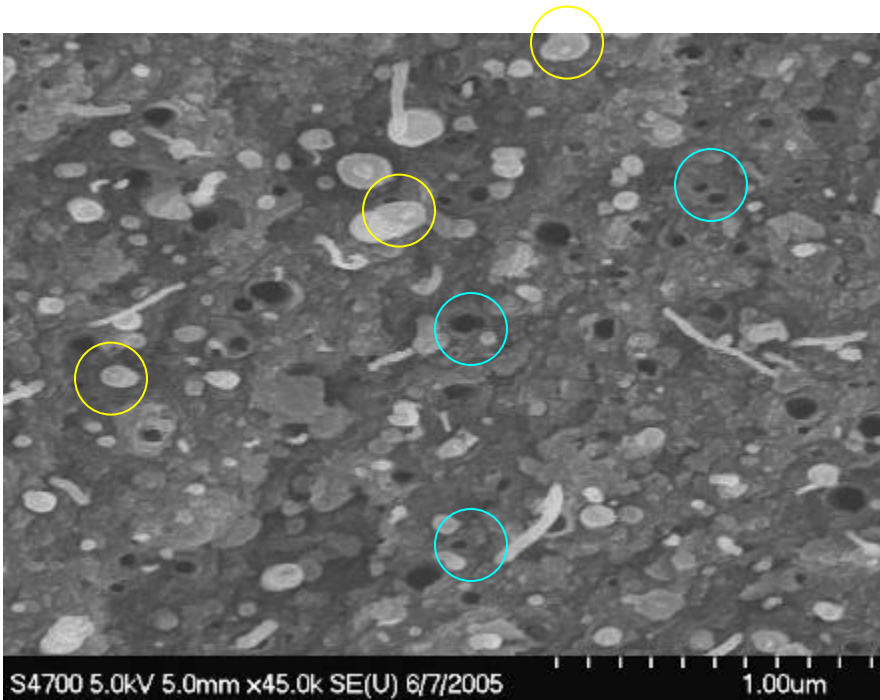

Figure 2-5 High Resolution SEM of a MWNT composite carbon fiber fracture surface
High resolution, field emission SEM micrograph shows the fracture surface of a MWNT composite PAN-based carbon fiber. The yellow circles highlight MWNTs which demonstrated a thick layer of carbon remaining adhered to the protruding MWNTs. The blue circles highlight corresponding holes, which demonstrate concentric stress graphitization annuli. In many cases, failure has not occurred at the interface of the MWNT surface, but at the interface with the adhered carbon layer and the bulk carbon matrix.

In cases where protruding MWNTs were coated with a thick layer of carbon, abnormally large outer diameters were observed, which furthermore matched the abnormally large diameters of holes in the fracture surface. These data suggested that interfacial failure was occurring not between the MWNT surface and the carbon matrix, but between the interphase carbon layer and the bulk carbon matrix. This phenomenon has been previously reported in polycarbonate- and poly(vinyl-alcohol) - MWNT composites, and

it has been interpreted as a distinct third phase induced by the presence of the MWNT surfaces*[50, 92]*. Similarly, Kumar observed similar structures in SWNT-PAN-based composite carbon fiber, and found them to be responsible for increasing the graphitic character of the final fibers and decreasing their tendency to shrink during stabilization*[113]*. Here relatively clean holes and MWNTs coated with a sheath of carbon remain. This suggests that the MWNTs selectively interact strongly with the nearby matrix, perhaps to the point of phase separating in the final carbon fiber. The implications of these interphase structures on the properties of PAN-based carbon fibers are a topic of continued investigation, the importance of which will be addressed later.
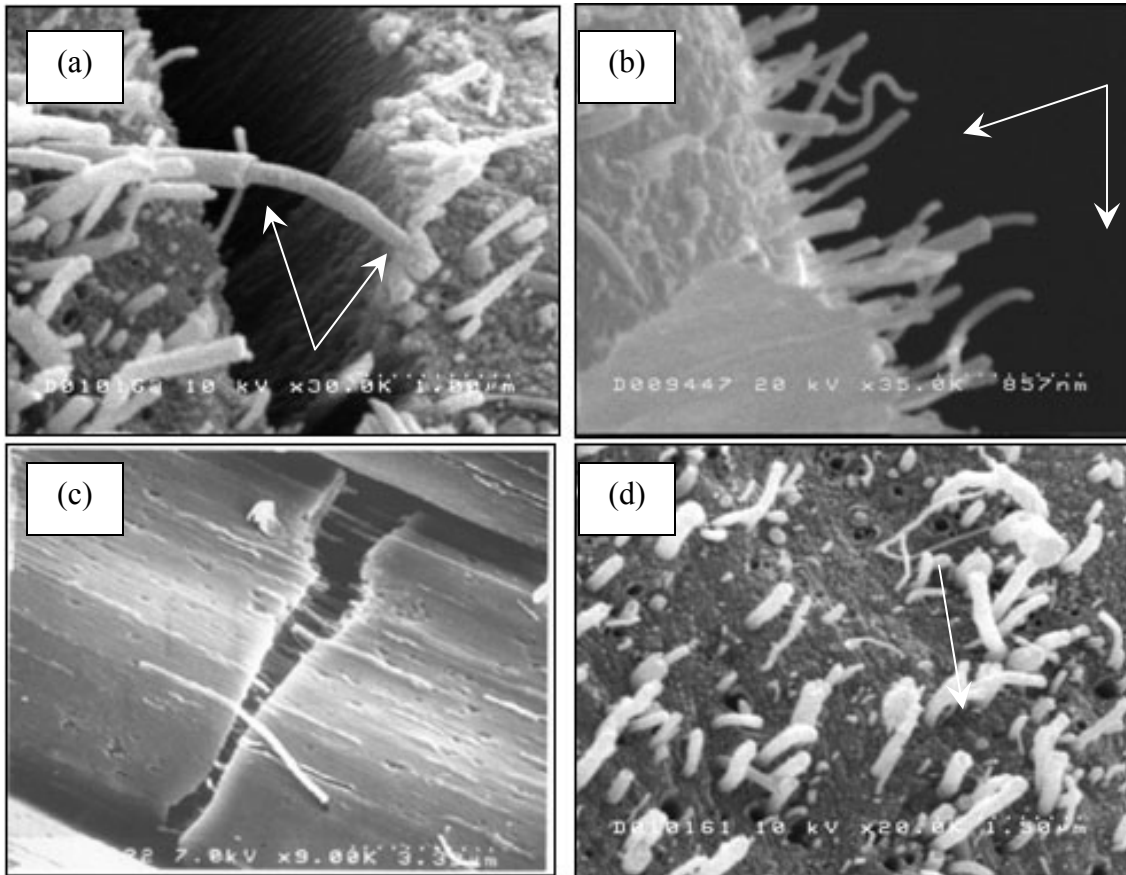

Figure 2-6 SEM observation of reinforcement mechanisms
SEM micrographs are shown above which indicate mechanisms of reinforcement. Telescoping of protruding MWNTs is shown by the white arrows in (a), (b), and (d). MWNTs serving to bridge a crack through the cross section of a fiber is shown in (c)

Further SEM analysis of the fracture surfaces were carried out in an effort to observe signs of reinforcing mechanisms such as telescoping of protruding MWNTs and crack bridging by MWNTs. These are shown in Figure 2-6. The telescoping of MWNTs under tensile loads is thought to occur after the initial fracture of the MWNT's outer shell, indicative of strong bonding with the surrounding matrix. Subsequently, the inner shells of the MWNT are slightly dragged along with the outer shell by weak van der Walls forces until they ultimately fracture, or are left behind at a defect site. Evidence of this

process in these fibers was not frequent, and rarely observed, as shown in Figure 2-6 (a), (b), and (d) by the white arrows. MWNTs serving to bridge a completely propagated crack are shown in Figure 2-6 (c).

2.3.2 Carbonization Tension

During the carbonization of stabilized MWNT composite fibers (@ºC/min to @ºC), the tension generated in the tow during heating was recorded using the set-up described in Figure 2-3. All temperatures are approximate within @°C, and spikes in the curves shown in Figure 2-7 are due to partial and/or complete fracture of the carbonizing fiber tow. A known initial tension was allowed to equilibrate prior to heating. Independent of the initial tension, all tows demonstrated an increase in tension beginning at @°C, which increased to a local maxima at @°C. This is likely due to shrinkage of the PAN molecules as they undergo residual stabilization reactions. Subsequently the tension

(A)

Shrinkage Stress vs. Carbonization Temperature

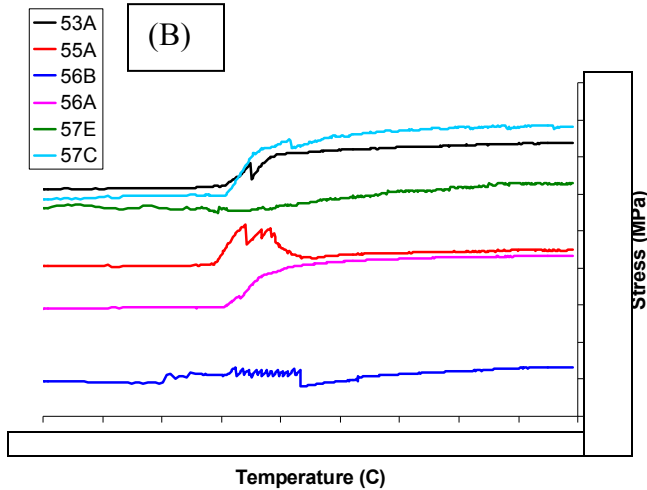|	
—53A	Pure PAN
—55A	1 wt.% MWNT (as-dispersed)
—56B	10 wt.% MWNT (as-dispersed)
—56A	10 wt.% MWNT (as-dispersed) – low draw ratio
—57E	10 wt.% MWNT (dispersed from supernant)
—57C	57E (higher initial tension)

Stress (MPa)

Temperature (C)
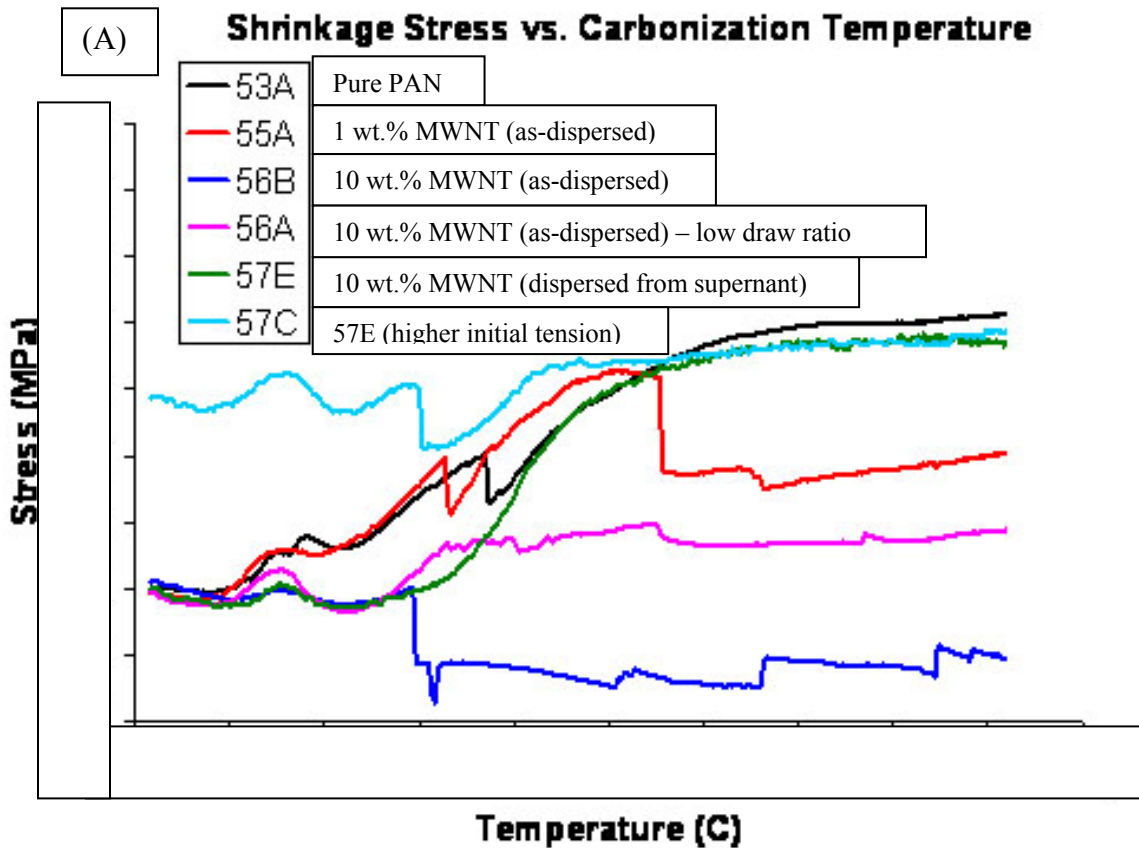
Figure 2-7 Tow tension during carbonization
(A) The tension generated during carbonization of several MWNT composite PAN-based fibers are shown.
(B) Further tension generated during cool-down of the fiber tows is shown.
(the identification numbers shown in the legend are explained further in the next section)

decreased to a local minima at @°C. Here the stabilized fibers soften just prior to carbonization as they are exposed, for the first time, to temperatures above @°C. Further heating resulted in a gradual increase in tension to a stable maximum at approximately @°C, which no longer increased with further heating to @°C. The temperature corresponding to the maximum rate of increase in tension, in all cases, appeared to be approximately @°C. Upon cooling, the tows displayed an increase in tension beginning at approximately @°C, which corresponds well with the temperature at which the carbon initially formed, and is likely due to thermal contraction considerations.

Pure PAN Fiber

Pure PAN Fiber
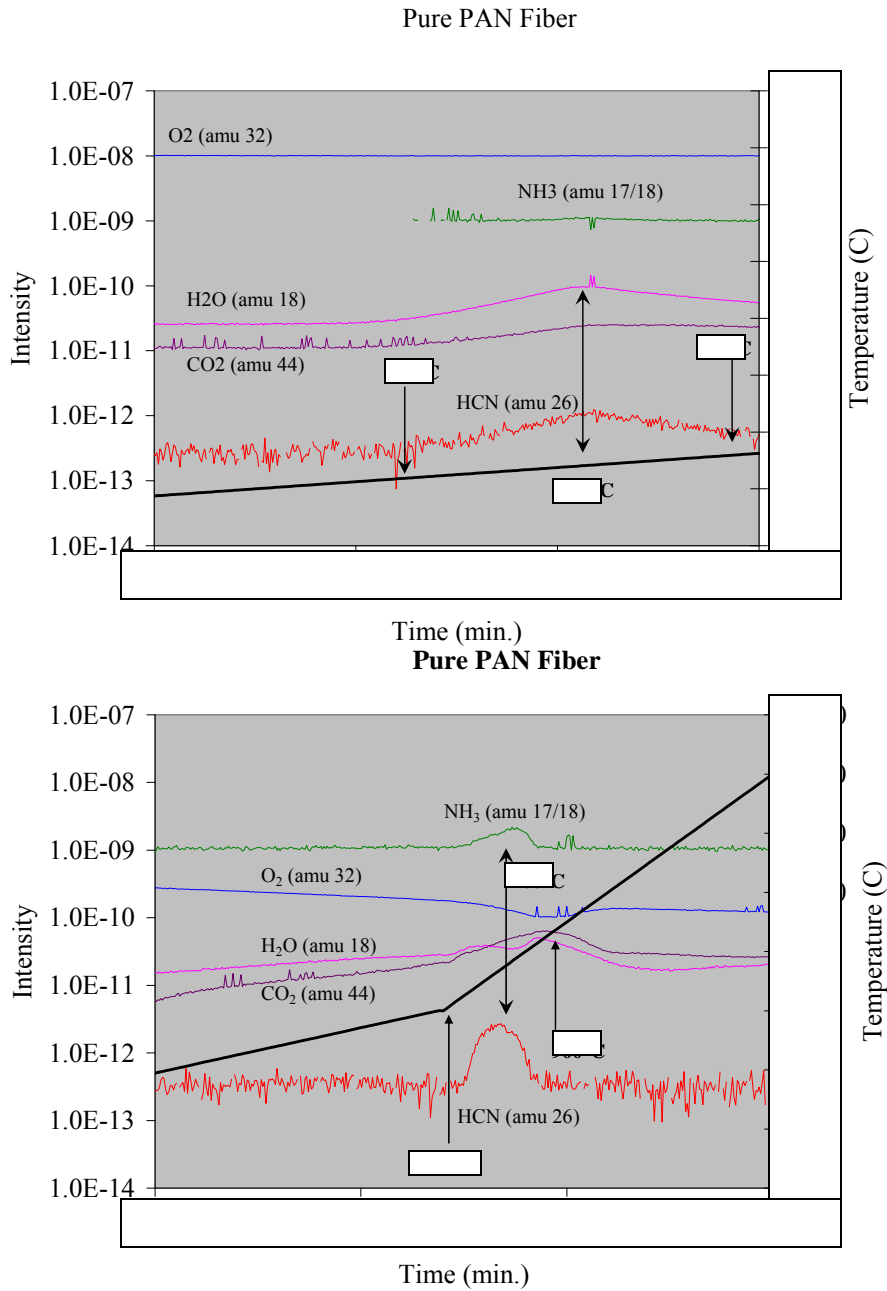
Figure 2-8 Evolution of volatiles during carbonization

TGA/MS experiments indicate a correlation between the tension and the generation of volatile compounds from the fiber as conversion to carbon proceeds (Figure 2-8). The low temperature initial peak in tension corresponds to the generation of HCN and H_2O, which are indicative of residual stabilization reactions occurring in the fiber. At high temperature, all tension is generated by @ºC, which is in agreement with the lack of any further volatiles generated at higher temperatures. Lastly, MWNT composite fibers showed a lower tendency for tension build-up during carbonization, which may reflect the MWNTs functioning to pin molecular relaxation. This is in agreement to

34

observations made by Kumar during the stabilization of SWNT composite PAN fiber[113]

2.3.3 Fiber Properties

The tensile properties of the various fibers tows were determined using the single filament method described in ASTM D3379-75. Ten single filaments were tested from each tow at 20, 30, 40, and 50mm gauge lengths (40 fibers/tow were tested). The break stress was recorded as the quotient of the tension at failure and average filament cross sectional area from the tow. No tensile tests showed any indication of non-linear or plastic deformation. The fiber modulus was corrected for system compliance (see Appendix C), and used in conjunction with the break stress to accurately reflect the break strain and strain energy density. All results are tabulated in Appendix C. Due to the high sensitivity of fiber properties to small changes in processing, relevant processing details are shown with the resulting fiber tensile properties in Table 2.1. The WSPIN# identifies the fiber tow through processing and testing.

Table 2.1 Processing parameters of MWNT composite fiber

WSPIN#	Initial Wt. % MWNTs	Total Draw Ratio	Initial Carbonization Tension (MPa)	Maximum Carbonization Tension (MPa)	Total Shrinkage (%)	Carbon Yield (%)	Equivalent Circular Diameter N=30 (μm)
53A	0.0				9.09	51.03	13.28 ± 1.36
55A	1.0 (as-dispersed)				8.00	50.64	12.93 ± 0.51
56B	10 (as-dispersed)				4.35	56.04	14.70 ± 1.38
57E	10 (supernatant)				5.88	54.60	14.11 ± 0.90
56A	10 (as-dispersed)				5.77	56.11	17.02 ± 1.73
57C	10 (supernatant)				5.77	56.42	14.15 ± 1.01

Processing parameters of the MWNT composite PAN-based carbon fibers are shown.

The average value, compliance-corrected stress-strain curves were generated for each of the fiber tows investigated using the data shown in Appendix C. The curves are shown in Figure 2-9. Three effects were clear in the data. First, there was a distinct and significant reduction in modulus for the MWNT composite fibers, especially those loaded with 10wt% MWNTs. Here, in fact, increases in modulus were expected. Secondly, no significant enhancement in break strength was observed for the MWNT containing fibers. And third, the highly concentrated MWNT composite fibers had higher strain-to-failure than the control fiber. These three properties; modulus, strength, and strain-to-failure will now be addressed separately.
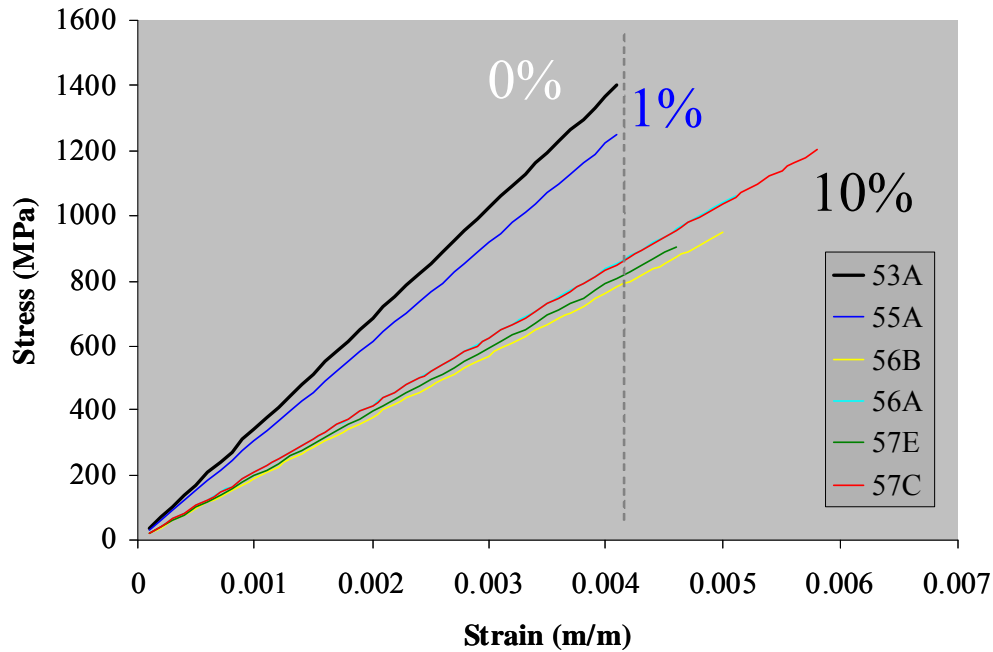
Reconstructed Average Value: Stress-Strain Curves

Figure 2-9 Reconstructed stress-strain curves for MWNT composite carbon fibers

Effect on Modulus

The compliance-corrected moduli for all fibers are shown in Figure 2-10. It is important to note that modulus is a mechanical property not significantly affected by the presence of defects, and is thus an intrinsic material property that is normally measured with higher degrees of accuracy and precision than strength. The 1wt.% MWNT fibers behaved much like the neat fibers in terms of modulus, with a small decrease noted. This suggests that the MWNTs were not prevalent enough to induce an increase in modulus, or that in this relatively high modulus matrix where the ratio of the inherent MWNT modulus to the matrix modulus is only about 2-3, their reinforcing effect is dilute enough to be undetectable, or a combination of the two. At higher MWNT concentrations, there was a significant and unexpected drop in modulus.

The modulus is the change in stress by the change in strain. Limiting the discussion to constant, low strain amongst the fibers, variations in modulus then reflect deviations in the corresponding stress responses of fibers. Significant reductions in modulus can then only occur if the material has inherently changed to a material of significantly different structure, or has a lower effective cross-sectional area. In terms of structure, for carbon fibers, a lower modulus structure would be one in which the carbon crystallites have become less aligned with the fiber axis. Alignment of crystallites in carbon fibers is dominated by precursor chemistry and processing, namely fiber draw ratio. Given that all the fibers tested here were PAN-based, and all processed under nearly identical conditions, decreases in alignment of crystallites with the addition of MWNTs is unlikely. Further, the MWNTs themselves were imaged by SEM to be well-aligned with

the fiber axis. In terms of effective cross-sectional area, however, any internal voids in the fibers can be extremely important for explaining deviations in modulus. Void fraction can be translated to reductions in the amount of load bearing cross-sectional area, as they function as null area. Furthermore, voids typically behave as stress risers at their boundaries which lead to decreases in break stress.
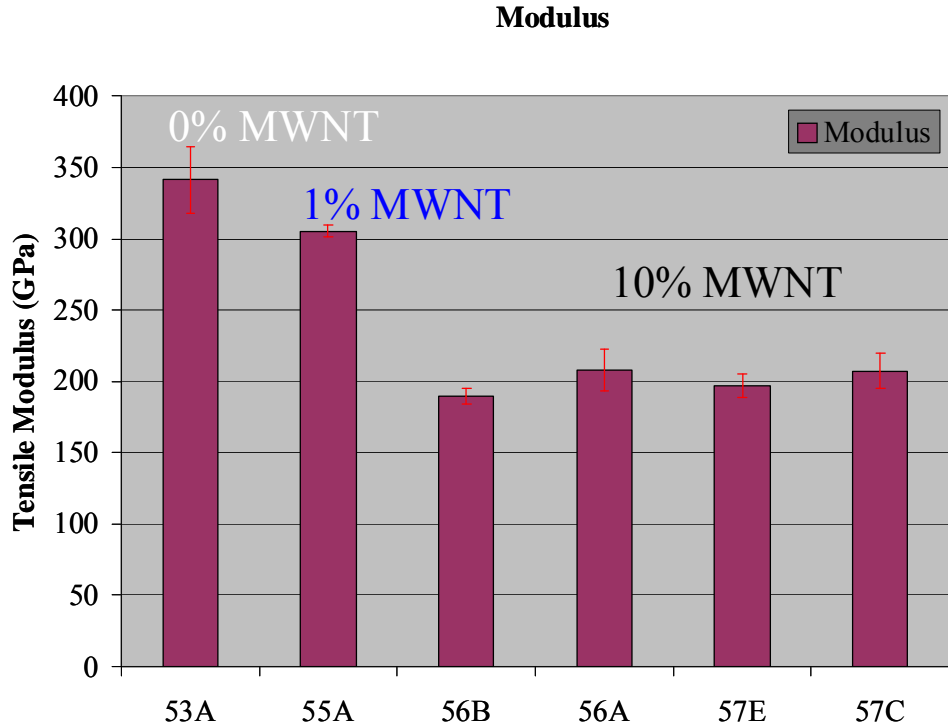
Modulus

Figure 2-10 Tensile modulus of MWNT composite carbon fiber
The average compliance-corrected moduli of the MWNT composite carbon fibers are shown. The error bars show the 95% confidence interval in the data. WSPIN 53A refers to the neat fibers, 55A to 1wt.% MWNT fiber and the remaining are variations of 10 wt.% MWNT fiber. (see Table 2.1 for details on fiber tow composition and processing)

The lower moduli may indicate a massive deficiency in stress transfer to the MWNTs. In this case, the drop in modulus would be occurring due the MWNTs themselves functioning as voids where they may have socketed within the surrounding PAN-based carbon matrix. SEM images of fiber fracture surfaces are helpful for potentially explaining the observed drop in MWNT composite fiber modulus. Shown in Figure 2-11 is a sequence of 0, 1, and 10% MWNT containing composite carbon fibers. The pure PAN-based carbon fiber shows a clean fracture surface with no holes observable. The evolution of holes becomes visible in the 1wt% MWNT containing fiber, and becomes prevalent in the 10wt% MWNT containing fiber (see Appendix B for more SEM images). The volume fraction of these holes, resulting from MWNT pull-out, scales directly with the concentration of MWNT within the fibers. Figure 2-12 analyzes this effect (from Figure 2-5) using high magnification of the fracture surface of PAN-based carbon fiber initially containing 10wt% MWNTs. Here it is visible that in almost all cases, the MWNTs are sheathed with a bound layer of interphase carbon, and that pull-out of the sheath-MWNT occurs resulting in even larger socket holes. Image analysis of the socket

area indicates approximately 20% of the fracture surface is hole area. If one considers that the remaining sheathed MWNTs present in their sockets and visible in the SEM image would represent approximately half of the overall potential for total pull-out, then an additional 20% of the fracture surface would be hole area. In total, this would make for essentially 40% of the original fiber cross-sectional area to have been rendered decoupled from the bulk fiber.
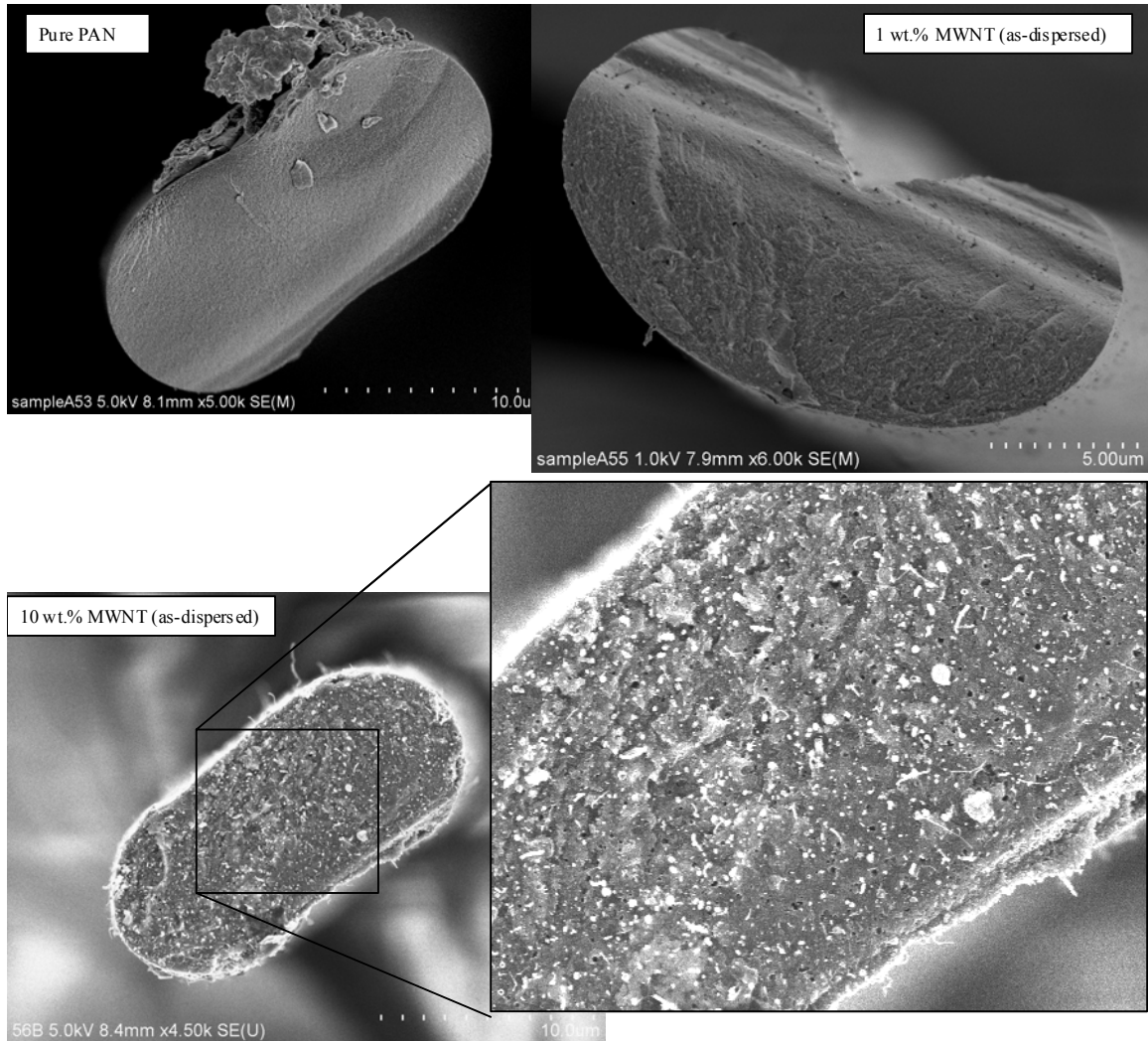

Figure 2-11 Observation of MWNT pull-out sockets in fiber cross sections
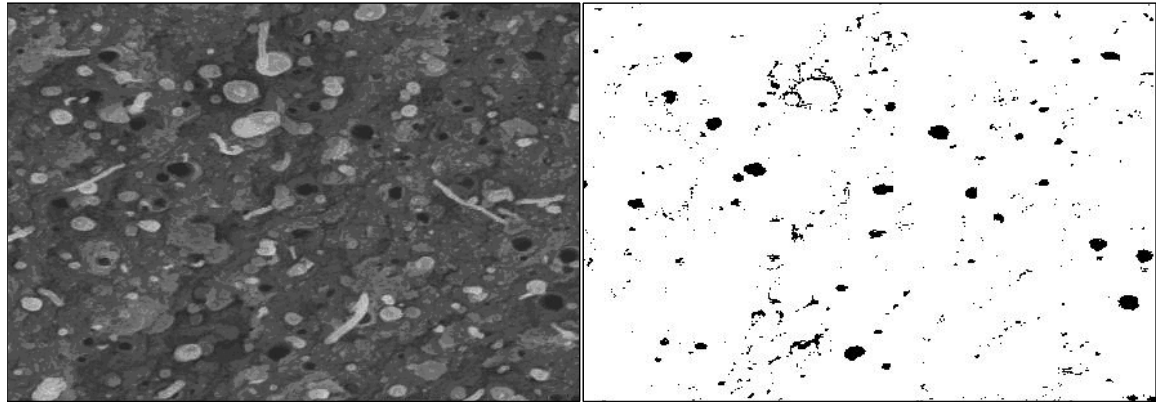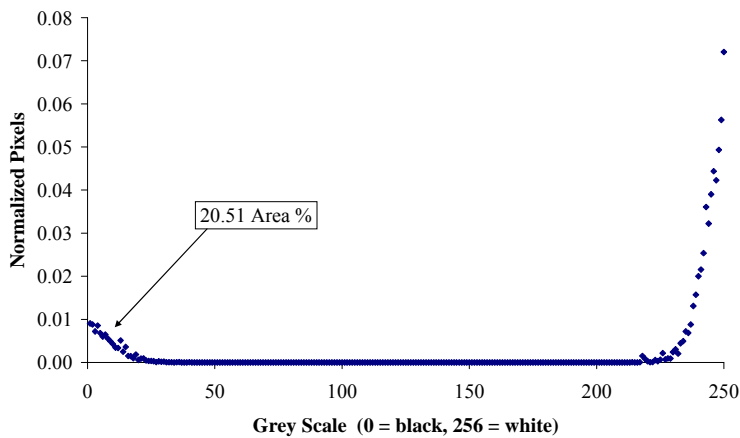
Image Analysis

Figure 2-12 Area fraction of the MWNT pull-out sockets

The effect of hole-area on the modulus of the fiber can be expressed by equation 2-1. Here, the holes, which take no part in bearing the load, are subtracted from the original measured cross-sectional area. It is necessary to note that MWNT composite PAN-based carbon fiber which initially contained 10wt% MWNT, after carbonization would contain approximately 20wt% due to the 50% carbon yield of the PAN matrix. Furthermore, one may expect that the difference in the density between the PAN-based carbon and the MWNT would be quite small such that 20wt% MWNT would be very close to 20vol% MWNT in the final composite carbon fiber. Figure 2-10 shows that an average of the moduli of the concentrated MWNT composite fibers was approximately 200GPa, and that the modulus of the neat fiber was approximately 340GPa.

$$\frac{E_{corr}}{E_{meas}} = \frac{1}{1 - \dfrac{A_{hole}}{A_{meas}}} = \frac{1}{1 - V_{hole}} \approx \frac{1}{1 - (V_{NT} + V_{SHEATH})} \qquad [2\text{-}1]$$

Using data from the image analysis, which indicated that the total volume fraction of holes was approximately 0.4, equation 2-1 predicts that the concentrated MWNT/PAN-based carbon fiber modulus, corrected for hole area, would be 333GPa. This is in good agreement with the modulus of the neat fiber suggesting that socketing of the embedded

39

MWNTs within the PAN-based carbon matrix, as imaged by SEM (Appendix B), played a major contributing role in the significant observed reductions in modulus. Other effects that can potentially reduce the modulus of the MWNT composite fibers are misalignment of the embedded MWNTs with the direction of load, and stress concentration at pull-out boundaries.

At the same time that the embedded MWNTs are functioning as voids (due to lack of bonding), one may expect them to function as stress risers. In this case, qualitatively, a proportionate fraction of the composite fiber may in fact be 'feeling' a higher internal stress due geometrical considerations of the void population. Quantitative analysis into this idea would be rigorous. It stands to reason that one potential explanation for the decrease in the modulus is a combination of weak interfacial bonding between the MWNTs and the matrix carbon, and great potential for debonding leading to a significant portion of stress risers internal to the matrix carbon fiber.

Although debonding was confirmed by SEM imaging in Figure 2-5, suspiciously there were no deviations from linearity in the stress-strain curve. If a large fraction of embedded MWNTs within the composite fiber were debonding during the tensile test, one would expect to see an indication of the event in the stress response. The MWNTs may therefore already be debonded from the matrix carbon fiber prior to testing, during processing under tension, particularly during cooling (Figure 2-7). This effect has been shown to occur in conventional carbon/carbon composites. One case in particular is well-described in a series of papers by Zaldivar, Rellick and Yang *[175, 176]*. There, tows of pitch-based carbon fibers were coated with a poly(arylacetylene) resin matrix and carbonized to varying heat treatment temperatures. In all cases, at very high temperatures (>2400°C), the matrix tended to form a sheath of graphitic carbon within the close vicinity of the embedded carbon fibers, which was attributed to stress-graphitization, and the effective strength utilization of the fibers in the composite was essentially zero because the fibers had decoupled from the matrix. They attributed the decoupling to occur primarily due to stress concentration of the matrix near the fiber surface causing a commensurate reduction in the local volume of the interphase matrix as its density increased, which subsequently caused it to decouple from the bulk matrix. Furthermore, upon cooling, differences in the CTE of the more graphitic carbon accentuated the decoupling.

Here, for MWNT in PAN-based carbon fiber, similar events appear to be occurring. Evidence of matrix transformation is shown in Figure 2-5 where sheathing of the MWNTs with interfacial matrix carbon is visible and is reminiscent of observations by Coleman in a PVA matrix*[138]*. However in contrast to the interphase forming at very high temperatures as observed by Zaldivar et. al., this interphase likely forms in the polymer matrix as reported by Kumar*[113]* due to polymer chains wrapping the embedded carbon nanotubes. Therefore, carbonization temperatures above which are necessary to convert the PAN matrix to carbon can promote preferential densification of the interphase, which in the final brittle carbon matrix, can lead to socket formation and reductions in mechanical properties. There would be great interest, therefore, for future experiments, to evaluate the fiber properties as a function of carbonization temperature.

Effect on Strength

The average break stresses for all fiber types are shown in Figure 2-13. The 1wt.% MWNT fibers again behaved much like the neat fibers with a modest decrease in strength. However, at higher MWNT concentration, all remaining MWNT composite fibers showed a clear decrease in break strength. The only exception to this was (57C) which was initially tensioned to 5MPa during carbonization rather than 2MPa (Figure 2-7). This result is in agreement with the function of the poorly bonded MWNTs forming sockets within the fiber. These sockets would then function as defects at which stress is concentrated and failure is likely at lower applied stresses. Analyzing break strength, correcting for the effective cross-sectional area due to socketing in an identical manner as done for modulus, would predict the break strength of fiber 57C would be 1.96GPa (considering 60% effective cross sectional area and identical break strain as presented if Figure 2-15). This would then be 42% increase in effective break strength. This correction, however, was not further considered to be valid for the analyzing the remaining fibers as the practical break strength remained that calculated using the as-measured cross-sectional area.
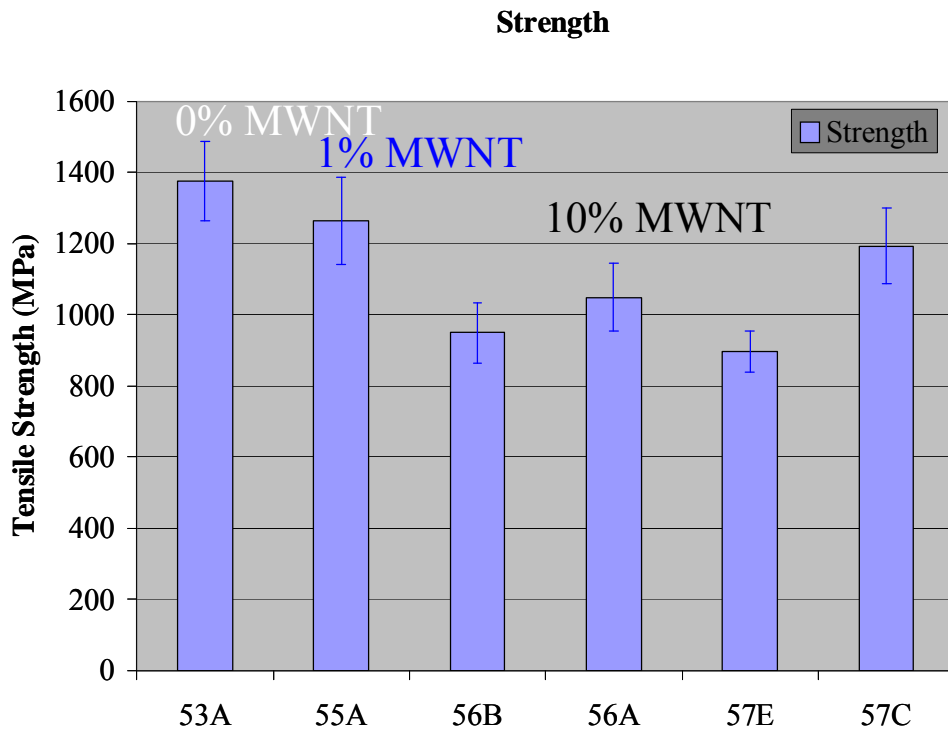
Strength

Figure 2-13 Tensile strength of MWNT composite carbon fiber
The error bars show the 95% confidence interval in the data.

A frequently used method to analyze strength results is through the use of Weibull distribution statistics, which accounts for the fact that break strength is a defect-dominated result and the distribution is thus non-normal. It also enables probability of fiber failure versus applied stress curves to be generated, which for these fibers is shown in Figure 2-14.

Weibull Probability of Failure

Figure 2-14 Weibull probability of failure of the MWNT composite carbon fibers

Changes in the shape of the probability of failure curve are indicative of changes in the homogeneity of the population of failure causing defects within the fiber. Here only small variations in curve shape are noted. However, shifts in the probability of failure curve to lower stresses are indicative of increases in 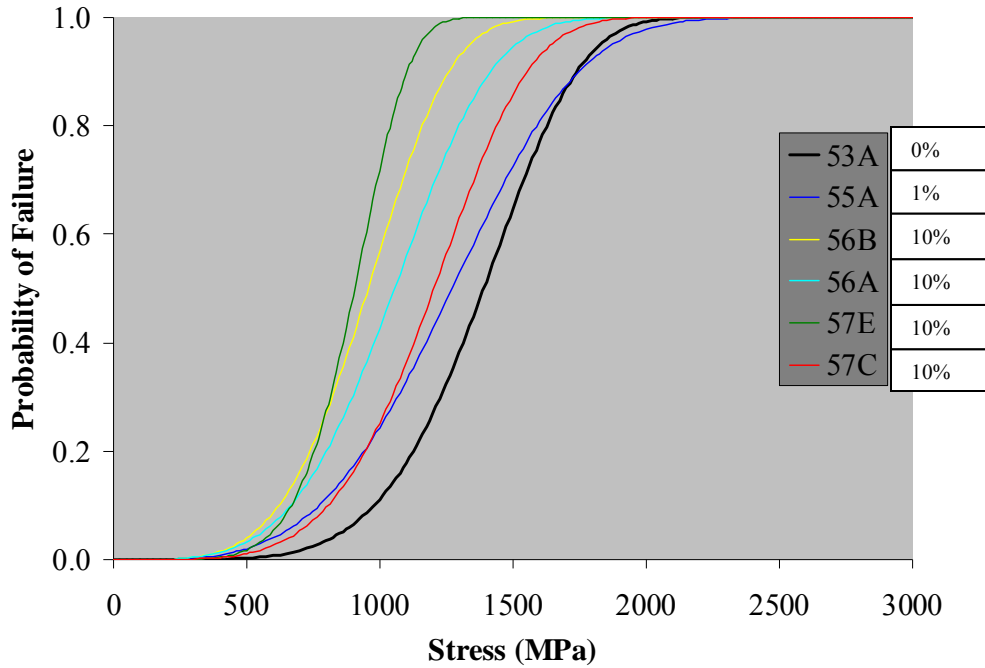the population of larger defect size. As the MWNT composite carbon fiber curves are shifted in this manner, it is consistent with larger defects in the fiber resulting in lower break stresses. Here, the sockets previously mentioned are likely functioning as larger defect sizes compared to the neat carbon fibers.

For 57C, the processing and composition of the fibers were exactly like 57E (initially 10wt% MWNTs processed from the dispersion supernatant), however it was initially tensioned to @MPa prior to carbonization as opposed to @MPa (Figure 2-7). This initial tension apparently improves the tensile strength in MWNT composite carbon fiber. Nevertheless, 57C also displayed the characteristically low modulus compared to neat carbon fiber. It therefore stands to reason that if higher tension improves the overall alignment with fiber axis, it can have a profound effect on the resulting fiber properties. Small imperfections in MWNT alignment can have severe implications on the resulting geometry of the socket-like defects. Sockets skewed at angles to the fiber axis would serve to concentrate stress more readily than those aligned with the fiber axis.

Effect on Strain

Fixing strain gauges to single filaments during tensile testing is impossible. This was accounted for to correct the modulus of the fibers by measuring the system compliance (Appendix C). Here, macroscopically, the single filament test is essentially two springs in series. One is the fiber, and the other is the load cell. Because the overall displacement measured during testing represents the total displacement in both the fiber and the load cell, coupled with the fact that each displacement is quite small and similar in magnitude, the displacement in the load cell can be a significant fraction of the overall measured displacement (strain). To account for these displacements, fibers from each tow were measured at 20, 30, 40, and 50mm gauge length. The inverse of the overall measured spring constant was then plotted and extrapolated to zero gauge length. Its intercept with the y-axis then quantified the degree of load-cell displacement with load for a given fiber tow of constant modulus and cross-sectional area, and was used to deconvolute the actual displacement of the fiber during testing. Because this was done to correct the modulus, an accurate measurement of fiber strain is then simply the ratio of the break stress to the corrected modulus. A graph of the fiber break strain is given in Figure 2-15.
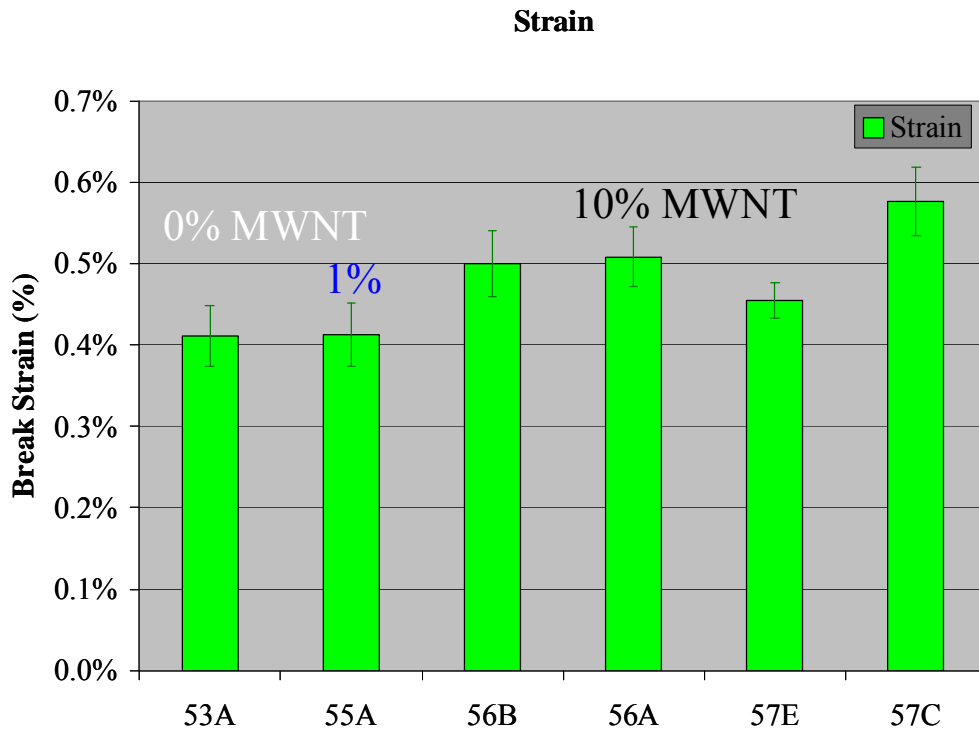
Figure 2-15 Break strain of MWNT composite carbon fiber
The error bars show the 95% confidence interval in the data.

Despite the fact that significant reductions in modulus and tensile strength were observed for concentrated MWNT composite carbon fibers, a clear increase in their break strain was anomalously observed the only exception being 57E, which may be explained by its slightly lower carbon yield (Table 2.1). The tendency to higher break strain in

conventional carbon/carbon composites is often attributed to a blunting of an advancing crack tip at the fiber matrix inteface[175]. Here similar mechanisms are likely to be occurring along with crack bridging as observed in Figure 2-6(c).

An integration of the stress-strain curves is directly related to the toughness of the fibers as is quantifies the amount of strain energy, or stored spring energy, the fiber can handle before failure. Since these fibers were completely linearly elastic, the area under the stress-strain curve was simply calculated ½ (break stress)(break strain) = ½ (Modulus)(break strain)^2. This product is often referred to as the strain energy density as is quantifies the strain energy stored in the volume of the gauge length of the fiber during tensile testing. A graph of the fiber strain energy density is given in Figure 2-16.

Strain Energy Density
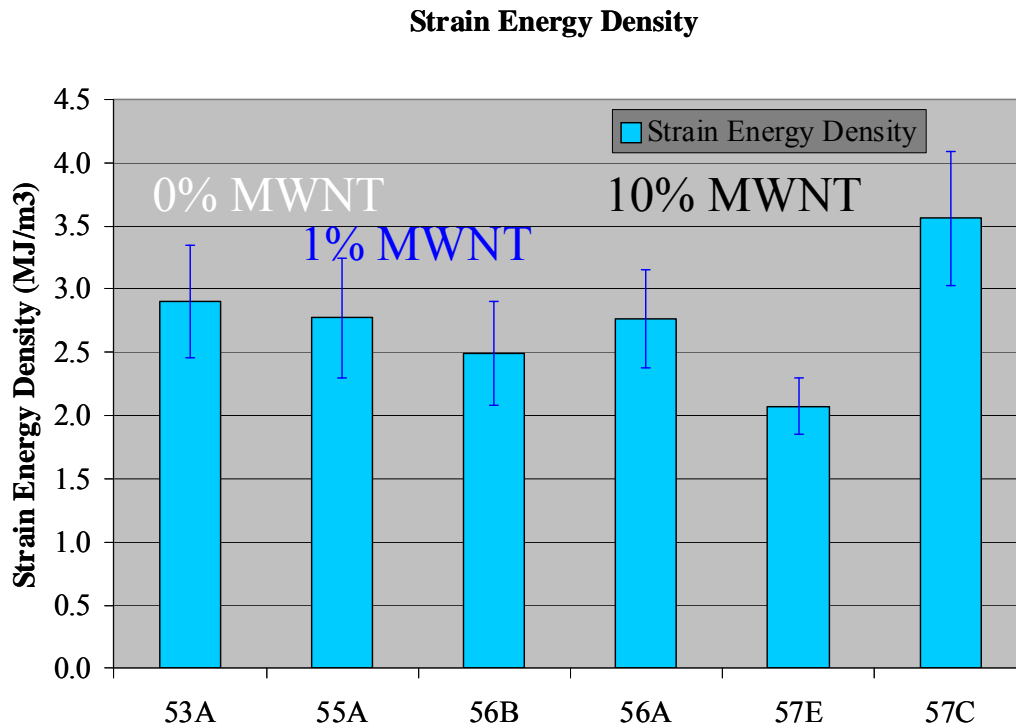
Figure 2-16 Strain energy density of MWNT composite carbon fiber
The error bars show the 95% confidence interval in the data.

Here, the strain energy density (toughness) of the fibers is essentially constant except for 57E, which again is likely due to its lower carbon yield. 57C, however, demonstrated a clear increase in strain energy density. The remarkable fact is that it outperformed the control neat carbon fiber despite the fact that its modulus was 207GPa, which is 40% lower than the control fiber modulus. Its ability to withstand greater break strain clearly enabled this increase to occur (0.577% break strain versus the control fiber at 0.411% break strain). The effect of the embedded MWNTs to mitigate crack propagation along with higher carbonization tensions are likely the underlying reasons for the increase.

Undoubtedly, the concentrated MWNT composite carbon fibers were significantly different from the neat carbon fibers, both in properties and morphology. Decreases in modulus suggested poor interfacial bonding, which was corroborated by SEM

observation pulled out MWNTs. In addition, interphase sheaths of carbon surrounding the MWNTs observed in the fracture surfaces indicated that the debonding was readily occurring at the interface between the bulk matrix and the sheathed MWNTs. This new effective MWNT, composed of the original MWNT plus its sheath, may be forming a completely new constituent within the fibers. One that, although likely to be itself of high modulus, easily debonds at the interface with the surrounding carbon matrix offering the parent carbon fiber no effective resistance to deformation, and thus a lower modulus is observed. Similarly to conventional carbon/carbon composites, the debonding or decoupling of the interphase+MWNT from the surrounding bulk carbon matrix may be due to heat treatment beyond that necessary to convert the PAN matrix to carbon causing the interphase to form a more graphitic carbon, thus a more dense carbon, which would promote separation from the bulk due to an increased localized volume contraction. This may explain the formation of sockets in the MWNT composite carbon fibers studied. Furthermore, these sockets are likely functioning as larger flaws, reducing the tensile strength as indicated by the Weibull analysis. However, upon initiation of micro-cracks, the MWNTs may function to deflect crack propagation at their boundaries, blunt the crack tip, and to bridge cracks to some degree, which explains increases in break strain. Although the measured tensile properties of the MWNT composite fibers were predominantly lower than the neat fibers, evidence pointed to the fact that the MWNTs, or the interphase+MWNTs, were not effectively being utilized. One area of intense interest which has risen from this analysis, is to investigate the effect of final heat treatment of the tensile properties of the MWNT composite PAN-based carbon fiber. If the carbonization temperature is excessively high (in this case @°C), causing decoupling of the interphase+MWNT from the bulk matrix fiber, and lower carbonization temperatures enable reinforcing effects from the MWNTs, it may represent a novel way to produce high performance carbon fiber at lower-than-normal processing temperatures (@°C). This may significantly reduce the cost of high performance carbon fiber.

2.3.4 Fiber Processing Revisited: Linkages to Structure-Properties

Macro-void content, resulting from inefficient fiber coagulation, is one of the many complicating factors in the analysis of these composite fibers. These large voids have been shown to have a negative effect on all fiber tensile properties. Their effect, along with alignment considerations are pictorially shown in Figure 2-17. Micromechanical models will invariably predict increases in composite properties with increasing volume fraction of aligned fibers. However they rarely deal with the presence of defects. Large macro-voids are shown in Figure 2-18 where they have caused tensile failure. Future void analysis may include helium pycnometry for fiber density and/or x-ray scattering experiments, but in general, large entrapped voids are directly linked to residual, entrained solvent from the original solution spinning of the fiber. If skinning of the fiber occurs during coagulation, the potential makings of voids are set in motion. A computational modeling experiment has therefore been carried out to predict the concentration profile of solvent within the fiber during coagulation.
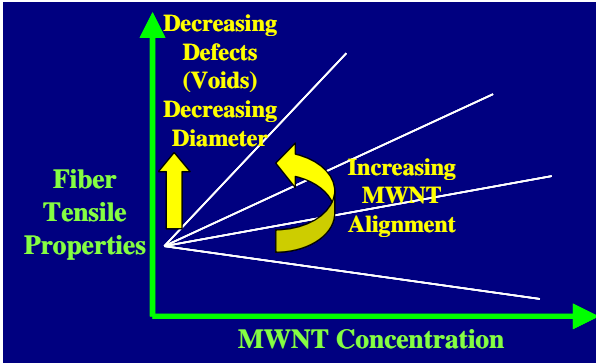
Figure 2-17 Effect of voids and MWNT alignment on tensile properties
The general effect of voids and relative MWNT alignment are shown as a function of MWNT concentration.
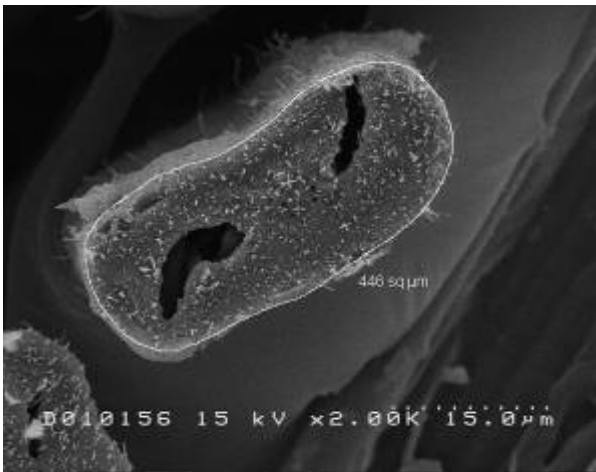

Figure 2-18 SEM image of macro-void in MWNT composite carbon fiber
SEM imaging of a MWNT composite PAN-based carbon fiber clearly shows typical voids as viewed, end-on within the cross section of the fiber.

2.3.4.1 Coagulation for Void Mitigation

The coagulation of PAN fibers during wet spinning is quite a complicated process, involving solvent diffusing out into the coagulant bath, and coagulant diffusing into the solidifying fiber. For this case, we simplified the problem to reflect free diffusion of DMAc out of a cylindrical PAN fiber.

$$\frac{C - C_0}{C_\infty - C_0} = 1 - \frac{2}{R}\sum_{n=1}^{\infty}\frac{\exp(-D\alpha_n^2 t)J_0(r\alpha_n)}{\alpha_n J_1(R\alpha_n)}$$

[2-2]

Equation [2-2] was used to model this diffusion process. C is the concentration of DMAc remaining in the PAN fiber in wt.% as a function of fiber radius, r, and time, t. R reflects the largest possible value of r at the fiber surface. Initially C_0 is the concentration of DMAc in the fiber. At t_0, C_0 is 0.8 independent of r. C_∞ is the concentration, in wt.%, of DMAc in the coagulation bath; the remaining being water. D is the diffusion coefficient of DMAc in PAN. As an approximation, D was taken to be 1.75 x 10^{-11} m^2/s, which is

46

the reported value for dimethylformamide (DMF) in PAN[177]. The product of $R\alpha_n$ are roots to the zero order Bessel function thus defining the value of α_n. The first five roots were used in the summation for each point; varying r while holding t constant; then varying t while holding r constant. The concentration profile of DMAc in the fiber was then graphically generated by plotting the value of C at the possible combinations of r and t.

Figure 2-19 shows in (0) the initial constant concentration of the spin dope at 80wt.% DMAc. Graph (A) shows the resulting concentration profile when the dope is coagulated in 10%DMAc/water solution for 45 s. In a practical sense, interest was in mitigating large gradients of solvent that would promote a thick skin formation on the fiber surface while the fiber interior remained a gel. These gradients would then set events up for difficult solvent diffusion from the center of the fiber through the skin, slowing solvent diffusion from the fiber and ultimately void fraction. The ideal concentration profile would remain flat (minimal gradient) across the diameter of the fiber as it decreases from 80% to 0%. A second, iterative method of the same model was then computed and plotted as a sequence in graphs (0) – (6). They represent the following coagulation scheme. An initially 80wt.% DMAc fiber is extruded and coagulated in a 50wt.% DMAc/water bath for 12 s (graph (1)). The complete concentration profile of the emerging fiber is then input into the model as the initial condition for the following coagulation in a 40wt.% DMAc/water bath for 6 s (graph (2)). This scheme of using the concentration profile of the exiting fiber from one coagulation bath as the input condition for another was continued through an additional 12 s under 30wt.% DMAc/water (graph (3)); 6 s under 20wt.% DMAc/water (graph (4)); 6 s under 10wt.% DMAc/water (graph (5)); and 12 s under pure water (graph (6)). A total of 54 s of decreasing solvent concentration coagulation was computed and compared to the original 45 s of coagulation under a constant 10wt.% DMAc/water bath. The primary difference is the successful mitigation of large concentration gradients of DMAc within the coagulating fiber. Fundamentally, the surface concentration is never allowed to diverge significantly from the centerline concentration. A more condensed graphical version of Figure 2-19 is shown in Figure 2-20, which clearly demonstrates the gentler, homogeneous diffusion of solvent out of the fiber. It is anticipated that the implementation of such a coagulation scheme will serve to minimize residual solvent entrainment, and ultimately minimize the void content.
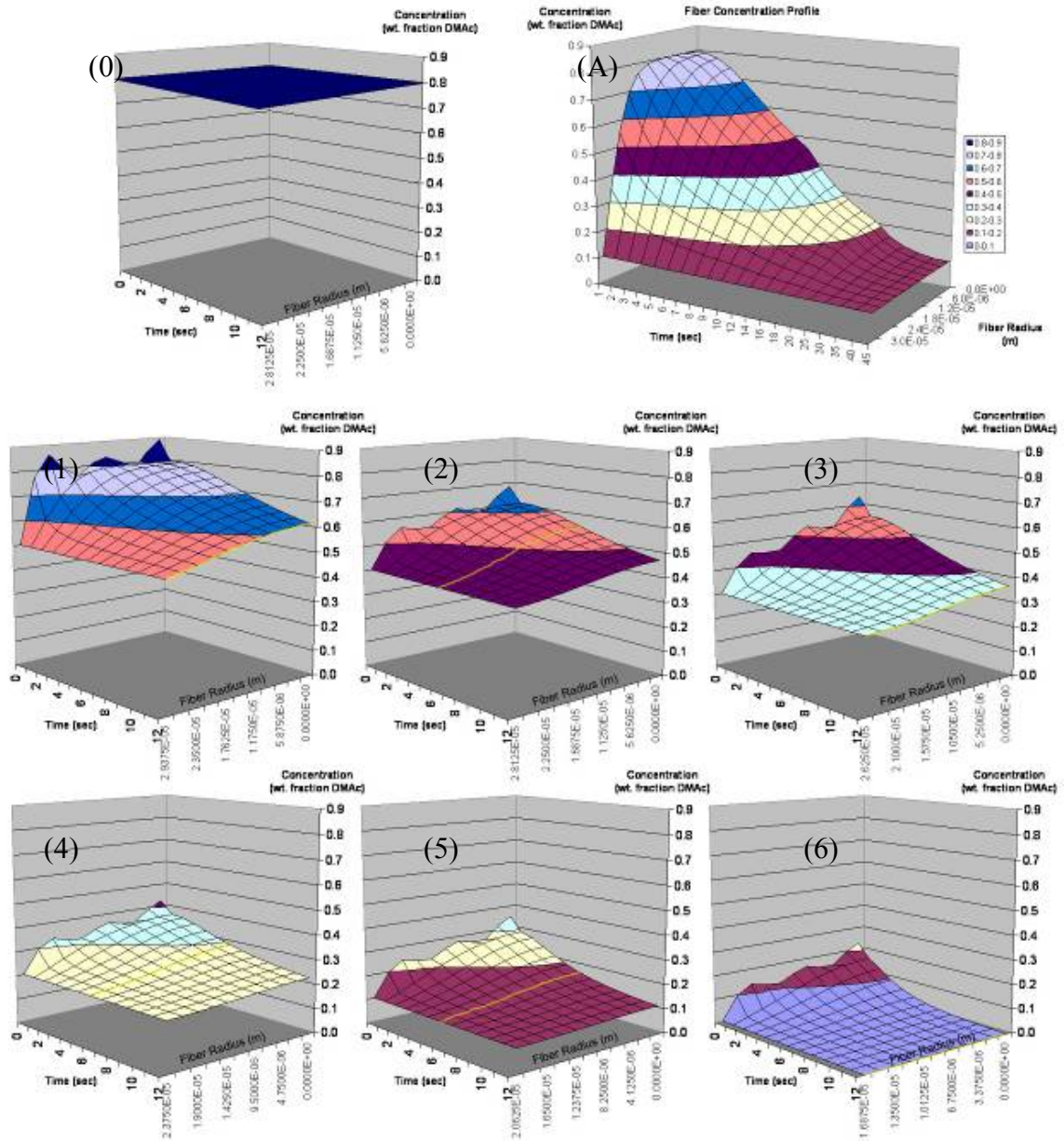
Figure 2-19 Coagulation modeling
Shown above are the results of the diffusion modeling during two coagulation processes. In both cases the initial PAN fiber exits the die as a homogeneous solution concentration of 80wt.% DMAc and 20wt.% PAN with a circular cross-section of radius 30μm, graph (0). In all graphs, the concentration of DMAc within the fiber is then modeled as a function of submersion time and fiber radius. First, graph (A) shows the concentration profile of the PAN fiber when coagulated in a bath of constant 10wt% DMAc and 90wt.% water for 45 seconds. Second, graphs (1) – (6) show the concentration profile of the PAN fiber when sequentially coagulated in the following manner: final concentration profile out of bath 1 = initial concentration profile into bath 2, and so on as indicated by the yellow highlighted profile line. Each graph represents a coagulation bath. The concentration of DMAc/water in the baths, and time in the baths are sequentially [graphs (1) – (6) respectively]: 50% (12 s), 40% (6 s), 30% (12 s), 20% (6 s), 10% (6 s), and 0% (12 s). The second coagulation process represents a smoother, more homogeneous transition from spin-dope protofiber to a fully coagulated, solid fiber.
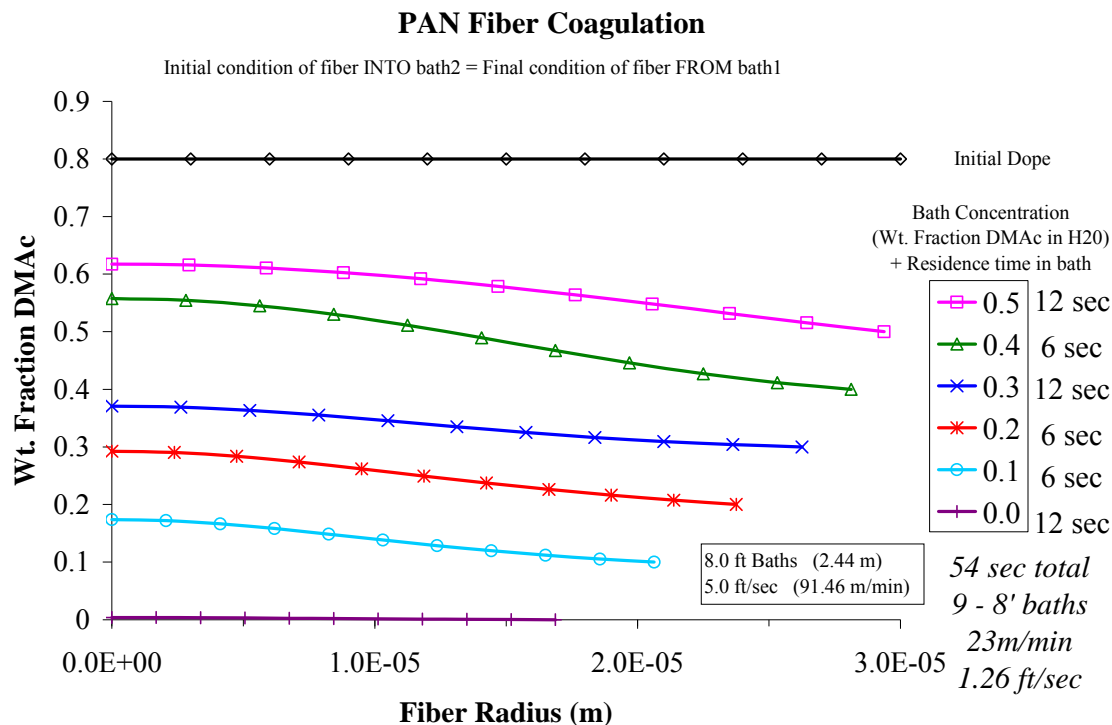
PAN Fiber Coagulation

Initial condition of fiber INTO bath2 = Final condition of fiber FROM bath1

Figure 2-20 Concentration profile
Shown above is a condensed version of Figure 2-19, where transient effects are not shown. The DMAc concentration profiles through the fiber are plotted upon exit from their respective coagulation bath for the indicated submersion time. A nearly linear decrease in the DMAc concentration within the fiber is indicated with time. This minimizes the potential for thick skin formation, which can trap residual solvent and ultimately lead to voids within the fibers.

2.4 Conclusions

In this chapter, fibers were successfully solution spun from polyacrylonitrile (PAN) spinning dopes containing homogeneously dispersed multiwall carbon nanotubes (MWNTs), and converted into composite carbon fibers. Key fiber morphologies were observed using SEM including good MWNT alignment and homogeneity throughout the fiber cross section. SEM observations of fracture surfaces showed the formation of an interphase layer of carbon around embedded, protruding MWNTs along with evidence of stress graphitization at the boundary of MWNT pull out from the matrix carbon fiber. These indicated failure of the interface between this interphase and the bulk carbon matrix. Little evidence for MWNT telescoping was observed along with some evidence of MWNTs functioning to bridge cracks. The measured mechanical properties of the MWNT-containing composite carbon fibers were compared to neat carbon fibers. After correcting for system compliance, decreases in the moduli of MWNT composite carbon fibers suggested poor adhesion to the MWNTs. Increases in break strain, and strain energy density were observed for MWNT composite carbon fibers initially containing 10 wt.% MWNTs processed from the dispersion supernatant, and initially tensioned to

@MPa. SEM micrographs indicated that the MWNTs served to bridge crack propagation.

These results indicate that efforts to improve interfacial bonding would likely enable improvements in the fiber modulus. Furthermore the function of MWNTs in carbon fiber to increase the break strain is significant. High strength carbon fiber is predominantly achieved by producing fiber inherently capable of withstanding high tensile strain (up to 2.5%). It is never the highest modulus carbon fiber available as high modulus fiber is very brittle and difficult to handle. The details of commercial high strength carbon fiber production is, by any measure, a well-guarded secret of a few large industrial carbon fiber producers, and has been vaguely linked to variations in the precursor chemistry, dope cleanliness, carbonization tension, carbonization temperature, etc. MWNT composite carbon fiber may offer a novel route to producing higher break strain fiber.

Lastly it is significant that templating of carbon to the embedded MWNTs occurred. It is not yet known if this growth of carbon represents true epitaxial crystal growth. Although these structures appear to have readily debonded from the matrix carbon fiber, they are likely high modulus, high strength micro-fibrils of carbon. Further research will undoubtedly focus on improving their bonding to the bulk matrix. Controlling this templated carbon organized with different structure than the bulk matrix at MWNT surfaces embedded in PAN-based carbon fiber, and fostering adhesion is likely to be key for further development of the properties of the resulting composite carbon fibers.

3.1 Introduction

High performance materials are typically thought of as those that exhibit elevated quasi-static mechanical properties, like the high strength and high modulus of carbon fiber. However, performance in real world applications is largely based on the material's ability to withstand fatigue failure. Results from the previous chapter suggest that MWNTs were increasing the break strain of composite carbon fibers by serving as crack propagation inhibitors. This result, along with other reports, indicate that MWNTs may be very effective in increasing the fatigue performance in composites*[142, 143]*.

In this chapter, the fatigue performance of a commodity thermoplastic matrix, polymethylmethacrylate (PMMA), filled with MWNTs, and with chopped carbon fibers (CCF), is measured and compared. It is hypothesized that the nanoscale dimensions of the MWNTs enables them to directly interact with the matrix at the sub-micron scale, where damage such as crazing begins, which leads to a critical crack (flaw) that ultimately causes failure. Crazes form when the molecules of the polymer realign in the direction of the applied stress*[178]*. This not only creates fibrils of aligned polymer but it also generates regions of micro-cracking. Typically, the dimensions of the fibrils and micro-cracks are larger than MWNTs but much smaller than carbon fibers; therefore, the MWNTs are more likely to affect craze formation and growth. Since crazing often precedes fatigue crack growth, MWNTs should exhibit a greater effect on fatigue performance than would carbon fiber.

3.2 Experimental

3.2.1 Instrumentation

The fatigue test is fundamentally encompassed by counting the number of deformation cycles required to cause the material to fail. The deformation cycles to failure are usually a function of magnitude of the applied stress or strain (held constant during the test). A collection of fatigue tests is often reported by the S-N curve, or stress amplitude versus number of cycles to failure. Increasing stress amplitude drastically decreases the number of cycles required for fatigue failure. In practice, stress-controlled testing, by a transducer feedback control loop, is usually limited to one specimen at a time and is very time-consuming. Specimen to specimen variation can lead to large standard deviations for the test, increasing the number of specimens needed to establish average values. A key objective of this study was to establish the fundamental principles and mechanisms governing the fatigue failure for carbon-based fillers (MWNT, and CCF) on the fatigue life rather than the specific effects of deformation amplitude on fatigue life. An in-house fatigue tester was designed and built in order to test numerous specimens at one time.

The simplest way to build multi-specimen fatigue test systems was to control the amplitude of strain rather than stress. The resulting instrument, built in-house, also enabled simultaneous testing at varying strain amplitudes. Figure 3-1 represents how the instrument worked. Rectangular beam specimens, held in place at one end (single

cantilever mode), are bent upwards by the rotation of a circular cam offset from the axis of rotation. The amount of offset defined the amplitude of the bending deflection, and the specimen holder height was adjusted for each cam offset such that no deflection occurred at the cam minimum. As the cam rotated, the specimen was deflected from zero, upwards to a maxima, then back to zero repeatedly. Twelve cams, identically machined to generate a desired deflection, were positioned on a single axle driven by a belt linked to a motor at one end. Twelve specimen holders, positioned at the desired height were installed to line up the specimens with the cams. By daisy-chaining the drive belt from one axle to another with pulleys, 4 rows, each of 12 specimen holders – cams, were installed. This enabled each row of 12 specimens to be simultaneously tested at varying amplitude of deflection. The drive motor was then wired with an AC frequency controller, which allowed the desired rate of the fatigue deflection to be obtained. A view of the completed instrument is shown in Figure 3-2.
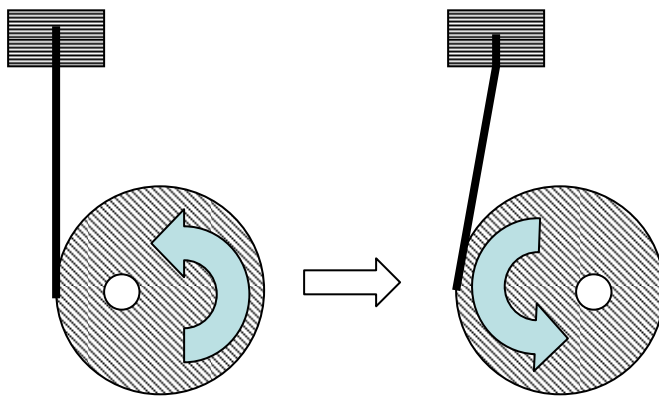

Figure 3-1 Basis of the fatigue testing instrument

To count the number of bending cycles to failure, a simple detection system was designed and installed. Small beam-break detectors, like those used in inkjet printers to position the printhead, consisting of U-shape with an emitter side and a detector side were installed at each specimen holder. The detectors were fixed such that they straddled each specimen from the side. During testing each specimen blocked its own beam until failure, which resulted in the broken end of the specimen to fall, and the beam then passed to the detector for that specimen. Circuitry[*] was designed that counted the cycles imparted during the fatigue test by using a master counter, consisting of a flag mounted to the shaft which repeatedly broke the beam of the master detector with each cycle. This signal was then counted as 1 cycle for all of the specimens for which their respective detector did not detect their own beam (due to the specimen blocking it). Since failure in single cantilever bending occurs at or near the specimen holder, as each specimen failed it simply fell to the floor. This enabled the detector to then detect their beams, and therefore specimen failure. When this occurred, the counter stopped for that particular specimen. The test was continued until all the specimens failed or a particular number of cycles were set as the run-out.

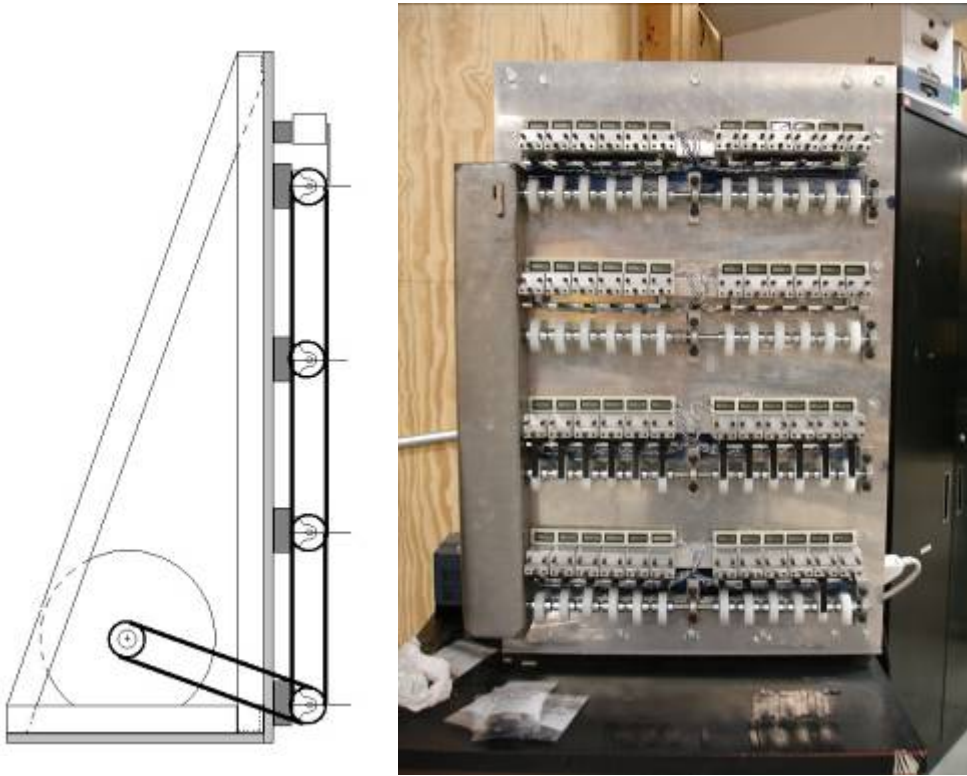[*] Circuitry was designed by Paul Shaffer at University of KY CAER

52

Figure 3-2 Photograph of the fatigue testing instrument

3.2.2 Sample Production

Multiwall carbon nanotubes (MWNTs) were produced in our laboratory to high purity (>95%) using a chemical vapor deposition process[14]. Histograms of their lengths post processing (Appendix A) indicated that the average MWNT embedded length was 9 μm. Combinded with an average outer diameter of 25nm gave an average MWNT aspect ratio of approximately 350. High strength PAN-based carbon fiber produced in a 12K tow (average fiber diameter = 5 micron) by Graphil Inc. was chopped in a water slurry using a blender to an average length of approximately 300μm. This gave the fiber an aspect ratio of approximately 60. A commercial grade PMMA, in pellet form was melt mixed with the two fillers to produced composites at 0.1, 0.5, 1.0, and 5.0 vol.% in the PMMA (ρ_{MWNT} = 2.00g/cc and ρ_{PMMA} = 1.17g/cc). Similarly processed neat PMMA was used as the control. The melt mixing process, described by Marrs[179], employed counter rotating mixing rotors in a 300ml high shear mixing apparatus built by Haake at 220°C. After mixing, the material was removed and allowed to cool in ambient conditions (25°; air). Once the material hardened, it was crushed into pellets (<5mm) and, subsequently, hot-pressed (200°C) under vacuum into films of uniform thickness. The films were machined into rectangular specimens (60mm x 10mm x 1.7mm) suitable for the constant amplitude-of-deflection fatigue testing. The rough surfaces of each specimen were smoothed with a rotary polishing device and all specimens were annealed (120°C) for approximately 20 hours. This relaxed residual stresses that developed during the machining process of specimen preparation. The specimens were aged in air (25°C) for an additional 20 hours prior to testing.
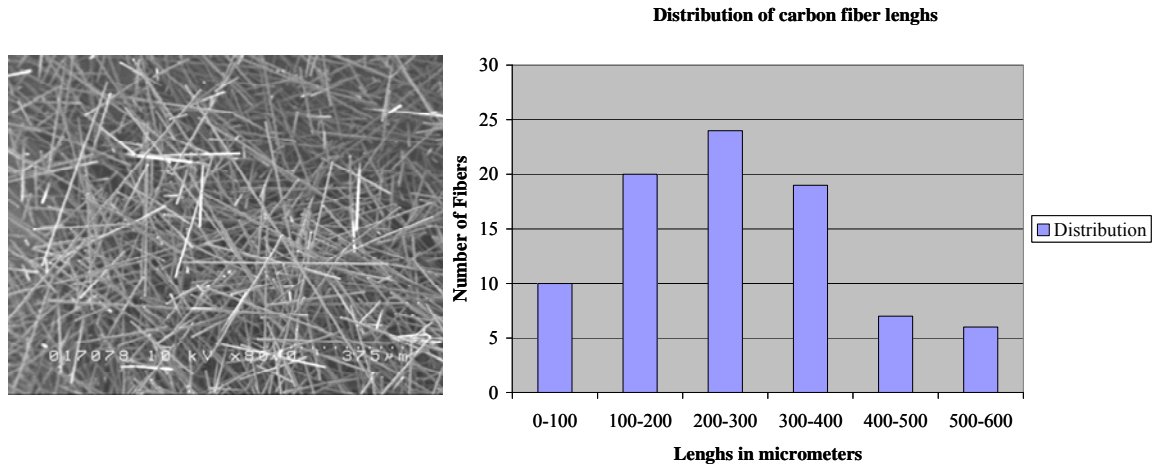
Figure 3-3 Chopped carbon fiber length distribution
Chopped carbon fiber

3.2.3 Fatigue Testing

Each sample (N = 12) was tested to failure in the custom built, constant amplitude-of-deflection fatigue tester. The specimens of each sample were tested simultaneously with amplitudes of 0.5" (12.7mm) and 0.4375" (11.1mm) at a test frequency of 5 Hz. Higher frequencies can promote heat build-up and temperature-induced sample softening. The run-out value was 5,000,000 cycles. The numbers of cycles to failure were recorded and analyzed using the linear version of the 3-parameter Weibull model (equation 3-3)*[143]*. To begin the analysis, the probability of failure is first calculated by ranking each specimen in number of cycles to failure in ascending order (R = 1, 2,…N), and implementing equation 3-1.

$$P(N_f) = \frac{R - 0.3}{N + 0.4} \qquad [3\text{-}1]$$

The minimum fatigue life (N_o), quantifies the number of cycles below which failure has zero probability and is calculated using the method of Janna*[180]* restricting $N_0 \geq 0$. Subsequently, the left side of equation 3-3 is plotted versus the $\ln(N_f\text{-}N_0)$, and a linear fit is used to extract the two remaining parameters: the shape parameter (α) also known as the Weibull modulus indicative of sample variance, and the location parameter (β) which characterizes the number of cycles below which 63.2% of the specimens fail *[180]*.

$$P(N_f) = 1 - \exp\left[-\left(\frac{N_f - N_0}{\beta - N_0} \right)^{\alpha} \right] \qquad [3\text{-}2]$$

$$\ln\left[\ln\left[\frac{1}{1 - P(N_f)} \right] \right] = \alpha \ln(N_f - N_0) - \alpha \ln(\beta - N_0) \qquad [3\text{-}3]$$

To simplify the comparisons between each material, the three Weibull parameters were used to calculate the Weibull mean (N_{WM}) using equation 3-4, which is an accepted

single number indicator of fatigue performance, which accounts for all of the above statistical considerations[143].

$$N_{WM} = N_0 + (\beta - N_0)\Gamma\left(1 + \frac{1}{\alpha}\right) \qquad \text{[3-4]}$$

Finally, the fractured surfaces of randomly selected failed specimens were investigated with scanning electron microscopy to investigate the effect of dispersed MWNTs and CCFs on fatigue fracture.

3.3 Results and Discussion

The average cycles to failure for each of the MWNT and CCF loadings are shown in Figure 3-4 for both the 11.1mm (7/16") and 12.7mm (1/2") deflections. The error bars are indicative of the 95% confidence limit. Weibull analysis are generally preferred due to the fact that the distribution of fatigue failure is non-normal. The Weibull means were calculated to compare the fatigue performance, and are shown in Figure 3-5. Significant improvement in the fatigue performance was observed. Low volume fractions of MWNTs were shown to improve the fatigue performance at both deflections, which became most apparent at 1.0vol% of filler. At this concentration, the enhancement effect is most clearly visible at the lower amplitude of deflection. Here, the MWNTs clearly outperformed the CCF, +623% vs 244% by Weibull mean comparison (+488% vs +268% by arithmetic mean comparison).

At 5.0vol% filler, the fatigue performance of the MWNT-filled PMMA began to decline, and is attributed to inhomogeneous dispersion resulting in agglomerates of MWNTs which can catalyze fatigue failure be serving a crack initiation sites (as shown in Figure 3-10). The 5.0 vol% CCF, however, began to outperform similarly loaded MWNTs which is likely due to their ability to be more homogeneously dispersed; a result from their being less likely to become entangled with each other. The Weibull parameters and Weibull means for each material and deflection are presented in Tables 3.1 and 3.2.

A general saturation of the enhancement of the fatigue properties for MWNT-filled composites occurred at 1.0 vol% filler. The effect of MWNT reinforcement was more pronounced at the smaller deflection. These results are similar to those reported by Marrs for MWNT reinforced methyl methacrylate – styrene copolymer (i.e. as stress amplitude decreased, the effect of MWNTs increased)[143]. Furthermore, in that report a saturation of the enhancement effect of the MWNTs occurred at approximately 2.0 wt%, which for PMMA/MWNT (density ratio of approximately 2:1) translates to 1.0 vol%. The key finding here is that similarly substantial increases in the fatigue performance of a commodity amorphous polymer, PMMA, can be realized by simple incorporation small volume fractions of MWNTs into them via melt mixing.
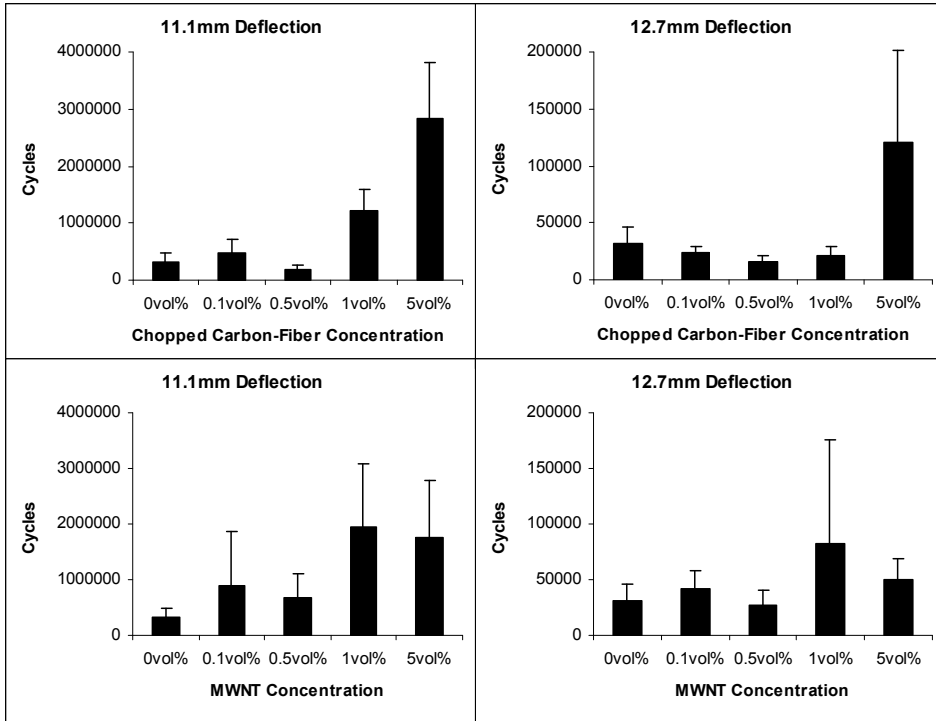
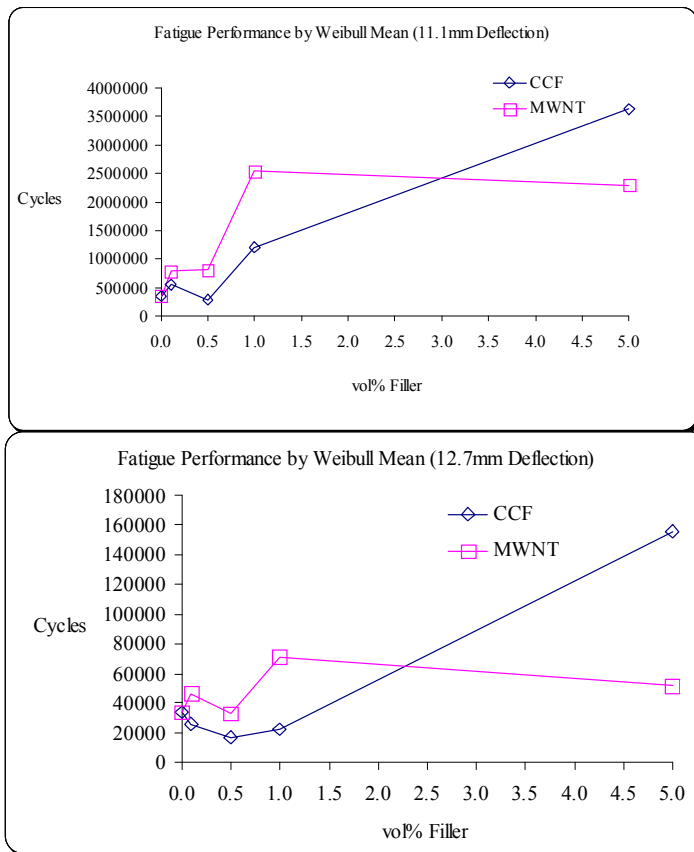**Figure 3-4 Cycles to failure of MWNT and CB – PMMA composites**

Figure 3-5 Fatigue performance of MWNT and CB – PMMA composites

Table 3.1 Weibull Parameters and Weibull Means at 11.1mm Deflection

Chopped CF - 11.1 mm Deflection

Group	N_O	α	B	N_{WM}
0vol%	42733	0.950	344714	351735
0.1vol%	91689	0.733	473909	555673
0.5vol%	0	0.700	229208	290215
1vol%	0	1.216	1291131	1210352
5vol%	0	0.914	3477496	3628978

MWNT - 11.1 mm Deflection

Group	N_O	α	β	N_{WM}
0vol%	42733	0.950	344714	351735
0.1vol%	38013	0.669	607913	793300
0.5vol%	0	0.725	651751	799006
1vol%	187232	0.587	1708560	2543920
5vol%	61683	0.623	1623311	2303739

Table 3.2 Weibull Parameters and Weibull Means at 12.7mm Deflection

Chopped CF - 12.7 mm Deflection

Group	N_O	α	β	N_{WM}
0vol%	9795	0.756	30021	33718
0.1vol%	0	2.866	28988	25836
0.5vol%	4582	1.683	18202	16743
1vol%	4100	1.279	23766	22324
5vol%	23344	0.563	104006	156016

MWNT - 12.7 mm Deflection

Group	N_O	α	β	N_{WM}
0vol%	9795	0.756	30021	33718
0.1vol%	6529	0.944	45382	46405
0.5vol%	0	1.145	34538	32913
1vol%	6727	0.813	64646	71610
5vol%	13445	1.089	52627	51384

Using the Weibull parameters shown in Tables 3.1 and 3.2, full probability of failure curves were generated (as shown in Figure 3-6), which can be analyzed to determine the effect of all fillers relative to the neat PMMA as the number of cycles increases. For specimens cycled at the lower amplitude of deflection (11.1mm), every loading of each filler was effective for decreasing the probability of fatigue failure at a given number of cycles, except 0.5vol% CCF. Most notably, PMMA filled with only 1.0 vol% MWNTs, significantly decreased the probability of fatigue failure, and was just as effective as both 5.0 vol% MWNTs and 5.0 vol% CCF. At the higher amplitude of deflection (12.7mm) only 1.0 vol% MWNTs, and 5.0 vol% CCF remained effective for decreasing the probability of fatigue failure, with CCF performing better than MWNTs. Overall, the improvement that 1.0 vol% MWNTs made to the fatigue performance of a PMMA matrix, compared to similar loadings of conventional CCFs and at varying amplitude of deflection, was impressive.

3-Parameter Weibull Model, Filled-PMMA, 11.1mm Amplitude
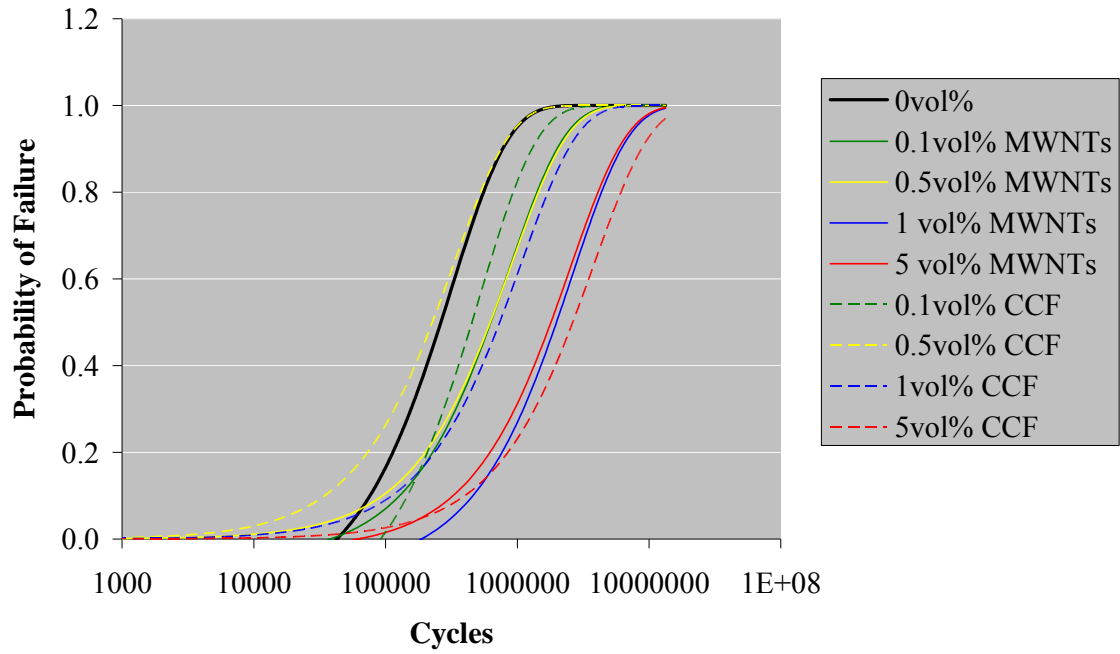
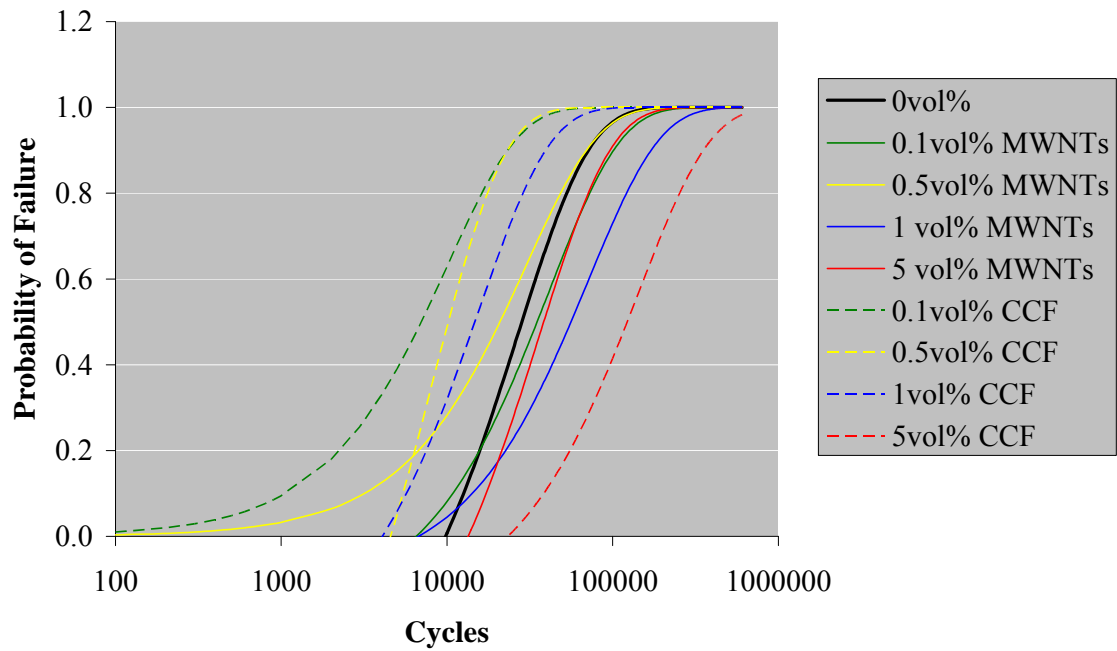**3-Parameter Weibull Model, Filled-PMMA, 12.7mm Amplitude**

Figure 3-6 Weibull probability of failure curves

Function of MWNTs for Fatigue Enhancement
In all cases, the fatigue fracture originated from the side of the specimen under tension during bending. In terms of fatigue, failure in tension is related to repetitive opening of micro-cracks causing them to advance through the specimen. Figure 3-7 shows SEM evidence of crack propagation failure. Below the white dotted lines in the figure denotes the region of tension during bending, and above the line, compression. It was repeatedly observed by SEM that the MWNT containing specimens showed clear crack propagation rings, which resulted in an annular "tree-ring" features left behind by the advancing crack. No such rings were observed in the compression side for either MWNT or CCF specimens.
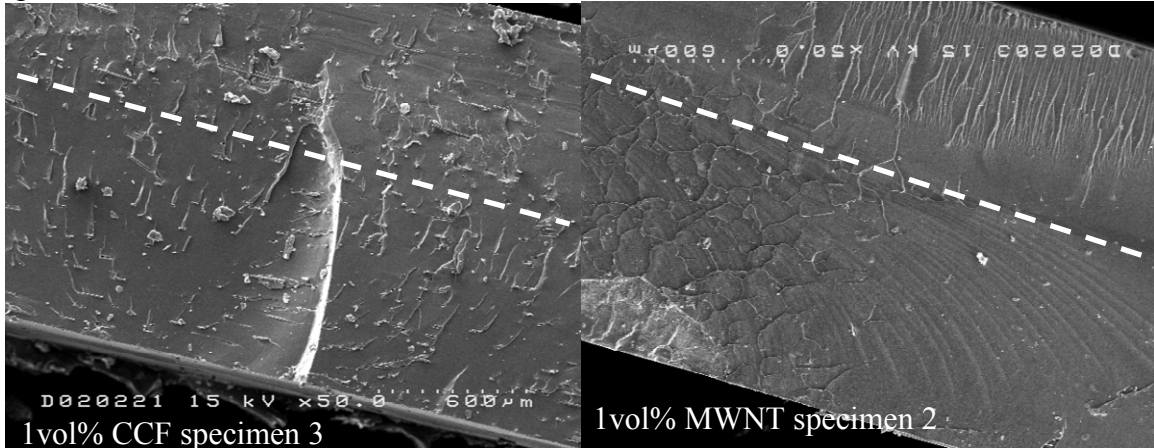
Figure 3-7 Fatigue fracture of PMMA composites: tension and compression surfaces

Figure 3-8 shows similar features to those in figure 3-7 however, the actual position of crack initiation can be inferred located at the lower left of Figure 3-8(a). Here, crack initiation has occurred at the surface of the tensile side of the specimen where tensile stress is the highest. A magnified view of the initiation site shown in Figure 3-8(b) shows how the crack growth rings trace back to the point of initiation, which appears to have been a surface void (white arrow). Since highly dense ring structures are indicative of slow crack propagation, the dense ring structures immediately surrounding the void suggest the MWNTs mitigated the rate of the subsequent crack growth*[178]*.

Figure 3-8 Initiation of fatigue failure

Fatigue failure occurs in a sequence of phases: (I) crack initiation, (II) accumulation of cyclic damage, crazing, and slow crack propagation, and (III) fast cata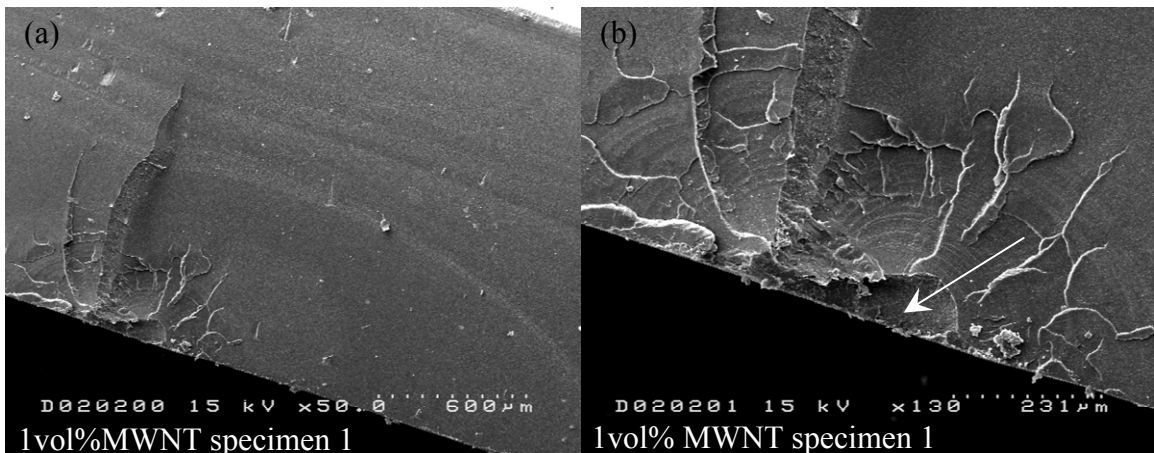strophic failure. Marrs showed that the primary mechanism of the fatigue performance enhancement for MWNT composite bone cement was due to the MWNTs functioning to significantly slow the effects occurring in phase (II)*[143]*. The small dimensions of the individual MWNTs were important in that they work at the sub-micron scale to mitigate damage prior to sufficient accumulation and coalescence to promote the onset of phase (III) fracture. Here, where MWNTs are directly compared with larger diameter CCFs, results corroborating this hypothesis are observed at low volume fraction filler. At 5.0 vol% filler, CCF began to outperform the MWNTs. This may be due to the effect of large-scale fiber debonding serving to dissipate strain energy that would otherwise contribute to crack propagation coupled with the large number of CCFs serving to deflect and blunt the propagating crack tip (as shown in Figure 3-9). Furthermore, inhomogeneous dispersion of MWNTs at 5.0 vol% was a common occurrence as shown by the MWNT agglomerations present in the fracture surface from which cracks can propagate (Figure 3-10). The underlying difference between the fatigue response of the MWNT and CCF filled PMMA is that the MWNTs served to mitigate crack growth by slowing craze coalescence prior to crack propagation. The CCFs, however, at high enough loadings can slow crack growth after craze coalescence has occurred by debonding and crack tip deflection.
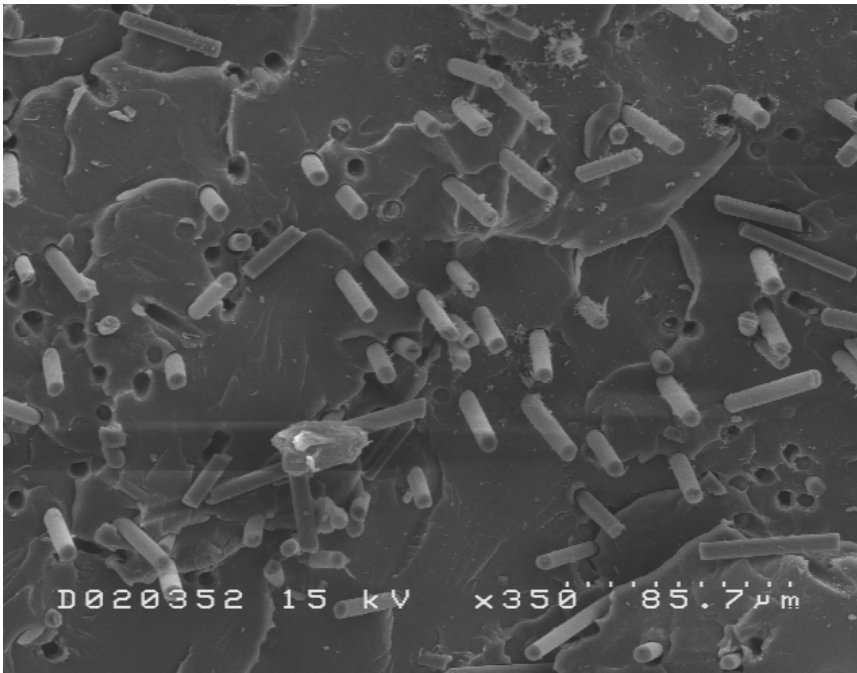

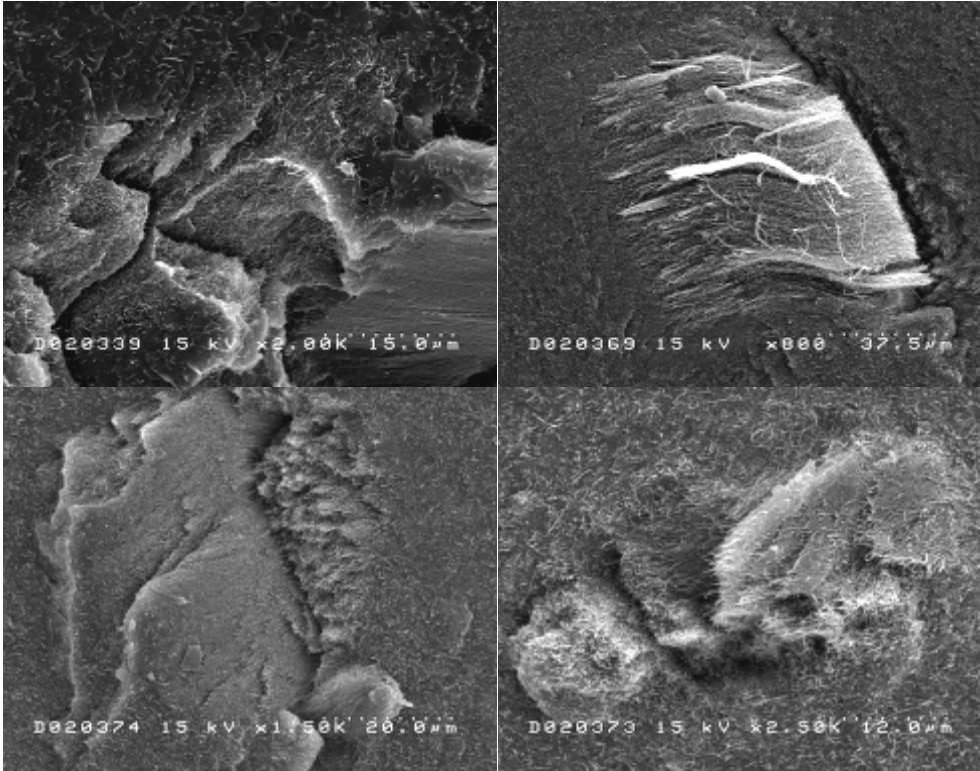**Figure 3-9 Fatigue fracture of 5.0 vol% CCF in PMMA**

Figure 3-10 Fatigue fracture of 5.0 vol% MWNT in PMMA (MWNT agglomerates)

Particularly, the small size of MWNTs enables them to reduce the sub-micron damage accumulation from crazing of PMMA. Regarding fatigue fracture, crazing dominates the phase (II) accumulation of damage. Crazing is a plastic deformation process of chain realignment in amorphous polymers under tensile load in which polymer chains draw into micro-fibrils parallel to the direction of load. As a number of these micro-fibrils extend, they begin to leave behind micro-cavities or recesses, from which additional polymer chains are drawn into the micro-fibrils. This process effectively toughens the polymer by enabling plastic deformation without rupture. However, as this process continues the cavities grow too large and the micro-fibrils being to fail. Crazing normally occurs just ahead of a progressing crack tip in a zone of plastic deformation. As the micro-fibrils fail, the crack tip quickly advances completely through the plastic zone, stops, and a new plastic zone of crazing begins. As this process continues, and the crack(s) grow larger, a point is reached where a single critical crack has grown large enough to concentrate the tensile (crack-opening) stress at its tip where fast brittle fracture of the PMMA occurs.

Conclusive TEM evidence has shown previously that nanotubes can effectively function to mitigate craze coalescence[181]. By doing so, they certainly are likely then to slow crack propagation, and enhance the fatigue performance of the PMMA matrix. Even after sufficient craze coalescence has occurred to allow the advancement of the crack tip through the plastic zone, remaining MWNTs may function to bridge the crack wake.

The micrograph in Figure 3-11 revealed the ability of a carbon nanotube to span a micro-crack that most likely developed during crazing of the PMMA matrix. This type of bridging helps to prevent micro-crack growth and slows the coalescence of multiple

micro-cracks. Since crazing typically precedes fatigue crack growth, the MWNTs slow the rate of crack growth by reinforcing the regions of crazing. This is not the case, however, for chopped carbon fiber. In fact, the diameter of a typical carbon fiber is too large to effectively address the development of a craze zone. In the suspected regions of crazing, traces of carbon fibers were present as shown in Figure 3-12 and 3-13, which suggests that during crazing the carbon fibers de-bonded from the matrix and offered little resistance to crack growth.

Figure 3-11 Craze bridging of MWNT
This micrograph represents the craze zone surrounding a secondary fatigue crack. The white arrow points to an isolated carbon nanotube bridging the faces of a micro-crack.
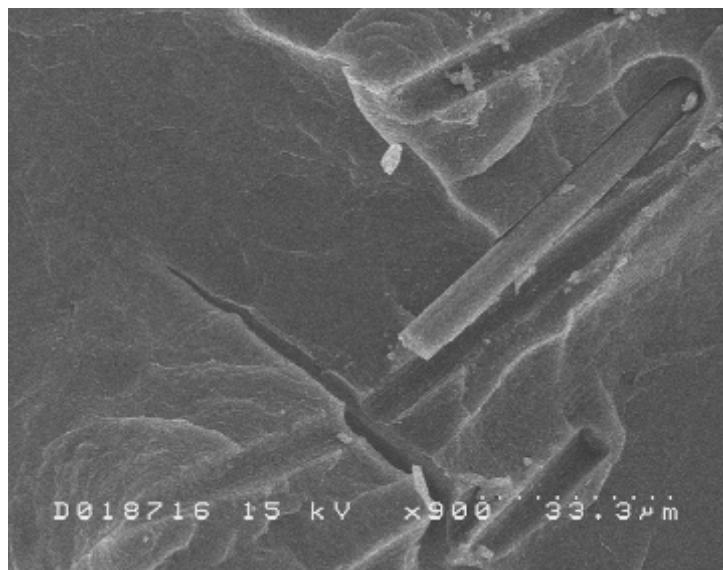

Figure 3-12 Debonding of carbon fiber
This micrograph of a 0.1vol% CFF – PMMA specimen reveals a carbon fiber that is de-bonding from the PMMA matrix. This also shows the impression of a carbon fiber that spans perpendicular to a secondary crack.
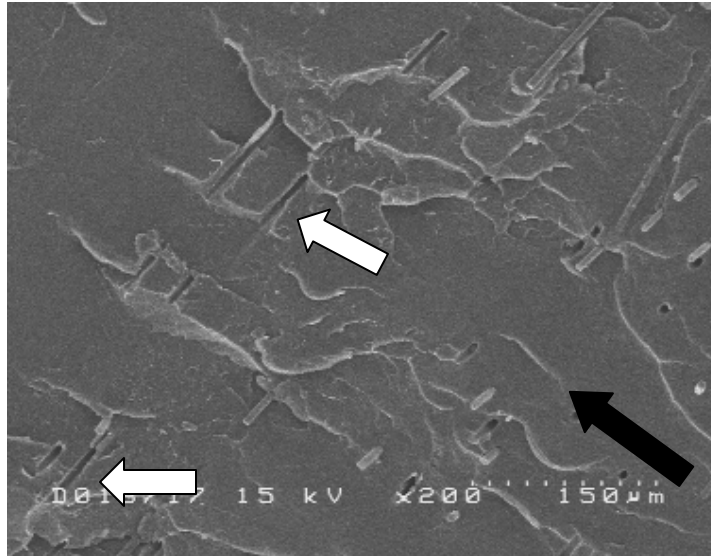
Figure 3-13 Debonded carbon fiber relative to crack growth
This SEM micrograph shows the fracture surface of a 0.1vol% CFF – PMMA specimen. The black arrow indicates the direction of crack growth. The white arrows point to traces of de-bonded carbon fibers within the "rough" region. This is a region of suspected crazing.

3.4 Conclusions

In this chapter the fatigue properties of filled PMMA were experimentally measured and analyzed. An in-house fatigue tested was designed, built, and used to carry out the fatigue testing, and proved successful to generate large amounts of fatigue data relatively quickly. The fillers used, MWNTs and chopped carbon fiber (CCF), were both effective to enhance the fatigue properties of the neat PMMA matrix. The MWNTs were superior to the CCF at all conditions tested up to a loading of 1.0 vol%, and significantly improved the fatigue performance of the PMMA. At the lower amplitude of deflection (11.1mm), 1.0 vol% MWNT enhanced the PMMA by 623%, whereas CCF enhanced it by only 244%. At the highest loading, 5.0vol%, the CCF outperformed the MWNTs. Nevertheless, these results are significant, and suggest that MWNTs may be very effective in mitigating failure in polymers subjected to cyclical or static (creep) loads. At higher amplitude of deflection (12.7mm) low loadings of CCF offered no benefit in the fatigue performance of CCF filled PMMA (perhaps a slight reduction), while MWNTs at 1.0 vol%, were still able to improve it by 112%. SEM imaging concluded that fatigue fracture was due to tensile crack opening during bending. Although CCF composites performed quite well at 5.0 vol%, they may be too large to effectively mitigate craze coalescence which leads to micro-cracking. Therefore their fatigue-enhancing effect was only observed at higher loading where sufficient crack tip blunting and fiber debonding can serve to dissipate energy and mitigate crack growth. At a loading of only 1.0 vol%, the MWNTs were very effective in enhancing the fatigue performance of the PMMA composite. Here the nano-scale dimensions of the MWNTs enabled them to mitigate sub-micron damage (crazing), which is likely the mechanism for the enhanced the fatigue performance.

4.1 Introduction

Due to their graphitic character, carbon nanotubes are good conductors of both electric current and thermal energy*[5, 30]*. Therefore, carbon nanotubes could act as conductive fillers in polymeric or insulating matrices. In a composite, the high aspect ratio of nanotubes is a key factor in that it enables the formation of a percolated, conductive network at lower concentration than that of spherical fillers such as carbon black (CB). In this chapter, the electrical and thermal conductivity of MWNT, and CB-filled, fully cured epoxy resin are investigated and compared at varying concentrations.

4.2 Experimental

Materials

The MWNTs were produced in our laboratory to high purity (>95%) using the chemical vapor deposition process, and used as-produced *[14]*. The carbon black, acquired through Alfa Aesar (Stk# 39724), had an average particle size of 42nm, and was also used as-provided. The epoxy resin, EPON 826, was cured with an anhydride hardener, nadic methyl anhydride (a generic version of HY906) combined with the catalyst EMI-24. The ratios of the three were 100:84:1 parts by weight respectively.

Dispersion Processing

The slow room temperature curing kinetics of the epoxy system enabled all 3 components to be combined (185g total), the desired filler added, and all mixed together using a high shear laboratory mixer (Silverson L4RT) at 5000 rpm for 15 minutes. The cups in which the dispersions were processed were continuously moved by hand to ensure that all of the material passed through the mixer head. Dispersions were processed with 0.1, 0.5, 1.0, 2.0 and 5.0 vol% of MWNT and CB. Similarly a neat epoxy sample was processed as a control. MWNT-epoxy dispersions (pre-cured) had much higher viscosities than those containing carbon black, and become nearly impossible to process at 5vol%. For conversion of the concentration to volume fraction, the density of the MWNTs and carbon black was assumed to be 2.0 g/cm^3 and the epoxy 1.2 g/cm^3.

Specimen Preparation

After mixing, the dispersion was poured (low viscosity) or transferred using a spatula to a disposable aluminum mold and cured by heating in air 0.5°C/min to 50°C for 6hrs followed by a post cure at 1°C/min to 180°C for 3hrs. Specimens 60 x 10 x 5mm were then cut from the center of the mould using a band saw, and the surfaces of the epoxy were further machined flat using a rotating polishing wheel at 600 grit.

4.2.1 Electrical Conductivity testing

Wires were attached to each of the specimens as shown in Figure 4-1 using a silver-filled epoxy solder to enable the resistance of the specimens to be measured. The four point method was opted for to mitigate contact-resistance anomalies which can occur when the

current and voltage drop are measured at the same point. The current was allowed to flow through the entire specimen forming the primary circuit, and the voltage drop was measured across a spacing of 40mm in a secondary circuit. For each specimen, the applied voltage generated by the power supply in the primary circuit was incremented from 1 to 3 to 5 V DC and resistance measurements were taken at each applied voltage (calculated by R = V/I). All specimens displayed Ohmic behavior. The current and voltage drop were measured using multimeters with lower detection thresholds of 10µA and 1mV respectively.
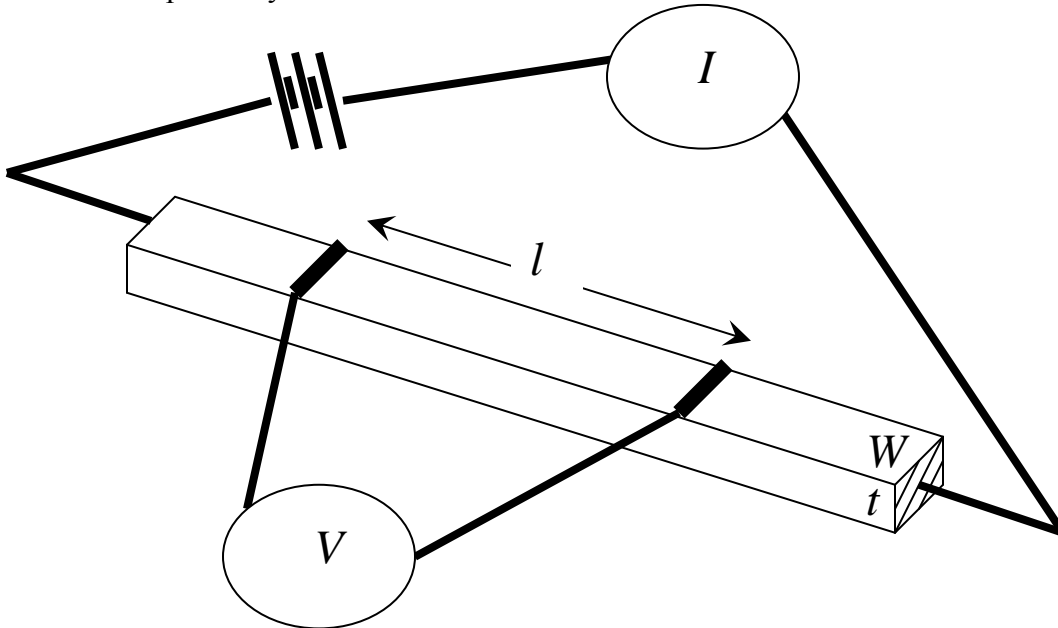
Figure 4-1 Electrical conductivity testing

The actual dimensions and gap spacing (l) of each specimen were carefully measured, and the resistivity of each specimen was calculated by:

(4-1) $\rho = \dfrac{R}{l} A$

The cross-sectional area, A was simply Wt. The conductivity was taken as the inverse of the resistivity.

4.2.2 Thermal conductivity testing

Measuring the thermal conductivity involved 3 discrete measurements one each for thermal diffusivity, bulk density, and heat capacity, their product being the thermal conductivity as shown in Equation (4-2). Values of each at room temperature were used to calculate the room temperature thermal conductivity, which was used for subsequent comparison between composite epoxies.

(4-2) $k = \alpha \rho C_p$

For thermal diffusivity, the laser flash technique was used (Netzsch LFA 427). The laser flash technique instantaneously heats the bottom face of the specimen using a laser pulse. Meanwhile, the temperature of the specimen's top face is monitored by an infrared detector. As a function of time, starting from the pulse, the temperature of the top face increases to an equilibrium creating an S-shaped curve. The point of inflection of the

curve, or half-time of heat up, combined with a known specimen thickness, enables the thermal diffusivity to be calculated. Prior to testing, specimens of 12.7 mm diameter and 2mm thickness were machined from the original cured sample. The mass of each was measured, which enabled a bulk density to be calculated. A laser voltage of 450V and a pulse-width of 0.5ms were used throughout LFA testing. Smaller samples, 4.75mm diameter by 0.5mm thickness were machined and their heat capacity measured by modulated differential scanning calorimetry (MDSC) (TA Instruments Q100).

4.3 Results and Discussion

Microscopy

Thin sections of cured specimens were cut using a diamond saw and examined under an optical microscope with a UV fluorescence technique. Good contrast in the images was obtained because the epoxy matrix fluoresced visible light whereas the carbon fillers did not. A qualitative measure of the dispersion was discernable from the photomicrographs of the epoxy composites (Figure 4-2). For MWNTs, it is clear that at high loadings (2 vol% and 5 vol%), large agglomerates were present, but were absent in samples of lower MWNT loadings. It is apparent that the high aspect ratio of the MWNTs is advantageous for the formation of the conductive network at low volume fractions. Microscopic fibrous structures are visible bridging through the composite even at 0.1 vol%. At concentrations higher than 1 vol%, agglomerates may remain due to poor circulation of the more viscous material through the mixer head, or the agglomerates may be forming as the concentration of MWNTs increases due to entanglement. In any case, 1 vol.% MWNTs represented the upper limit for homogeneous dispersion. Higher loadings displayed viscosities that rendered them un-processable in any practical sense.

| 0.1 vol% | 0.5 vol% | 1 vol% | 2 vol% | 5 vol% |
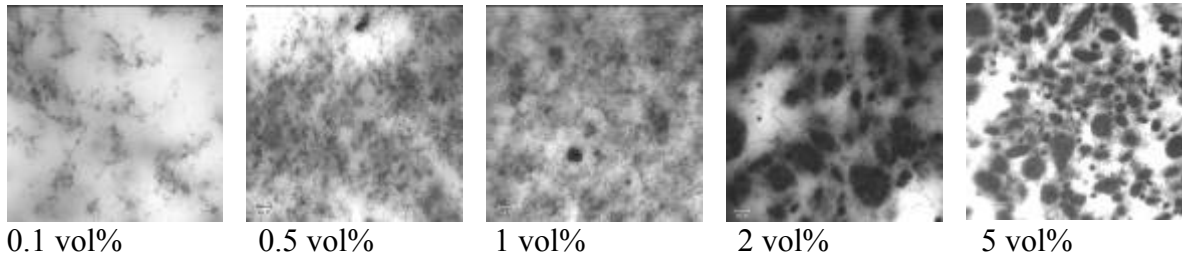
Figure 4-2 Dispersion of MWNTs
UV fluorescent light micrographs of thin sections of MWNT/epoxy composites.

For comparison, dispersion of carbon black in epoxy is show in Figure 4-3 below. The carbon black particles immediately flocculate into microscopic aggregates, which form a network via small interconnects. No fibrous-like junctions are discernable. These aggregates continue to pack into a dense structure up to 5 vol.%, and the increase in resin viscosity was not as drastic as with MWNTs. The particles of CB can not entangle due to their low aspect ratio, and thus have a diminished effect on increasing the resin viscosity.
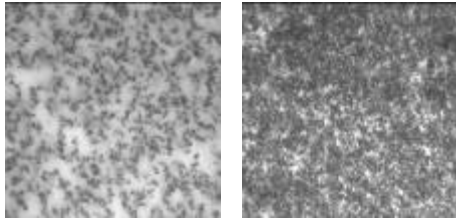
1 vol%   5 vol%

Figure 4-3 Dispersion of carbon black
Transmitted light micrographs of carbon black/epoxy MWNTs.

Electrical Conductivity
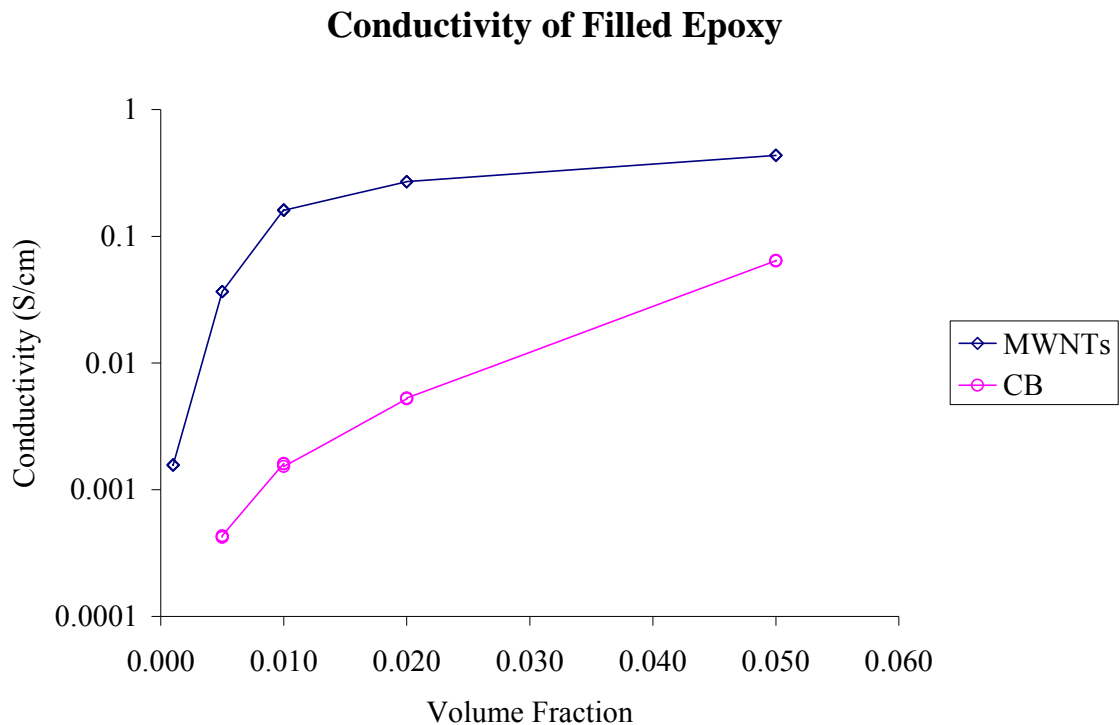
Figure 4-4 Electrical conductivity results
Electrical conductivity of MWNT and carbon black epoxy composites.

Figure 4-4 shows the conductivities of the filled epoxy for both MWNTs and CB fillers as a function of volume fraction. The conductivity of the pure epoxy was not measureable with the equipment employed, but is assumed to be in the 10^{-13} to 10^{-15} S/cm range[182]. MWNT-filled epoxy became measurably conductive at 0.1 vol.% while CB-filled epoxy only became measurably conductive at 0.5 vol.%, which is indicative of the MWNTs forming a conductive network at a much lower concentration or percolation threshold. With respect to the magnitude of the conductivity, MWNTs clearly out-performed the CB filler. The electrical conductivity of the MWNT filled epoxy quickly increased up to a value of 0.44 S/cm at 5.0 vol.%. To the author's knowledge, this represents the highest conductivity in a nanotube filled epoxy, at this concentration, reported to date. CB-filled epoxy increased in conductivity much slower and to lesser of

a degree. In the concentration range studied, CB-filled epoxy was always at least one order of magnitude lower in electrical conductivity than its MWNT-filled analogue.

The surface resistivity (or sheet resistance) of the specimens was calculated by simply dividing the bulk conductivity values by the thickness of the specimen. Surface resistivity is an important parameter used in the characterization of coatings and semiconducting wafers. The results are shown in Figure 4-5. At 1.0 vol.%, the surface resistivity of the MWNT epoxy composite was approximately 10 ohms/square, whereas the carbon black was 1000 ohms/square. Here very low surface resistivity is achievable at a very low volume fraction of MWNTs, and may enable MWNT epoxy composites to be easily electrostatically painted or to function as electromagnetic interference shielding materials. They are certainly conductive enough for anti-static applications, where nominal surface conductivities of 10^6 ohm/square are necessary.

Surface Resistance of Filled-Epoxy
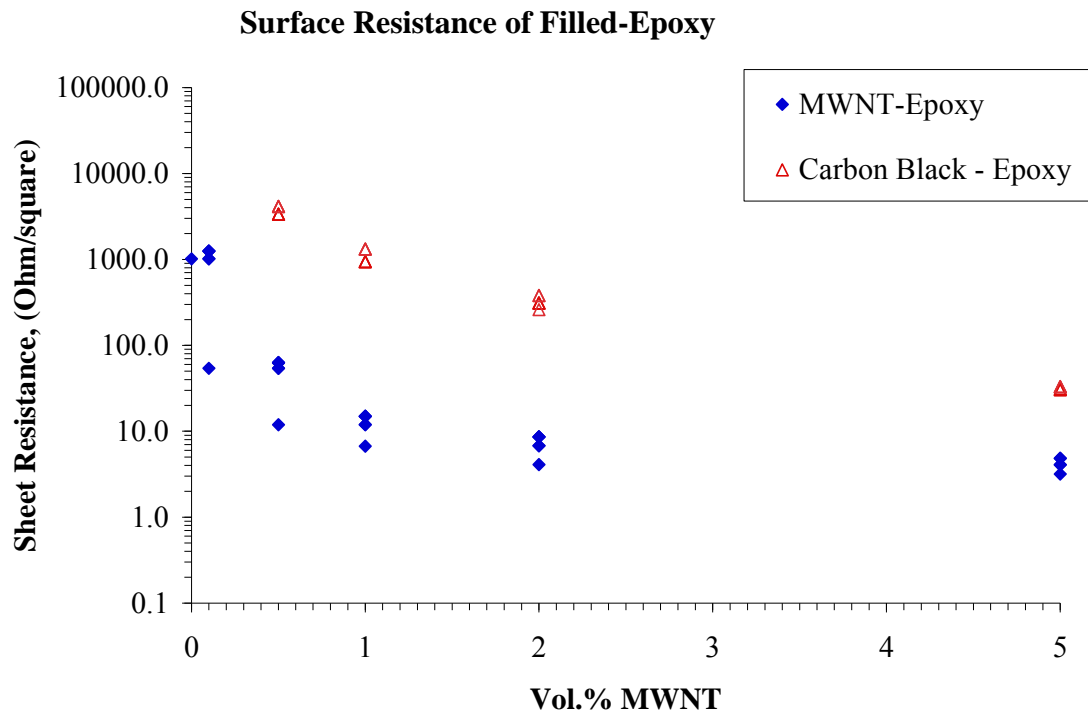
Figure 4-5 Surface resistance results

Although determination of the percolation threshold in the composite epoxies was not a primary focus, an effort to analyze where it was likely to have occurred was undertaken. Better analysis of the percolation threshold would have required more specimens at lower concentrations to have been measured, as well as the use of more accurate measuring equipment. Nevertheless, typical percolation scaling laws take the form of:

(4-1) $\sigma = \sigma_0 (p - p_c)^t$

Where σ is the composite conductivity after percolation, p is the mass or volume fraction of filler, p_c is the percolation threshold and σ_0 and t are constants. Theoretically, t should be 2 (for 3-dimensional percolation), and σ_0 should be the conductivity of the filler phase. A plot of log(conductivity) versus log(volume fraction) showed in Figure 4-6 displayed

good linearity, which indicated that the percolation threshold occurred at concentrations below those measured. As a first approximation, the percolation threshold was taken as the concentration value of the linear fit when the electrical conductivity equaled 10^{-3} S/cm, which is in agreement with the point of percolation by numerous researchers[158, 160]. It was found that the percolation thresholds were 0.053 vol.%, and 0.75 vol% for MWNTs and CB respectively, which are values quite similar to those reported in literature[30, 57]. Furthermore, the slope of the linear fit, to the carbon black-filled epoxy, was close to 2 as expected for 3 dimensional percolation. The slope of the MWNT-filled epoxy was less than 2, which may indicate some degree of preferred orientation of the MWNTs within the epoxy. Interpretation of both fits suggests that irrespective of what the percolation threshold conductivity is, MWNTs-filled epoxy will attain it at concentrations of at least one order of magnitude lower than CB-filled epoxy.
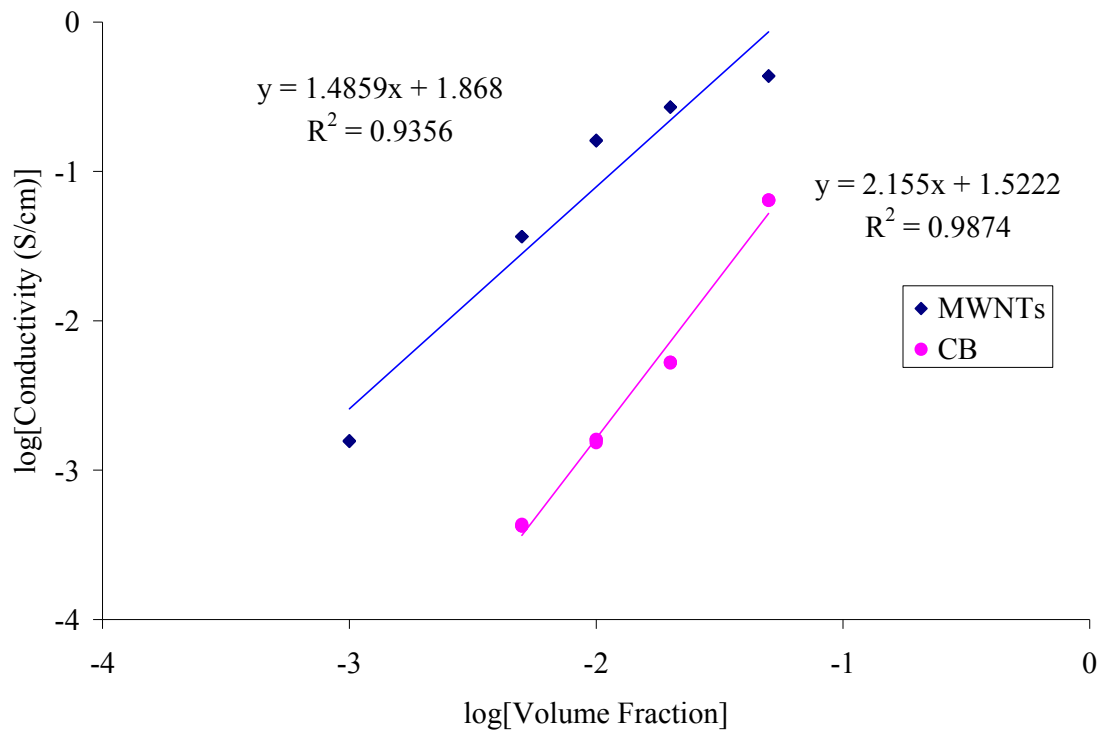
Figure 4-6 Electrical conductivity percolation

The mechanism for charge transfer between embedded MWNTs or CB with an insulating matrix has been discussed in terms of quantum tunneling of electrons through the potential barrier resulting from a thin polymeric coating of the embedded carbon conductors[57, 100, 158]. Prior analysis of these cases suggested that if a plot of the log conductivity versus volume fraction$^{(-1/3)}$ was linear, electron tunneling is the mechanism of conduction. The basis for this relationship is that the average gap width between neighboring nanotubes reduces as the concentration is increases. The number of contacts should also increase as concentration increases. Thus the tunneling potential barrier decreases as conductivity increases. A similar plot, using the conductivity data acquired in this work, does in fact generate nice linear fits as shown in Figure 4-7. Detailed study

into the mechanism of charge transport is normally done by studying conductivity as a function of temperature beginning at liquid He temperatures. This is discussed in Chapter 1.

Graph plotting $\ln[\text{Conductivity, (Ohm-cm)}]$ on the y-axis (ranging from 0 to -9) versus $(\text{Volume Fraction})^{-1/3}$ on the x-axis (ranging from 0 to 12). Two data series are shown: Carbon Black (diamonds) with fit line $y = -1.5537x + 1.0078$, $R^2 = 0.9515$; and MWNTs (squares) with fit line $y = -0.7987x + 1.5472$, $R^2 = 0.9905$.
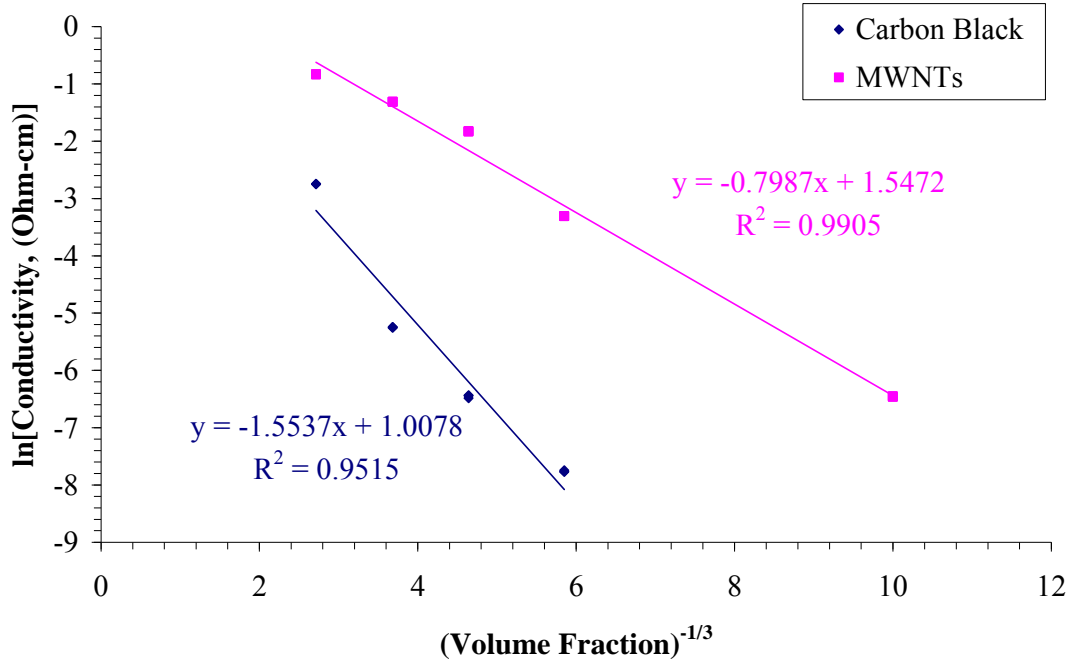
Figure 4-7 Electrical conductivity mechanism

Thermal Conductivity

Unlike electrical conductivity, where a sharp increase of several orders of magnitude in conductivity occurs in accordance with the initial formation of a percolated network, no such increase in thermal conductivity occurs. Severe limitations on the efficiency of thermal transport between polymeric matrices and embedded MWNTs occur. Soft polymers preferentially transport low frequency phonons across their interface to the highly conductive MWNTs. The results of the MWNT and composite epoxy are presented in Table 4.1. Although significant increases in thermal conductivity were measured with increasing concentration, the value of thermal conductivity increased only modestly. MWNTs, as in electrical conductivity, clearly out-perform CB fillers. At the highest loadings, increases of 245% and 46% were observed for MWNTs and CB respectively. The thermal conductivity within the temperature range of room temperature to 100°C was shown not to change significantly (Figure 4-8).

Table 4.1 Thermal conductivity of MWNT and CB composite epoxy

| Filler	Filler (Vol. %)	Heat Capacity (J/gK)	Thermal Diffusivity (mm2/sec)	Density (g/cm3)	Thermal Conductivity (W/mK)
(none)	0	1.408	0.132	1.1629	0.216
MWNT	0.1	1.429	0.138	1.1980	0.236
MWNT	0.5	1.393	0.168	1.1978	0.280
MWNT	1.0	1.438	0.236	1.1487	0.390
MWNT	2.0	1.396	0.294	1.1666	0.479
MWNT	5.0	1.446	0.425	1.2123	0.745
Carbon Black	0.1	1.656	0.095	1.1545	0.182
Carbon Black	0.5	1.532	0.150	1.1907	0.274
Carbon Black	1.0	1.489	0.141	1.1760	0.247
Carbon Black	2.0	1.474	0.141	1.1816	0.246
Carbon Black	5.0	1.511	0.177	1.1785	0.315
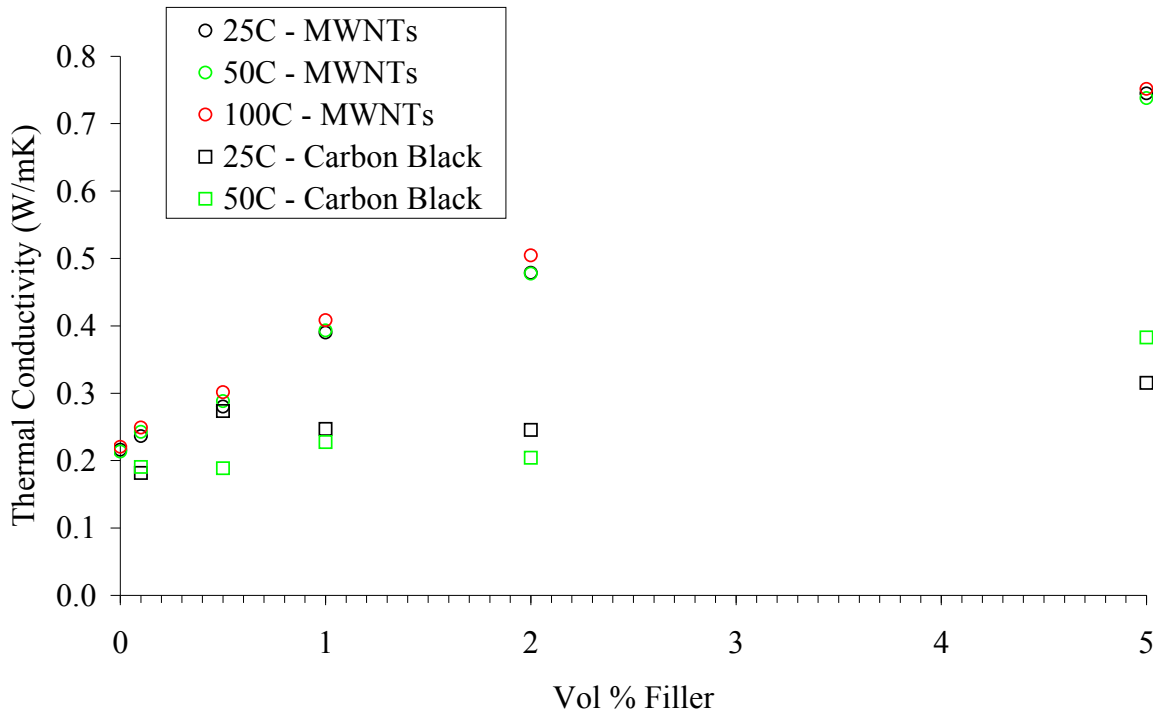
Figure 4-8 Thermal conductivity of MWNT and CB composite epoxy

The increases in thermal conductivity were modeled using the effective medium approach described in Chapter 1, using equation (1-12). For MWNTs, the thermal conductivity was taken as 700 W/mK[30, 31], the aspect ratio as 1000, and the diameter to be 30nm. The interfacial resistance to heat conduction (Kapitza resistance) was used as a fitting parameter to the data and found to be 4.2×10^{-7} m^2K/W, which is much lower than previously reported[166, 167], and may be indicative of relatively good thermal transport in the MWNT epoxy composites. Similarly, the thermal conductivity of the carbon black epoxy composites was modeled. Here the conductivity of the carbon black was taken as 200 W/mK, the aspect ratio as 1, and the diameter of the particles to be 50nm. In this case the Kapitza resistance was found to be 3.7×10^{-9} m^2K/W. Increasing the coupling between the embedded carbon fillers and the epoxy matrix would clearly be beneficial to the overall thermal conductivity, but is likely to be difficult to demonstrate in practice.
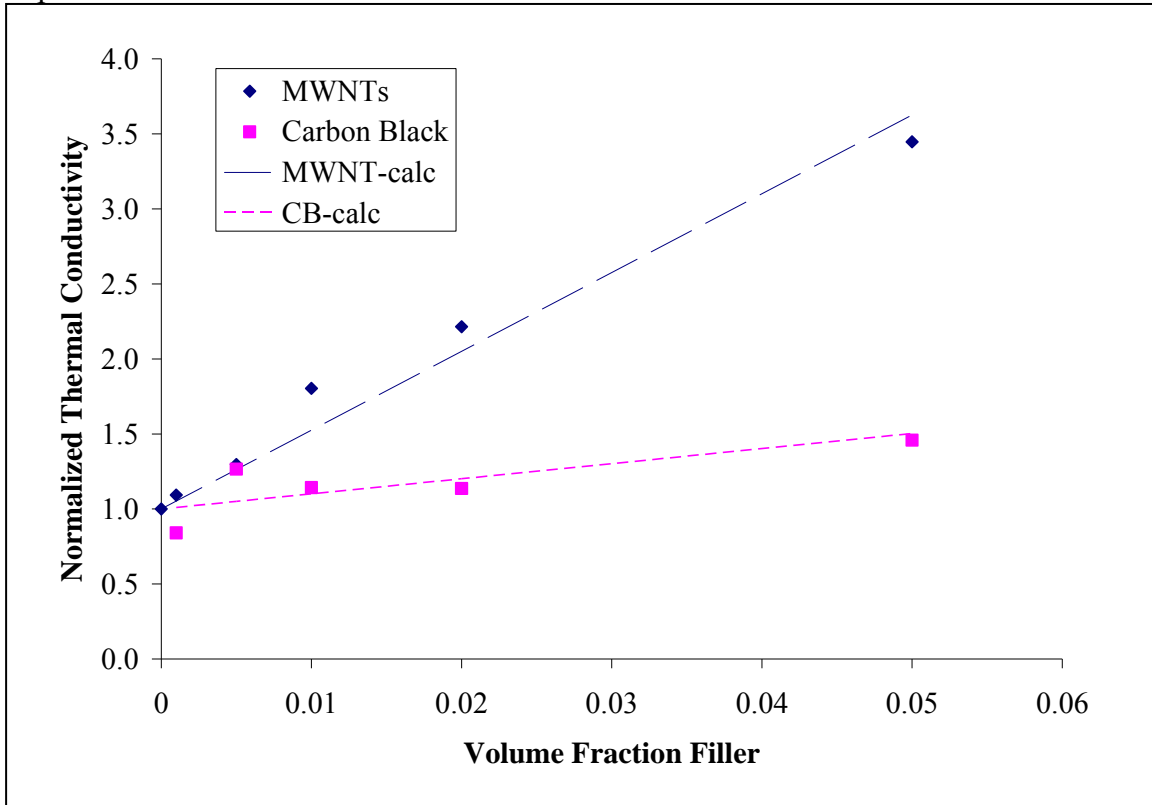
Figure 4-9 Increases in thermal conductivity

4.3.1 Epoxy Infiltrated Aligned MWNT Arrays

In an effort to by-pass the limitations of interfacial thermal transport, and to take advantage of the highly aligned morphology of the as-grown MWNTs, epoxy infiltration into MWNT arrays was investigated as a method of producing highly thermally conductive films. Figure 4-10(c) shows the morphology of the as-grown MWNT arrays. An alteration of the CVD method used to synthesis the MWNTs was employed to make

the MWNT grow to longer lengths, which in this case can be referred to as mat thickness. By carefully removing the arrays from the quartz substrate using a razor it was shown that they could be detached from the underlying substrate in large, continuous mats. During removal from the substrate without any polymer infiltration, the MWNT arrays typically rolled into 'rolled carpet' structures as seen in Figure 4-10 (a-b).

Figure 4-10 Aligned MWNT arrays
In photo (A), the structure of the as-grown multiwall carbon nanotube (MWNT) array is shown post removal from the substrate. The inset yellow circle highlights the mat thickness which is shown in picture (B). SEM Micrograph (C) clearly shows the aligned structure of the individual MWNTs through the thickness of the mat.

The process of infiltrating the epoxy into the MWNT began while they were still attached to the substrate. A thin layer of liquid epoxy-hardener mixture was wiped on to a thin Teflon sheet and p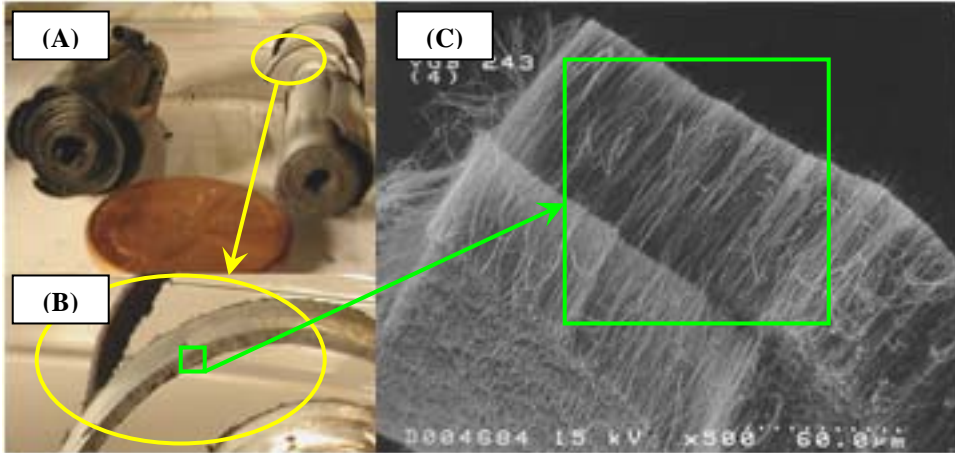laced flat over the MWNT array. A weight was used to apply a small amount of pressure evenly over the array surface, and capillary action of the interstices in the MWNT array drew the epoxy into the array. The epoxy was allowed to partially cure, and the infiltrated array was carefully removed from the substrate using a razor in large continuous pieces. No volatile solvents were used to prevent warpage or otherwise destruction of the aligned nature of the array that can occur during evaporation and shrinkage. Images of the collected epoxy infiltrate MWNT arrays are shown in Figure 4-11(a-c). Single pieces of up to 4" x 10" in size were successfully infiltrated and removed. Normal thicknesses of the arrays were approximately 0.5mm. The infiltrated arrays were then heated to 150ºC to ensure full curing of the epoxy and specimens of the material were cut and analyzed for thermal conductivity.

The thermal conductivity results are shown, in conjunction with the previously measured dispersed MWNT and CB epoxy composites, in Figure 4-12. Massive increases in thermal conductivity over the dispersed systems were observed, and measured to be in the 15-20 W/mK range. This constitutes an improvement over neat epoxy by a factor of 70 to 93. TGA analysis of the infiltrated arrays showed them to contain approximately 47wt.% or 35vol.% MWNT (densities 2.0 g/cc and 1.2 g/cc of MWNTs and epoxy respectively).
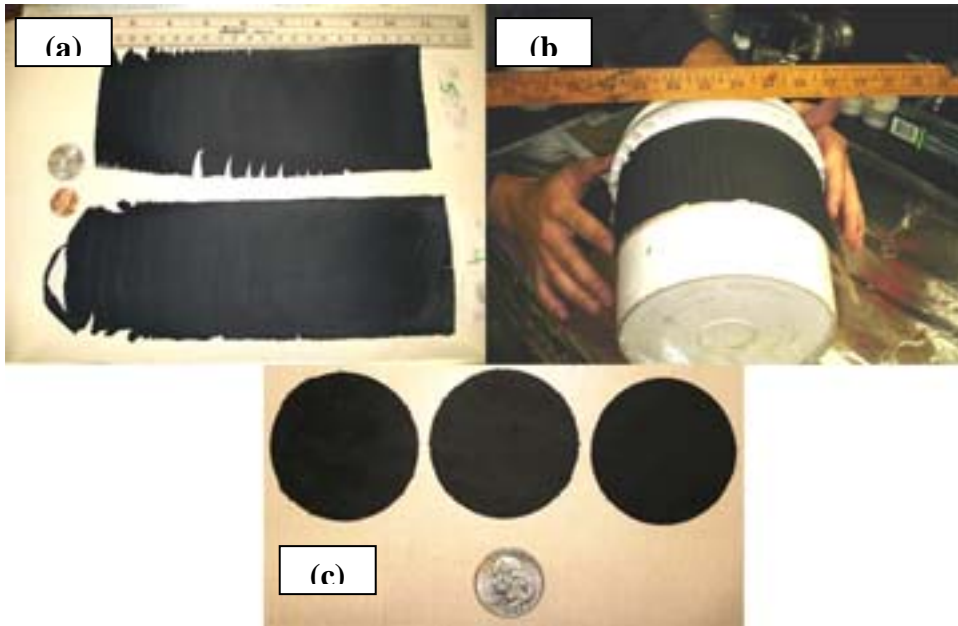
Figure 4-11 Epoxy infiltrated aligned MWNT arrays
In photo (a) two, free-standing, epoxy-infiltrated cured MWNT arrays are shown that are approximately 3"
x 8" and 0.5mm thick. Photo (E) illustrates how these mats can be used in applications requiring the mats
to wrap or conform to surfaces. Photo (F) illustrates small discs made from arrays similar to those shown
in (D).

Thermal Conductivity of Filled-Epoxy
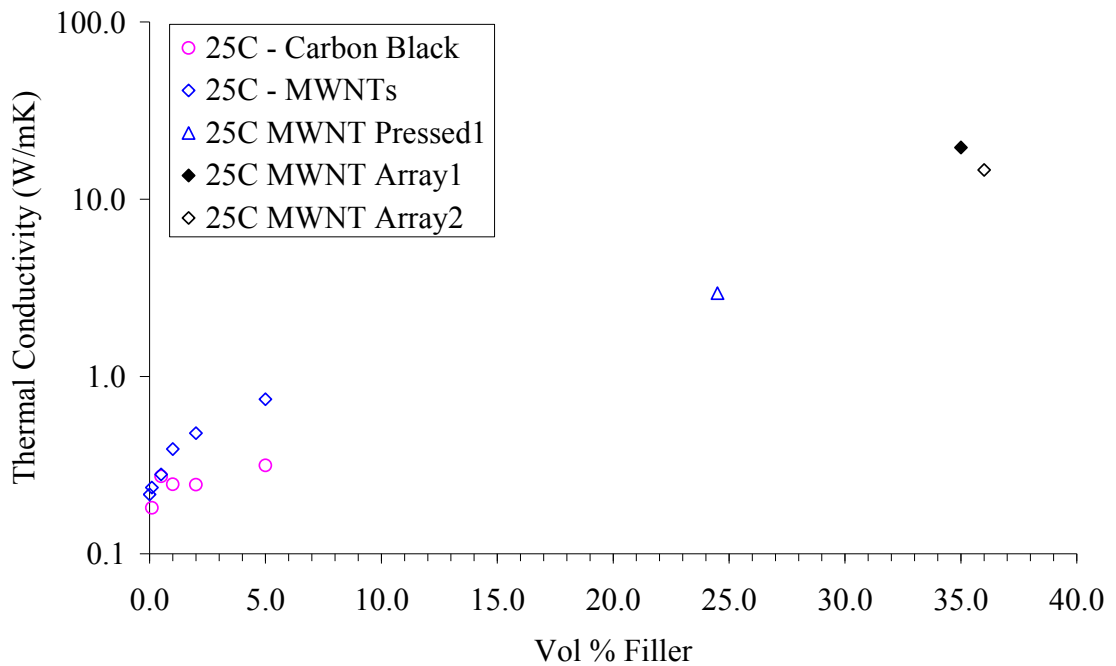
Figure 4-12 Thermal conductivity of infiltrated MWNT arrays

74

The thermal conductivity of a piece of the infiltrated array that was intentionally folded, mashed and pressed (to destroy its aligned character) was measured at approximately 3 W/mK. This is conclusive evidence that the alignment of the MWNTs is critical for maximizing thermal conductivity. This is not unexpected given the highly anisotropic nature of the thermal conductivity of carbon nanotubes. Furthermore, the infiltrated arrays were measured to have bulk densities of approximately 1g/cc.
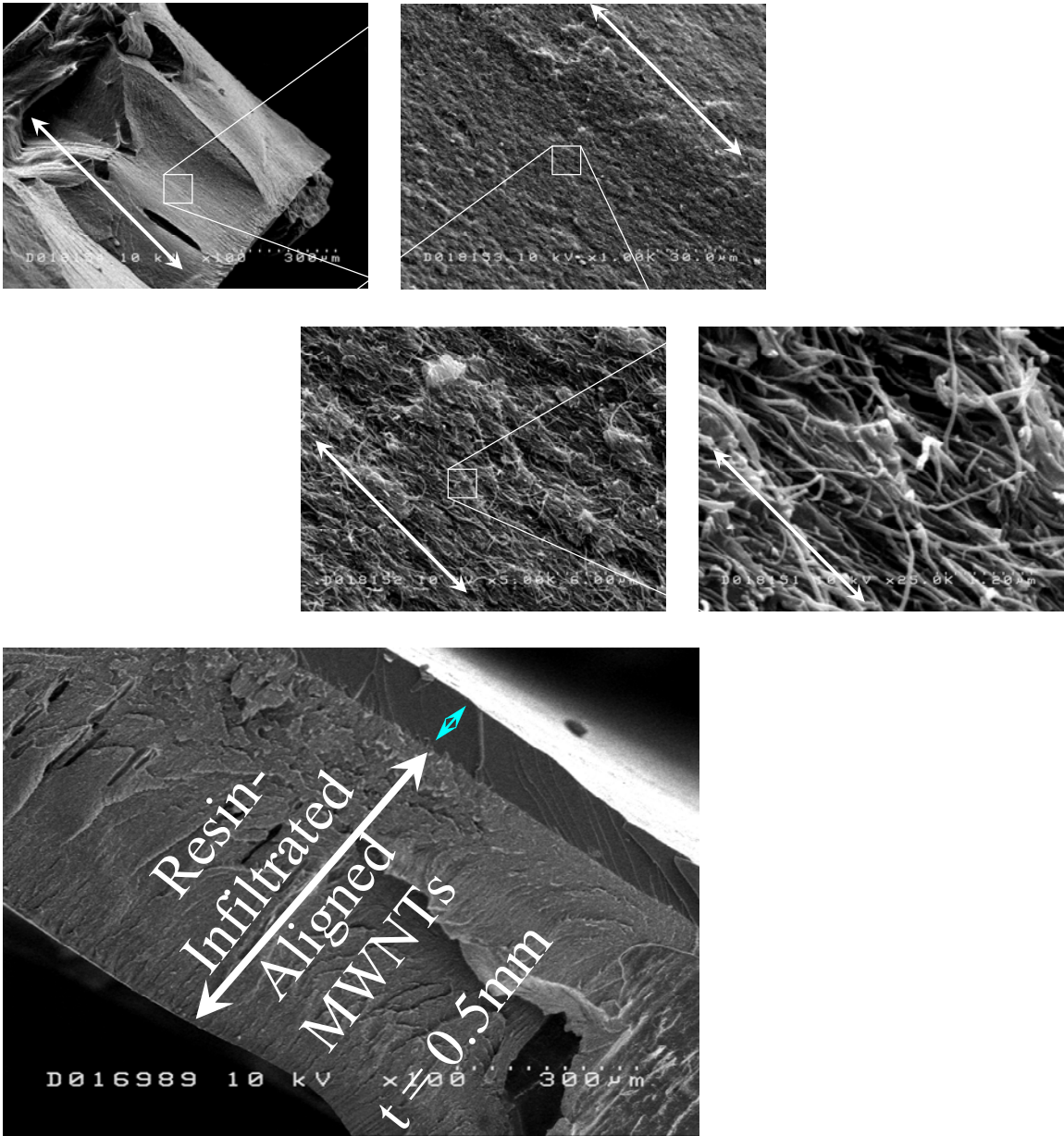
Figure 4-13 Microstructure of infiltrated MWNT arrays

SEM imaging of an epoxy infiltrated array is shown in Figure 4-13. The aligned character of the MWNT array is preserved during through fabrication of the cured, infiltrated array. The lower portion of Figure 4-13 shows a wide-field view edge-on where complete infiltration of the epoxy is noted. At the top of this particular array, a

layer of neat epoxy is discernable. Because epoxy infiltration is done while the arrays are still bound to their underlying substrates, they remain vulnerable to excess epoxy. By controlling the amount of epoxy charged to the Teflon film prior to infiltration, the amount of epoxy in the final arrays can be controlled. Current work on this subject has generated infiltrated arrays that have little epoxy coating on the topside of the array as they are immediately electrically conductive through their thickness upon removal from the substrate.

This material may be ideally suited for applications in which through-thickness thermal conductivity and weight considerations are critical. The thermal conductivities of the infiltrated arrays are equivalent to stainless steel at a fraction of the density. Potential applications may included thermal transport films for interfaces between heat generators and heat sinks, such as the interface between IC chips and their heat sinks, or as interfacial layers in laminated or filament wound composite structures. The latter application was investigated by incorporating the arrays into the interlaminar region (between winding passes) in the production of a carbon fiber/epoxy filament wound composite tube. Similar analysis of the thermal conductivity of specimens of this material demonstrated more than a 100% improvement of the overall through-thickness thermal conductivity. When 1wt.% composite epoxy was used in concert during the filament winding process, even higher increases in thermal conductivity were observed (+250%). The results are shown in Figure 4-14.
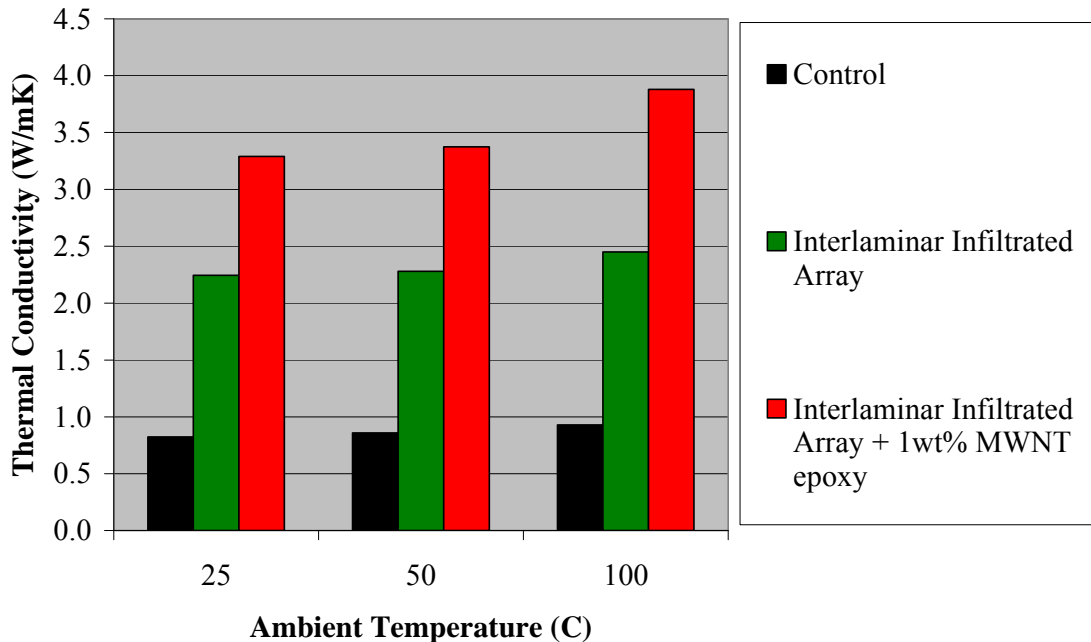
Figure 4-14 Thermal conductivity of filament wound – infiltrated array composites

4.4 Conclusions

In this chapter the electrical and thermal conductivities of MWNT filled epoxies were measured and compared to CB filled epoxies. The percolation thresholds for electrical conductivity in MWNT and CB epoxy were found to occur at approximately 0.053 vol.%, and 0.75 vol% respectively. The magnitude of the electrical conductivity of the MWNT filled epoxy was always approximately 1 order of magnitude higher than that of CB at equivalent loadings, and was found to reach as high as 0.44 S/cm at 5.0 vol.% MWNTs. The thermal conductivities of both composites were also measured, and again, MWNTs clearly performed superior to CB where increases of 245% and 46% were observed for MWNTs and CB respectively. Aligned arrays of MWNTs grown on quartz substrates were successfully infiltrated with epoxy, and removed, in large films, from the substrate. The thermal conductivity through the thickness of these materials was extremely high (15-20 W/mK), which represented an increase in thermal conductivity of 70-90 times higher than the neat epoxy. Furthermore, the application of these infiltrated arrays as promoters of through-thickness conductivity by incorporation into the interlaminar regions of filament wound carbon fiber epoxy structures, showed great promise.

In this dissertation, the results of investigations into three separate carbon nanotube composites were presented and discussed. Within each, key properties were investigated and analyzed, which in total, covered a scope of envisioned carbon nanotube composite applications.

Mechanical Reinforcement

For mechanical reinforcement, a survey of the literature in Chapter 1 indicated that enhancements of the modulus and strength of polymers were predominantly modest, except when the embedded nanotubes served to induce a tightly bonded, ordered layer of matrix polymer at the nanotube interface. The incorporation of MWNTs in PAN-based carbon fiber was explored in Chapter 2. Production of these fibers was processing-intensive, and although, an ordered layer of templated carbon was indeed observed circumferentially bound to the MWNTs, no enhancement in the modulus of the fibers was observed, and in fact decreases occurred. Imaging of the fiber fracture surfaces indicated that these decreases may be linked to a lack of interfacial bonding of the interphase to the surrounding bulk matrix fiber. Tensioning of these fibers during the carbonization was also shown to be crucial for the development of high performance properties. Further investigation into MWNT composite carbon fibers is likely to focus on increasing the bonding of the embedded MWNTs throughout the bulk fiber and determining the effect of the carbonization temperature on the final composite carbon fiber properties. Fibers initially containing less than 10wt% MWNTs may be preferred. Painstaking optimization of the processing parameters from spinning through carbonization is likely to be of vital application for further development. If MWNT + interphase debonding is found to be mitigated at lower carbonization temperatures, and reinforcement of the matrix carbon fiber by the MWNTs is realized, it may enable the production of high performance carbon fibers at significantly lower energy costs.

In Chapter 3, the fatigue performance of MWNT composite PMMA was investigated and revealed stunningly positive results. Even in direct comparison to a high-strength chopped carbon fiber filler, the MWNTs performed markedly better. 1.0 vol% of MWNTs, melt mixed into the PMMA matrix was found to increase the fatigue performance by 623%, whereas CCF enhanced it by only 244%. The enhancements were shown to be amplified at lower strain amplitude cyclical deflection of the specimens. The improvements in the fatigue performance are in stark contrast with other mechanical properties of nanotube composites where quasi-static testing to failure is done to evaluate modulus and strength. The small dimensions of MWNTs directly enable them to interact and impede damage mechanisms related to subsequent fatigue failure such as craze coalescence and crack propagation. Furthermore, MWNTs may be ideal candidates for enhancing other related material properties in polymers where low stress plastic deformation dominates such as in creep.

Electrical and Thermal Conductivity

In Chapter 4, the electrical and thermal conduction properties of MWNT composite epoxy were investigated and directly compared to CB filled epoxy. The percolation thresholds for electrical conductivity in MWNT and CB epoxy were found to occur at approximately 0.053 vol.%, and 0.75 vol% respectively. The magnitude of the electrical conductivity of the MWNT filled epoxy was always approximately 1 order of magnitude higher than that of CB at equivalent loadings, and was found to reach as high as 0.44 S/cm at 5.0 vol.%. The thermal conductivities of both composites were also measured, and again, MWNTs clearly performed superior to CB where increases of 245% and 46% were observed for MWNTs and CB respectively. Aligned arrays of MWNTs grown on quartz substrates were successfully infiltrated with epoxy, and removed in large films from the substrate. The thermal conductivity through the thickness of these materials was extremely high (15-20 W/mK), which represented an increase in thermal conductivity of 70-90 times higher than the neat epoxy. Furthermore, the application of these infiltrated arrays as promoters of through-thickness conductivity by incorporation into the interlaminar regions of filament wound carbon fiber epoxy structures, showed great promise.

Concluding Remarks on MWNT Composites

Harnessing the desirable mechanical properties of MWNTs in practical engineering materials remains a difficult task. Although increases have been noted in the literature, most of the best increases are reported in, perhaps, less than desirable matrices such as PVA (which does not have good solid properties and swells and dissolves in water), involve processing methods which are simply not industrial viable, and in many cases in increases in matrix properties are the result of the MWNT inducing a sheathing of ordered matrix. The general conclusion from the literature is that by simply mixing MWNTs into commodity thermoplastics, where application could be significant, does not efficiently increase the properties of the matrix. MWNT composite fibers, however, offer a way in which the desired orientation of the MWNT is a built-in function of the necessary processing regardless of any filler. It is partly for this reason that MWNT PAN precursor fibers were studied in this dissertation.

The other part was to determine whether the templating effect of the MWNTs, mentioned above, would lead to a fiber structure of higher performance. It was considered that by carbonizing the MWNT PAN composite fibers, a templated structure would form an interphase with high adhesion to the MWNTs. Although templating of the MWNTs did occur, and they appeared to bond very well to the MWNTs, the interphase did not bond well or at all to the matrix, and no enhancement in modulus or strength occurred. These materials had modest increases in break strain, which in some cases led to an increase in toughness. In any case, the results and observations generated in this study may be useful for further attempts to improve the overall adhesion or continuity between MWNTs and carbon matrices, which may lead to high performance. Or perhaps simply increasing the break strain of certain types of carbon fiber may be the desired effect. One example may be in high modulus mesophase pitch based carbon fiber where break strength, toughness and handle-ability are limited by low break strains.

MWNTs proved to be very effective for increasing the fatigue performance of PMMA. This effect should be useful for increasing the fatigue performance of any amorphous thermoplastic. Evidence points to the fact the MWNTs, due to their small size, are effective in mitigating the accumulation of damage incurred by cyclical deformation by mitigating craze formation and crack propagation. The area of MWNT composites for fatigue enhancement is, currently, an overlooked region of MWNT composite research. Furthermore, given that creep involves many of the same damage mechanisms found in fatigue, MWNTs may be equally effective for mitigating creep in amorphous polymers. Most applications in which creep is an issue do not even consider a polymeric material for design. Whether or not similar improvements in fatigue or creep performance would translate in semi-crystalline polymeric matrices is an open question. These are areas, however, where MWNT composites are likely to enjoy success.

Electrically conductive polymer-MWNT composites can be easily produced. Results in this dissertation, and throughout the literature, suggest that the percolation threshold for MWNTs is less than 0.1vol% whereas CB composites are in the 1vol% range. Applications for polymeric composites that are slightly conductive (near the percolation threshold) typically include anti-static electronics packaging materials. Given the difference in percolation threshold, MWNTs would approximately need to cost no more than 10 times carbon black. Whether or not MWNTs will ever be this cheap is questionable. However, MWNTs may in fact find application in composites where the electrical conductivity needs to be in the 1-10 S/cm range, or beyond the reach of carbon black composites, and the conductive composite needs to be light. Economically, MWNTs may have a chance here given that typical highly conductive polymer composites use silver or gold filled epoxy, which is both heavy and expensive. Demonstration of substantial EMI shielding by a MWNT filled epoxy, may well find application in military or aviation electronics.

Highly thermally conductive MWNT polymer composites are not likely to be produced by simply mixing small amounts of MWNTs into a polymer matrix. The inefficiencies in heat transfer from polymer to nanotube are simply too large. However, infiltrating polymer into an aligned MWNT array to produce a composite film does indeed result in a highly thermally conductive material. Secondly, it is anisotropically conductive where heat transport is favored through its thickness. Numerous applications exist for through-thickness thermal transport, or where transport through an interface between parts is the problem. Even within this dissertation it was shown how epoxy infiltrated MWNT arrays function to increase thermal transport through the thickness of a filament wound carbon fiber-epoxy structure. This material has large potential for application.

As the field of carbon nanotube composites continues to move forward, many of the issues above will continue to be investigated and analyzed. Of all the mechanical, electrical, and thermal properties discussed in this dissertation, I conclude that the areas most fruitful for application are MWNTs for fatigue enhancement (possibly creep enhancement) of amorphous polymers, and polymer infiltrated aligned MWNT arrays for through thickness thermal conductivity. Other applications which take advantage of the

highly-aligned, as-grown MWNT mat structure are likely also to be successful due to the uniqueness of the structure combined with its constituents' desirable properties. In any case it will be interesting to see whether the above carved out niche applications for nanotube composites will thrive in the future. But more than likely, many exciting applications of nantoubes will involve things yet-to-be discovered or ideas yet-to-be formed.

APPENDIX A MWNT Diameter and Length Distribution

Length Distribution of MWNTs
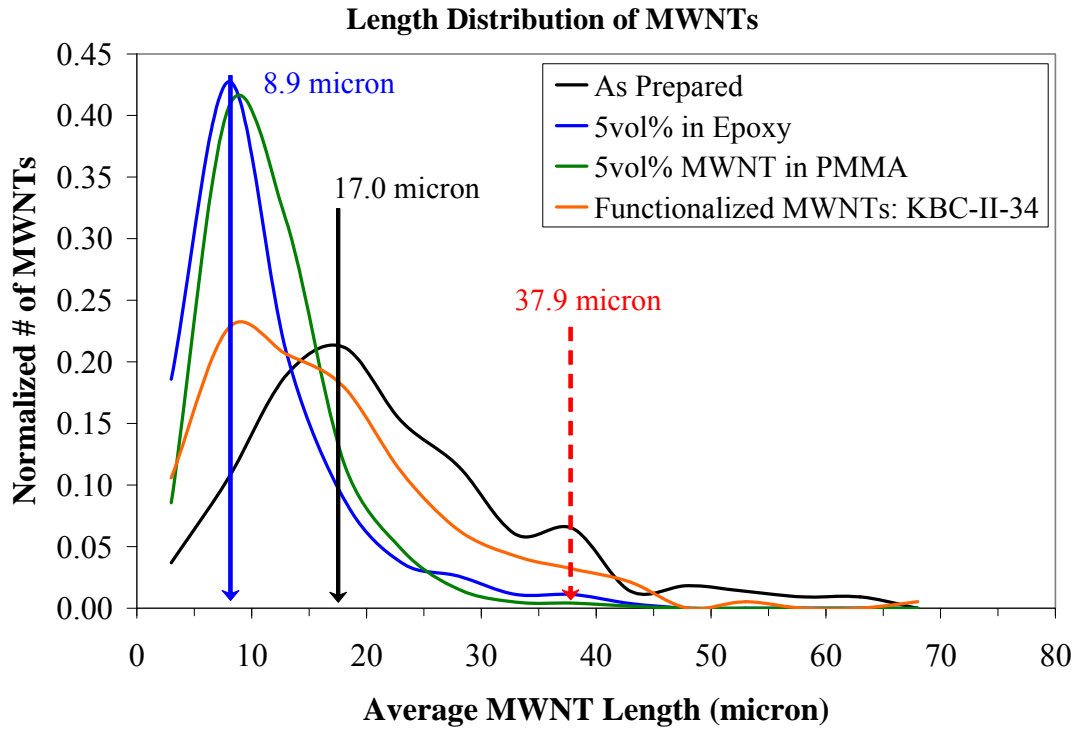
Figure A-1 MWNT length distribution
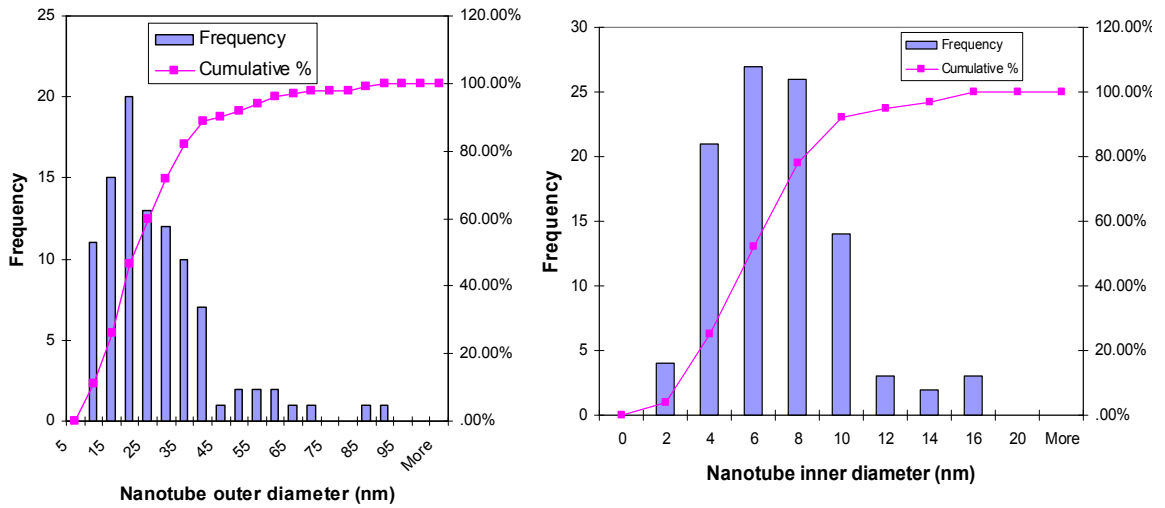
Figure A-2 MWNT outer and inner diameter distributions

APPENDIX B SEM Fracture Surfaces of MWNT Composite Carbon Fibers
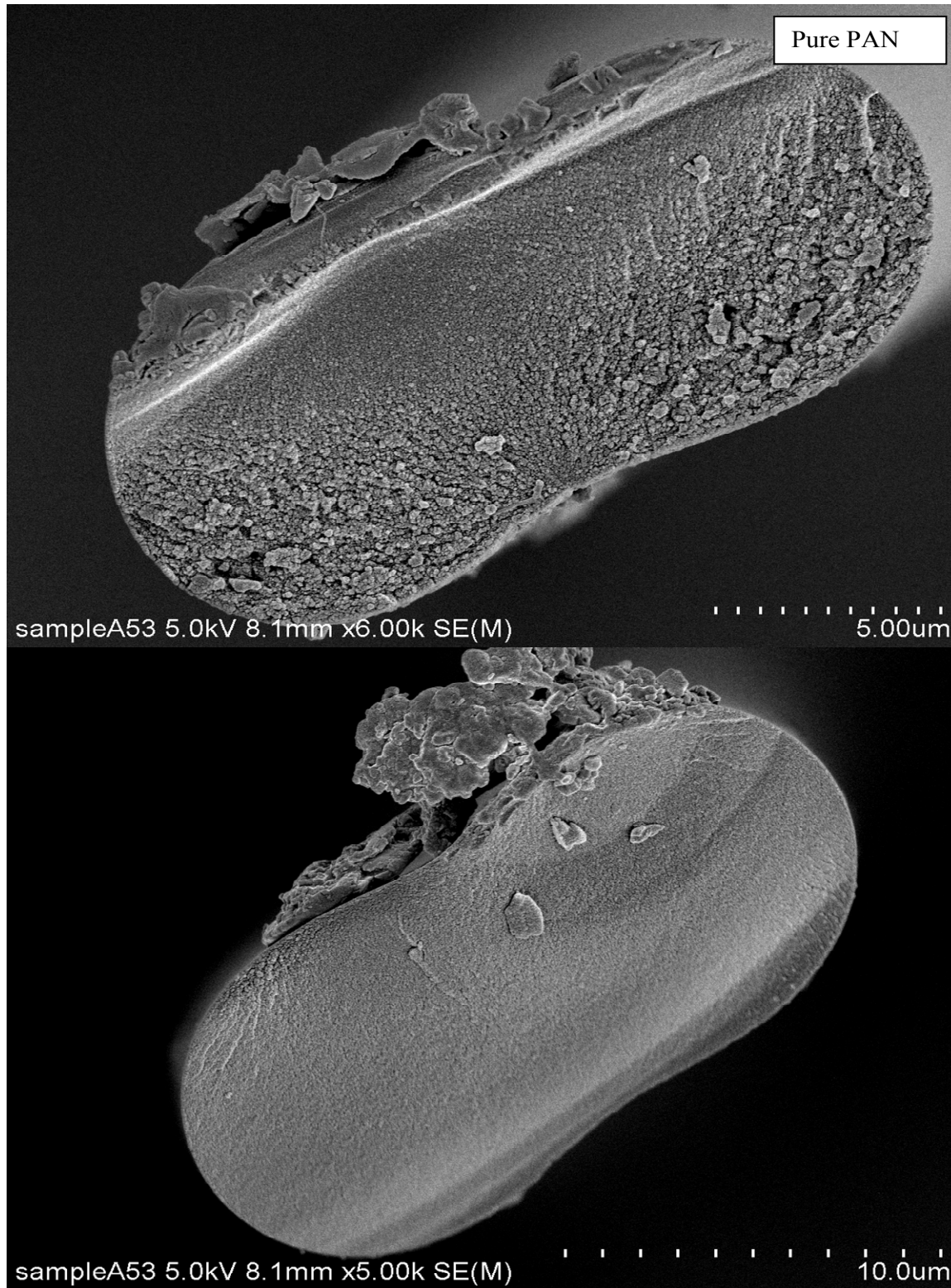
Figure B-1 Neat PAN-Based carbon fiber fracture surfaces (WSPIN 53A)
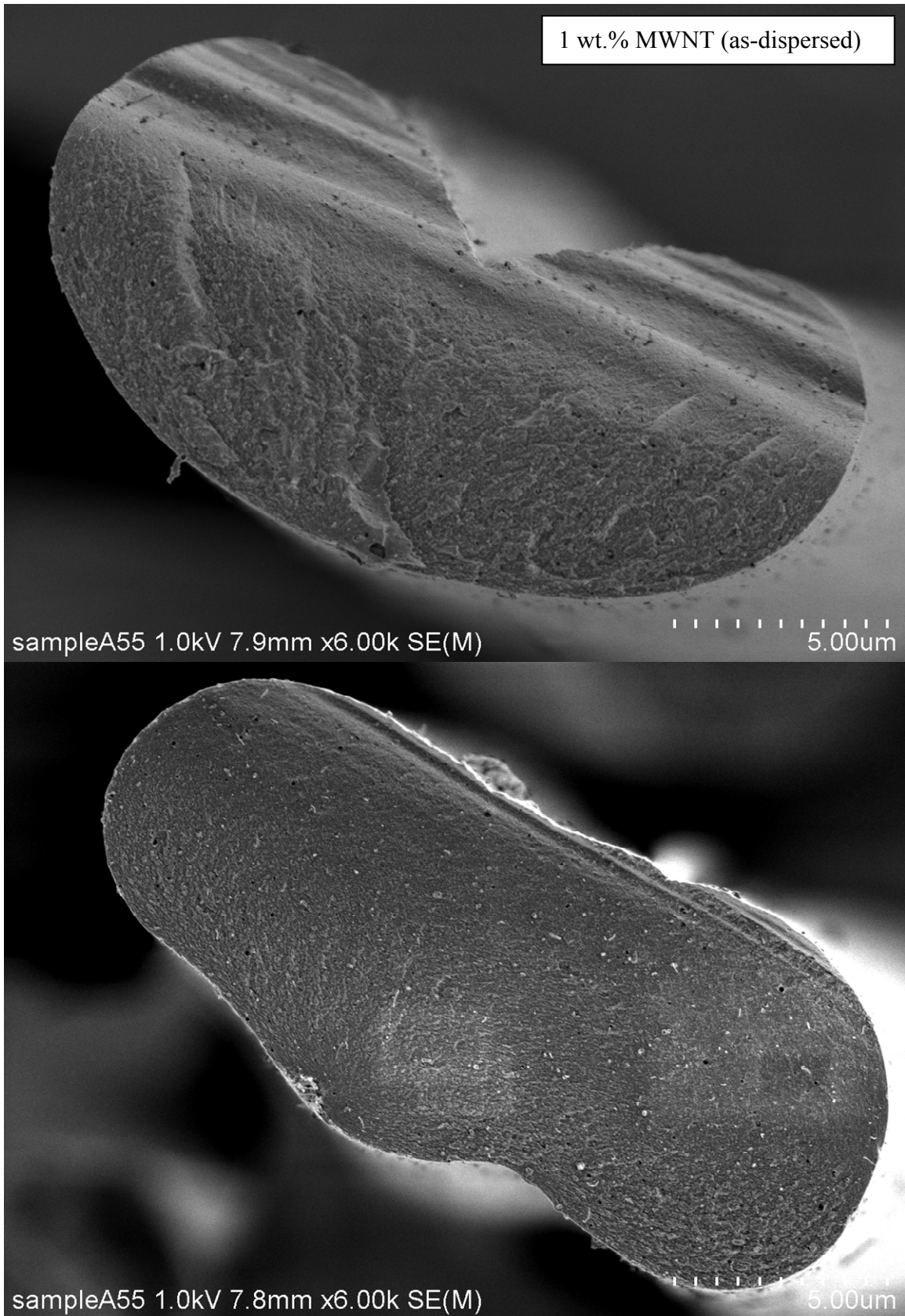
Figure B-2 1 wt% MWNT/PAN-Based carbon fiber fracture surfaces (WSPIN 55A)

sampleA56 5.0kV 8.3mm x5.00k SE(M)   10.0um

sampleA56 5.0kV 7.8mm x5.00k SE(M)   10.0um
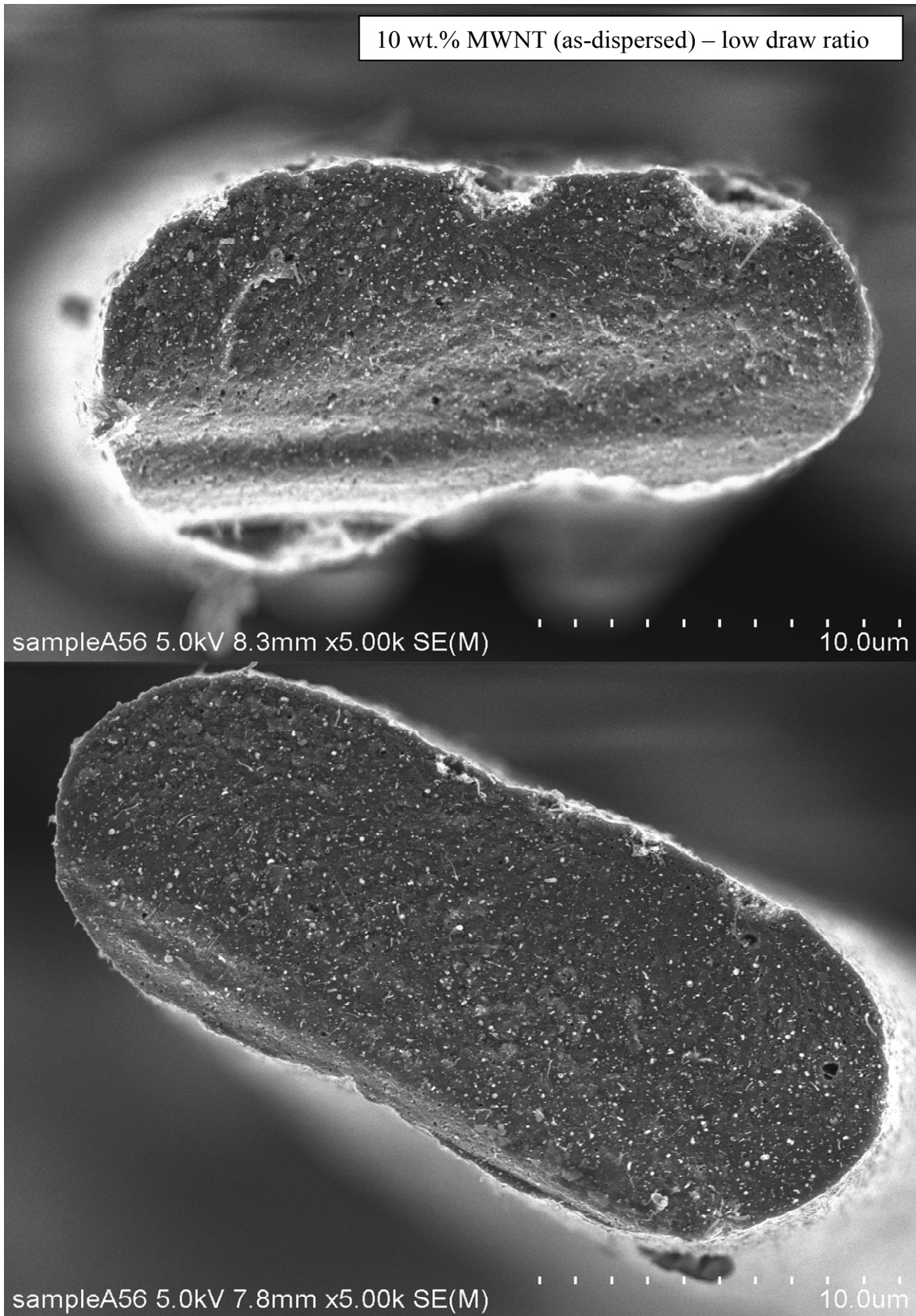
Figure B-3 10 wt% MWNT/PAN-Based carbon fiber fracture surfaces (WSPIN 56A)

10 wt.% MWNT (as-dispersed)

56B 5.0kV 8.8mm x5.00k SE(U)   10.0um

56B 5.0kV 8.4mm x4.50k SE(U)   10.0um
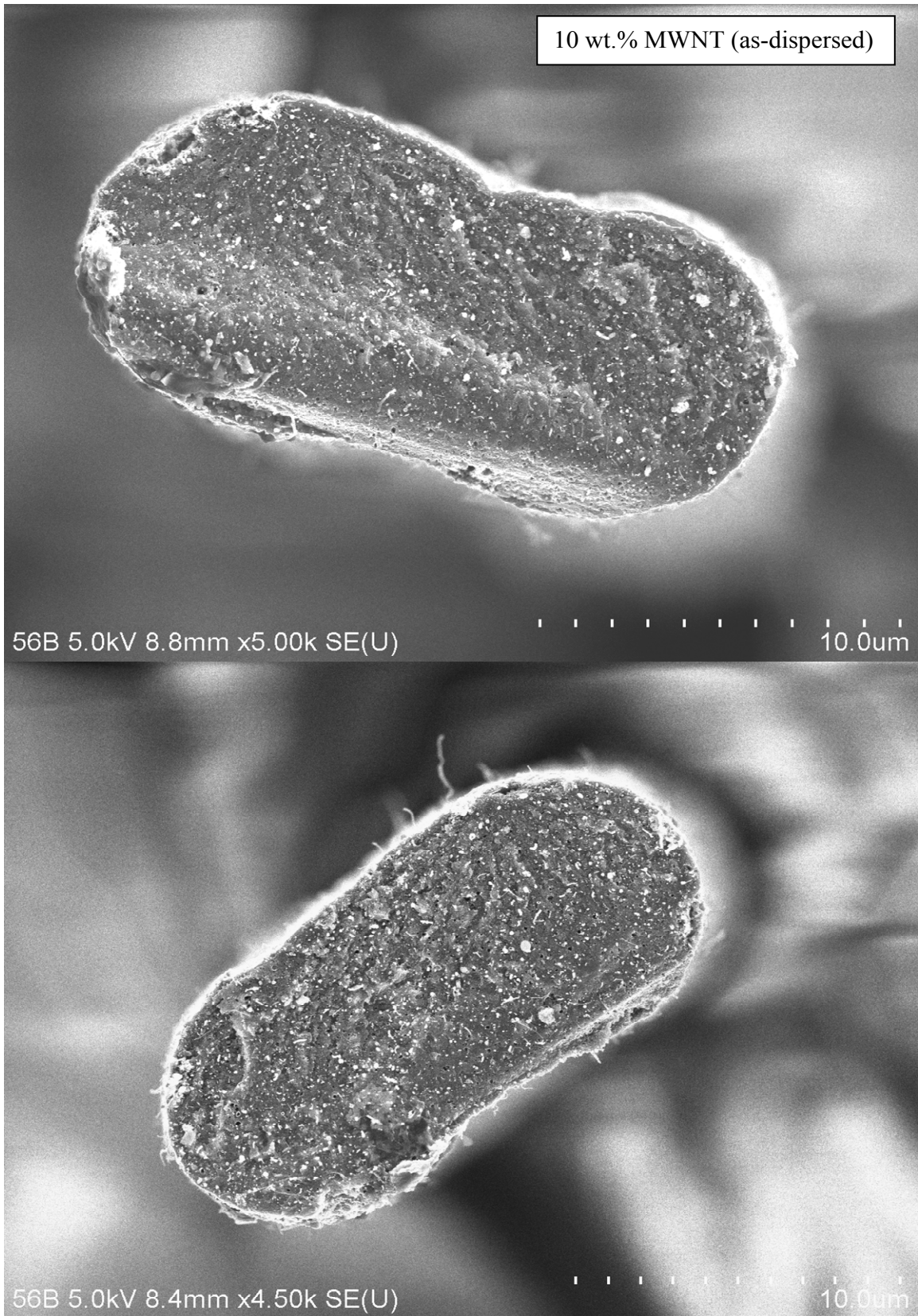
Figure B-4 10 wt% MWNT/PAN-Based carbon fiber fracture surfaces (WSPIN 56B)

10 wt.% MWNT
(dispersed from supernant)

57E 5.0k ... x4.00k SE(U)   10.0um

57E 5.0kV 9.0mm x4.00k SE(U)   10.0um
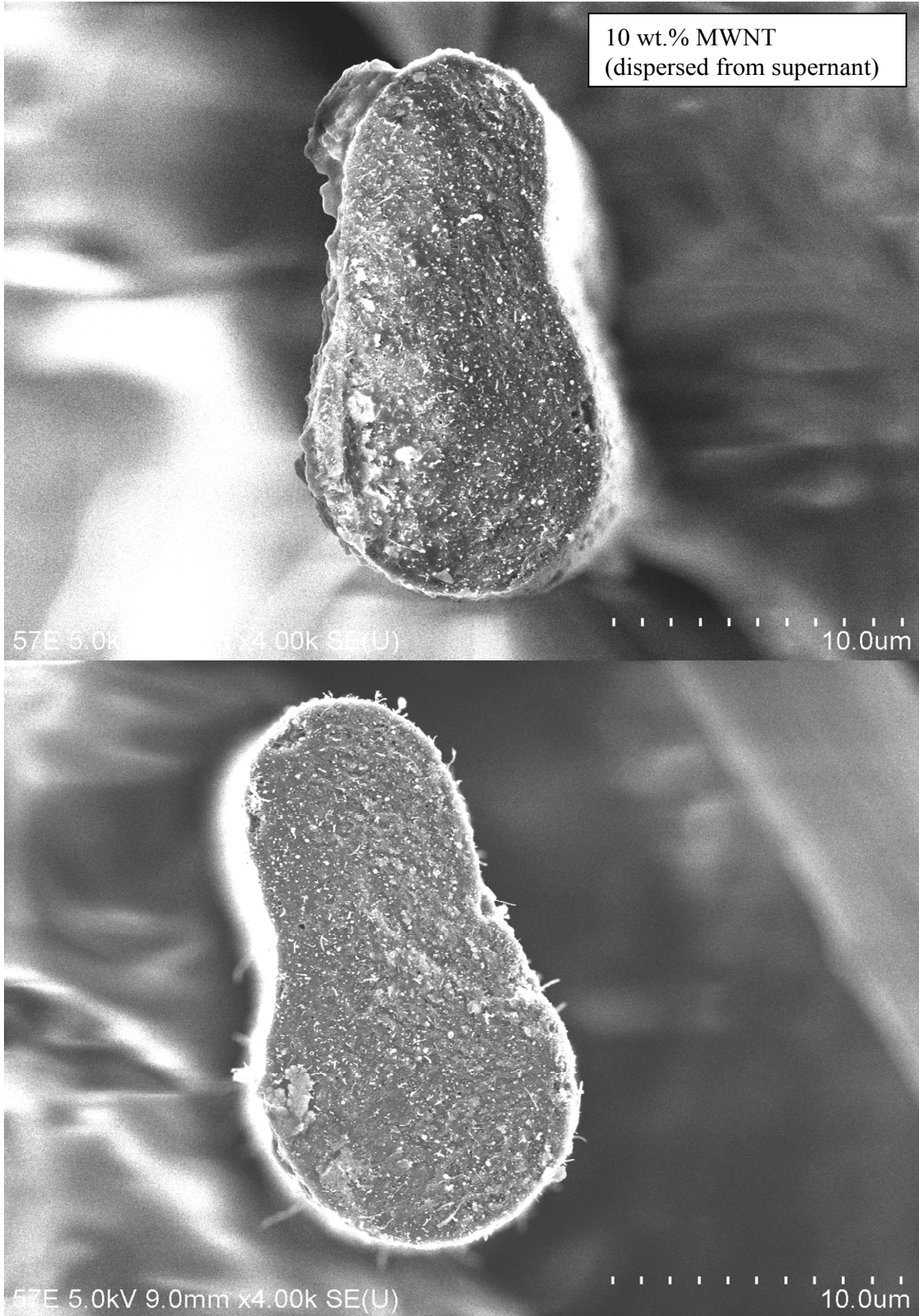
Figure B-5 10 wt% MWNT/PAN-Based carbon fiber fracture surfaces (WSPIN 57E)

10 wt.% MWNT
(dispersed from supernant)
(higher initial tension)

57C 5.0kV 9.1mm x3.00k SE(U)   10.0um

57C 5.0kV 9.1mm x4.50k SE(U)   10.0um

Figure B-6 10 wt% MWNT/PAN-Based carbon fiber fracture surfaces (WSPIN 57C)

APPENDIX C MWNT/PAN composite fiber tensile properties

WSPIN#	Initial Wt. % MWNTs	Total Draw Ratio	Initial Carbonization Tension (MPa)	Maximum Carbonization Tension (MPa)	Total Shrinkage (%)	Carbon Yield (%)	Equivalent Circular Diameter N=30 (μm)
53A	0.0	124			9.09	51.03	13.28 ± 1.36
55A	1.0 (as-dispersed)	124			8.00	50.64	12.93 ± 0.51
56B	10 (as-dispersed)	155			4.35	56.04	14.70 ± 1.38
57E	10 (supernatant)	129			5.88	54.60	14.11 ± 0.90
56A	10 (as-dispersed)	93			5.77	56.11	17.02 ± 1.73
57C	10 (supernatant)	124			5.77	56.42	14.15 ± 1.01

Figure C-1 Processing parameters and fiber tow identification

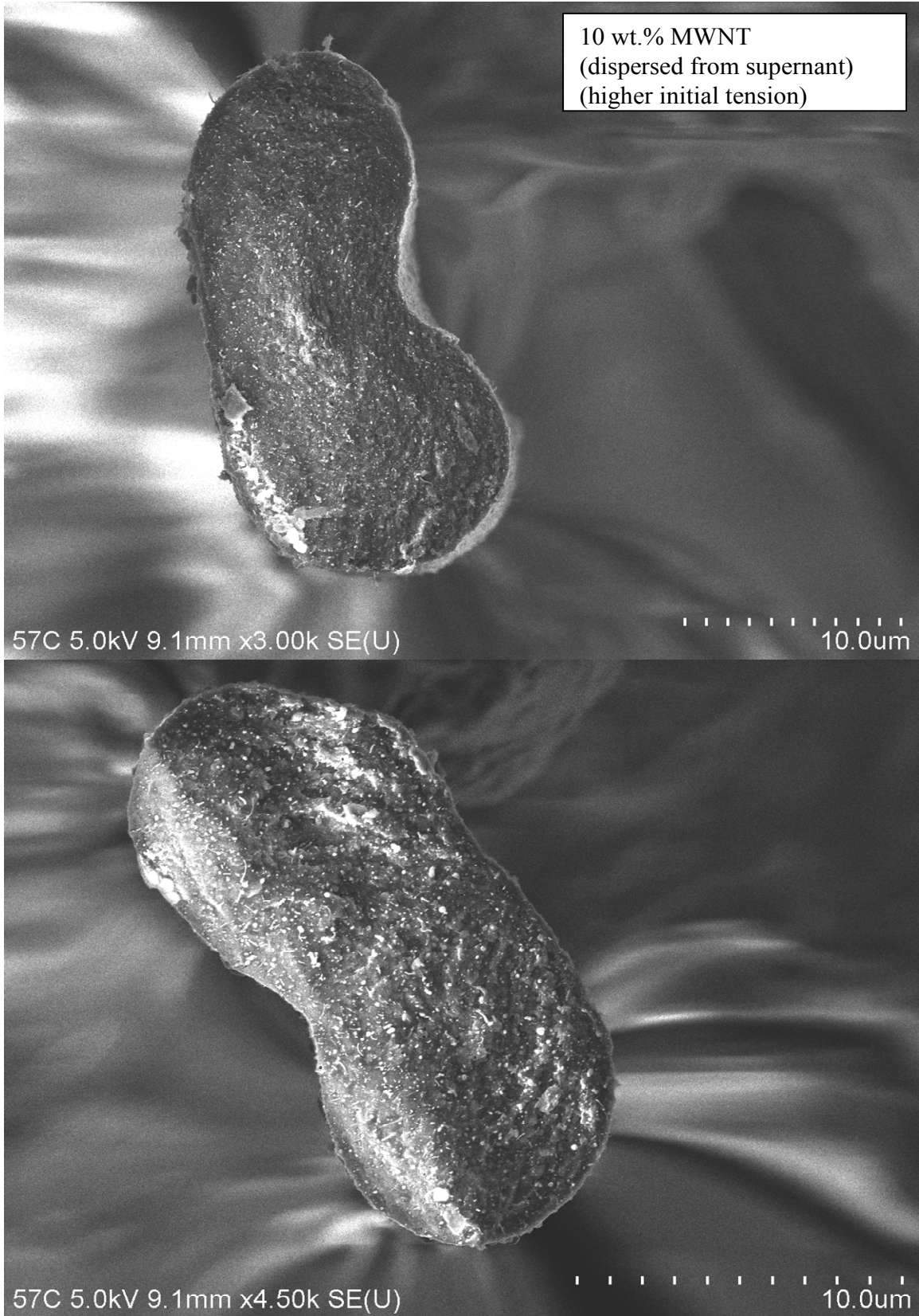| Fiber	Measured Modulus GPa	True Modulus GPa	Break Stress MPa	Strain At Break (m/m)	Strain Energy MJ/m³	
53A	240.2	341.6	1375.5	0.411%	2.90	ave
	37.1	57.2	275.5	0.092%	1.08	stdev
	23	23	23	23	23	N
	15.1	23.4	112.6	0.038%	0.44	95% conf
55A	247.1	305.3	1262.5	0.413%	2.77	ave
	18.0	11.5	330.1	0.105%	1.28	stdev
	28	28	28	28	28	N
	6.7	4.2	122.3	0.039%	0.48	95% conf
56B	171.2	189.6	949.3	0.500%	2.49	ave
	14.2	16.0	233.2	0.111%	1.13	stdev
	29	29	29	29	29	N
	5.2	5.8	84.9	0.040%	0.41	95% conf
56A	181.3	208.0	1049.0	0.509%	2.77	ave
	33.8	44.8	291.3	0.109%	1.18	stdev
	35	35	35	35	35	N
	11.2	14.8	96.5	0.036%	0.39	95% conf
57E	167.9	196.9	895.9	0.455%	2.07	ave
	18.3	21.8	159.7	0.062%	0.61	stdev
	29	29	29	29	29	N
	6.7	7.9	58.1	0.022%	0.22	95% conf
57C	201.0	207.4	1192.5	0.577%	3.56	ave
	30.2	31.7	274.5	0.109%	1.38	stdev
	26	26	26	26	26	N
	11.6	12.2	105.5	0.042%	0.53	95% conf

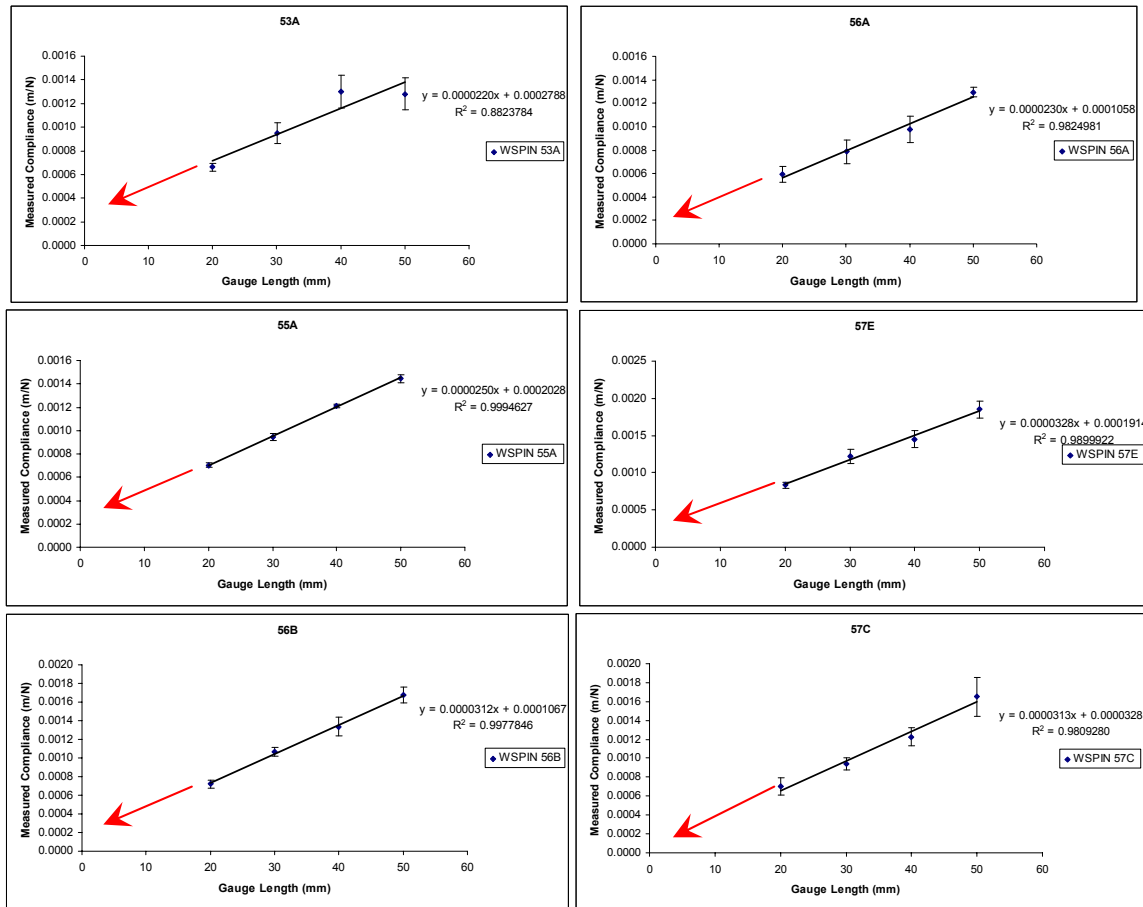Figure C-2 Average fiber tensile results

Figure C-3 System compliance calculation for each of the investigated fiber tows

Measuring the actual strain in the fiber gauge length during tensile testing is impossible using conventional strain gauges because they can not be attached without degrading the tensile properties of the fiber. The cross-head displacement is thus measured as a psueo-strain, but entails both displacements in the fiber plus the displacement in the load cell used to measure the tensile force during testing. Other displacements, albeit less important, such as those in the glue used to mount the fiber, etc., are also included in the total displacement measured by the cross-head. Therefore, in total, a "system" displacement is measured by the cross-head. All things being equal during testing (load cell, glue, mounts, etc.) as the gauge length of the fiber is increased, the overall contribution of displacement by the fiber to total displacement is larger. Here the system can be view as two springs in series, one is the sytem (load cell + glue etc.), and the other is the fiber gauge length. The total spring constant of the system, k_{sys}, can then be calculated knowing the overall force vs. displacement curve. By plotting $1/k_{sys}$ vs fiber gauge length, and extrapolating to zero gauge length, the compliance of the system can be accurately determined, and thus its displacement contribution can be subtracted from the total displacement to reflect the actual fiber displacement. This is the system compliance correction which enables the true modulus of the fiber to be determined, and is shown above in Figure C-3.

REFERENCES

[1]   S. Iijima, *NATURE* **1991**, *354*, 56.
[2]   A. Oberlin, M. Endo, T. Koyama, *Carbon* **1976**, *14*, 133.
[3]   S. B. Sinnott, R. Andrews, *Critical Reviews in Solid State and Materials Science* **2001**, *26*, 145.
[4]   P. Lambin, *Comptes Rendus Physique* **2003**, *4*, 1009.
[5]   K. Kaneto, M. Tsuruta, G. Sakai, W. Y. Cho, Y. Ando, *Synthetic Metals* **1999**, *103*, 2543.
[6]   S. Berber, Y. K. Kwon, D. Tomanek, *Physical Review Letters* **2000**, *84*, 4613.
[7]   P. Kim, L. Shi, A. Majamdar, P. L. McEuen, *Physical Review Letters* **2001**, *87*, 215502.
[8]   R. Saito, G. Dresselhaus, M. S. Dresselhaus, *Physical Properties of Carbon Nanotubes*, Imperial College Press, London **1998**.
[9]   J.-P. Salvetat-Delmotte, A. Rubio, *CARBON* **2001**, *40*, 1729.
[10]   A. Thess, R. Lee, P. Nikolaev, H. Dai, P. Petit, J. Robert, C. Xu, Y. H. Lee, S. G. Kim, A. G. Rinzler, D. T. Colbert, G. E. Scuseria, D. Tomanek, J. E. Fischer, R. E. Smalley, *Science* **1996**, *273*, 483.
[11]   R. Andrews, D. Jacques, D. Qian, T. Rantell, *Accounts of Chemical Research* **2002**, *35*, 1008.
[12]   J.-B. Donnet, T. K. Wang, J. C. M. Peng, S. Rebouillat, Eds., *Carbon Fibers Third Edition, Revised and Expanded*, Marcel Dekker Inc., New York **1998**.
[13]   Y. Zhang, H. Gu, S. Lijima, *Applied Physics Letters* **1998**, *73*, 3827.
[14]   R. Andrews, D. Jacques, A. M. Rao, F. Derbyshire, D. Qian, X. Fan, E. C. Dickey, J. Chen, *Chemical Physics Letters* **1999**, *303*, 467.
[15]   A. Krishnan, E. Dujardin, T. W. Ebbesen, P. N. Yianilos, M. M. J. Treacy, *Physical Review B* **1998**, *58*, 14013.
[16]   G. V. Lier, C. V. Alsenoy, V. V. Doren, P. Geerlings, *Chemical Physics Letters* **2000**, *326*, 181.
[17]   L. S. Schadler, S. C. Giannaris, P. M. Ajayan, *Applied Physics Letters* **1998**, *73*, 3842.
[18]   M.-F. Yu, B. S. Files, S. Arepalli, R. S. Ruoff, *Physical Review Letters* **2000**, *84*, 5552.
[19]   M. B. Nardelli, B. I. Yakobson, J. Bernholc, *Physical Review Letters* **1998**, *81*, 4656.
[20]   E. Munoz, D.-S. Suh, S. Collins, M. Selvidge, G. Ussery, A. G. Rinzler, M. T. Martinez, R. H. Baughman, *Advance Materials* **2005**, *17*, 1064.
[21]   C.-W. Nan, G. Liu, Y. Lin, M. Li, *Applied Physics Letters* **2004**, *85*, 3549.
[22]   D. A. Walters, L. M. Ericson, M. J. Casavant, J. Liu, D. T. Colbert, K. A. Smith, R. E. Smalley, *Applied Physics Letters* **1999**, *74*, 3803.
[23]   M. M. J. Treacy, T. W. Ebbesen, J. M. Gibson, *Nature* **1996**, *381*, 678
[24]   M.-F. Yu, O. Lourie, M. J. Dyer, K. Moloni, T. F. Kelly, R. Ruoff, *Science* **2000**, *287*, 637.
[25]   B. G. Demczyk, Y. M. Wang, J. Cumings, M. Hetman, W. Han, A. Zettl, R. O. Ritchie, *Materials Science & Engineering* **2002**, *A334*, 173.
[26]   H. D. Wagner, A. H. Barber, R. Andrews, L. S. Schadler, *Applied Physics Letters* **2005**, *87*, 203106.
[27]   H. D. Wagner, O. Lourie, Y. Feldman, R. Tenne, *Applied Physics Letters* **1998**, *72*, 188.
[28]   Y. J. Kim, T. S. Shin, H. d. Choi, J. H. Kwon, Y.-C. Chung, H. G. Yoon, *Carbon* **2005**, *43*, 23.
[29]   M. H. G. Wichmann, J. Sumfleth, B. Fiedler, F. H. Goyny, K. Schuttle, *Mechanics of Composite Materials* **2006**, *42*, 395.
[30]   A. Moisala, Q.Li, I. A. Kinloch, A. H. Windle, *Composites Science and Technology* **2006**, *66*, 1285.
[31]   T. Y. Choi, D. Poulikakos, J. Tharian, U. Sennhauser, *Applied Physics Letters* **2005**, *87*, 013108.
[32]   J. Sandler, A. H. Windle, P. Werner, V. Altstadt, M. V. Es, M. S. P. Shaffer, *Journal of Materials Science* **2003**, *38*, 2135.
[33]   A. Sciences, Vol. 2005, **2005**.
[34]   R. Bacon, *Journal of Applied Physics* **1960**, *31*, 283.
[35]   F. Deng, Q.-S. Zheng, L.-F. Wang, C.-W. Nan, *Applied Physics Letters* **2007**, 021914.
[36]   Hexcel, Vol. 2005, **2005**.
[37]   Toray, Vol. 2005, **2005**.
[38]   Cytec, **2007**.
[39]   M. Cadek, J. N. Coleman, K. P. Ryan, v. Nicolosi, G. Bister, A. Fonseca, J. B. Nagy, K. Szostak, F. Beguin, W. J. Blau, *Nano Letters* **2004**, *4*, 353.

[40]   M. Cadek, J. N. Coleman, D. Blond, A. Fonseca, J. B. Nagy, K. Szostak, F. Beguin, W. J. Blau, "Effect of Nanotube Type on the Enhancement of Mechanical Properties of Free-Standing Polymer/Nanotube Composite Films", presented at *Molecular Nanostructures: XVII Int'l. Winterschool/Euroconference on Electronic Properties of Novel Materials*, **2003**.

[41]   J. N. Coleman, U. Khan, Y. K. Gun'ko, *Advance Materials* **2006**, *18*, 689.

[42]   E. J. Siochi, D. C. Working, C. Park, P. T. Lillehei, J. H. Rouse, C. C. Topping, A. R. Bhattacharyya, S. Kumar, *COMPOSITES Part B: engineering* **2004**, *35*, 439.

[43]   J. Zeng, B. Saltysiak, W. S. Johnson, D. A. Schiraldi, S. Kumar, *COMPOSITES Part B: engineering* **2004**, *35*, 173.

[44]   R. E. Gorga, R. E. Cohen, *Journal of Polymer Sciences: Part B: Polymer Physics* **2004**, *42*, 2690.

[45]   S. G. Advani, Z. Fan, "Effect of Dispersion State on the Rheology of Mulit-walled Carbon Nanotube Suspensions in Shear Flow", presented at *Materials Processing and Design: Modeling, Simulation, and Applications, NUMIFORM 2004*, **2004**.

[46]   M. S. P. Shaffer, X. Fan, A. H. Windle, *Carbon* **1998**, *36*, 1603.

[47]   M. S. P. Shaffer, A. H. Windle, *Macromolecules* **1999**, *32*, 6864.

[48]   J. Zeng, B. Saltysiak, W. S. Johnson, D. A. Schiraldi, S. Kumar, *Composites Part B: Engineering* **2004**, *35*, 173.

[49]   M. C. Weisenberger, E. A. Grulke, D. Jacques, T. Rantell, R. Andrews, *Journal of Nanoscience and Nanotechnology* **2003**, *3*, 535.

[50]   W. Ding, A. Eitan, F. T. Fisher, X. H. Chen, D. A. Dikin, R. Andrews, L. C. Brinson, L. S. Schadler, R. S. Ruoff, *Nano Letters* **2003**, *3*, 1593.

[51]   K. P. Ryan, M. Cadek, V. Nicolosi, D. Blond, M. Ruether, G. Armstrong, H. Swan, A. Fonseca, J. B. Nagy, W. K. Maser, W. J. Blau, J. N. Coleman, *Composites Science and Technology* **2007**, *67*, 1640.

[52]   G. L. Hwang, Y.-T. Shieh, K. C. Hwang, *Advanced Functional Materials* **2004**, *14*, 487.

[53]   D. McIntosh, V. N. Khabashesku, E. V. Barrera, *J.Phys.Chem. C* **2007**, *111*, 1592.

[54]   D. Blond, V. Barron, M. Ruether, K. P. Ryan, V. Nicolosi, W. J. Blau, J. N. Coleman, *Advance Materials* **2006**, *16*, 1608.

[55]   A. B. Dalton, S. Collins, E. Munoz, J. M. Razal, V. H. Ebron, J. P. Ferraris, J. N. Coleman, B. G. Kim, R. H. Baughman, *NATURE* **2003**, *423*, 703.

[56]   E. T. Thostenson, T.-W. Chou, *Carbon* **2006**, *44*, 3022.

[57]   F. H. Gojny, M. H. G. Wichmann, B. Fiedler, I. a. Kinloch, W. Bauhofer, A. H. windle, K. Schulte, *Polymer* **2006**, *47*, 2036.

[58]   F. T. Fisher, R. D. Bradshaw, L. C. Brinson, *Composites Science and Technology* **2003**, *63*, 1689.

[59]   K. P. Ryan, M. Cadek, V. Nicolosi, S. Walker, M. Ruether, A. Fonseca, J. B. Nagy, W. J. Blau, J. N. Coleman, *Synthetic Metals* **2006**, *156*, 332.

[60]   E. Hammel, X. Tang, M. Trampert, T. Schmitt, K. Mauthner, A. Eder, P. Potschke, *Carbon* **2004**, *42*, 1153.

[61]   S. Giordani, S. D. Begin, V. Nicolosi, S. Lebedkin, M. M. Kappes, W. J. Blau, J. N. Coleman, *Journal Physics Chemistry B* **2006**, *110*, 15708.

[62]   S. Giordani, S. Bergin, V. Nicolosi, S. Lebedkin, W. J. Blau, J. N. Coleman, *Physics Status Solidi* **2006**, *243*, 3058.

[63]   J. C. Kearns, R. L. Shambaugh, *Journal of Applied Polymer Science* **2002**, *86*, 2079.

[64]   F. J. Fuchs, "New Ultrasonic Technology Improves Cleaning and Prevents Surface Damage Due to Cavitation Erosion Effects", presented at *45th Annual Technical Conference of Society of Vacuum Coaters*, **2002**.

[65]   Y. Yang, E. A. Grulke, Z. G. Zhang, G. Wu, *Journal of Applied Physics* **2006**, *99*, 114307.

[66]   J. K. W. Sandler, S. Pegel, M. Cadek, F. Gojny, M. v. Es, J. Lohmar, W. J. Blau, K. Schulte, A. H. Windle, M. S. P. Shaffer, *Polymer* **2004**, *45*, 2001.

[67]   X. Gong, J. Liu, S. Baskaran, R. D. Voise, J. S. Young, *Chemistry of Materials* **2000**, *12*, 1049.

[68]   C. Velasco-Santos, A. L. Martinez-Hernandez, F. T. Fisher, R. S. Ruoff, V. M. Castano, *Journal of Physics D: Applied Physics* **2003**, *36*, 1423.

[69]   P. Poulin, B. Vigolo, P. Launois, *CARBON* **2002**, *40*, 1741.

[70]   C. Velasco-Santos, A. L. Martinez-Hernandez, F. T. Fisher, R. S. Ruoff, V. M. Castano, *Chemistry of Materials* **2003**, *15*, 4470.

[71]   R. Haggenmueller, H. H. Gommans, A. G. Rinzler, J. E. Fischer, K. I. Winey, *Chemical Physics Letters* **2000**, *330*, 219.

[72]   H. Bubert, S. Haiber, W. Brandl, G. Marginean, M. Heintze, V. Bruser, *Diamond and Related Materials* **2003**, *12*, 811.
[73]   B. Kim, W. M. Sigmund, *Langmuir* **2004**, *20*, 8239.
[74]   K. Esumi, A. Ishigami, A. Nakajima, K. Sawadi, H. Honda, *Carbon* **1996**, *34*, 279.
[75]   W. Chen, X. Tao, Y. Liu, *Composites Science and Technology* **2006**, 3029.
[76]   A. Eitan, K. Jiang, D. Dukes, R. Andrews, L. S. Schadler, *Chemistry of Materials* **2003**, *15*, 3195.
[77]   L. Valentini, I. Armentano, D. Puglia, J. M. Kenny, *Carbon* **2004**, *42*, 323.
[78]   J. Shen, W. Huang, L. Wu, Y. Hu, M. Ye, *Composites Part A: applied science and manufacturing* **2007**, *38*, 1331.
[79]   L. Liu, H. D. Wagner, *Composites Science and Technology* **2005**, *65*, 1861.
[80]   C. A. Kyke, M. P. Stewart, F. Maya, J. M. Tour, *Synlett* **2004**, *1*, 155.
[81]   M. Holzinger, O. Vostrowsky, A. Hirsch, F. Henrich, M. Kappes, R. Weiss, F. Jellen, *Angewandte Chemie, International, Ed.* **2001**, *40*, 4002.
[82]   M. J. Moghaddam, S. Taylor, M. Gao, S. Huang, L. Dai, M. J. McCall, *Nano Letters* **2004**, *4*, 89.
[83]   D. Pantarotto, C. D. Partidos, R. Graff, J. Hoebeke, J. P. Briand, M. Prato, A. Bianco, *Journal of the American Chemical Society* **2003**, *125*, 6160.
[84]   C. A. Dyke, J. M. Tour, *Journal of the American Chemical Society* **2003**, *125*, 1156.
[85]   K. Lozano, S. Yang, R. E. Jones, *Carbon* **2004**, *42*, 2329.
[86]   Z. Jin, K. P. Pramoda, G. Xu, S. H. Goh, *Chemical Physics Letters* **2001**, *337*, 43.
[87]   T. Kashiwagi, E. Grulke, J. Hilding, R. Harris, W. Awad, J. Douglas, *Macromolecules Rapid Communications* **2002**, *23*, 761.
[88]   L. Jin, C. Bower, O. Zhou, *Applied Physics Letters* **1998**, *73*, 1197.
[89]   M. S. P. Shaffer, A. H. Windle, *Advanced Materials* **1999**, *11*, 937.
[90]   S. L. Ruan, P. Gao, X. G. Yang, T. X. Yu, *Polymer* **2003**, *44*, 5643.
[91]   P. M. Ajayan, O. Stephan, C. Colliex, D. Traught, *SCIENCE* **1994**, *265*, 1212.
[92]   J. N. Coleman, M. Cadek, R. Blake, V. Nicolosi, K. P. Ryan, C. Belton, A. Fonseca, J. B. Nagy, Y. K. Gun'ko, W. J. Blau, *Advanced Functional Materials* **2004**, *14*, 791.
[93]   K. P. Ryan, S. M. Lipson, A. Drury, M. Cadek, M. Ruether, S. M. O'Flaherty, V. Barron, B. McCarthy, H. J. Byrne, W. J. Blau, J. N. Coleman, *Chemical Physics Letters* **2004**, *391*, 329.
[94]   M. Cadek, J. N. Coleman, V. Barron, K. Hedicke, W. J. Blau, *Applied Physics Letters* **2002**, *81*, 5123.
[95]   C. Stephan, T. P. Nguyen, M. Lamy de la Chapelle, S. Lefrant, C. Journet, P. Bernier, *Synthetic Metals* **2000**, *108*, 139.
[96]   E. Assouline, A. Lustiger, A. H. Barber, C. A. Cooper, E. Klein, E. Wachtel, H. D. Wagner, *Journal of Polymer Sciences: Part B: Polymer Physics* **2003**, *41*, 520.
[97]   E. T. Thostenson, T.-W. Chou, *Journal of Physics D: Applied Physics* **2002**, *35*, L77.
[98]   O. Lourie, D. M. Cox, H. D. Wagner, *Physical Review Letters* **1998**, *81*, 1638.
[99]   G. Tibbetts, J. J. McHugh, *Journal of Materials Research* **1999**, *14*, 2871.
[100]   F. Du, C. Guthy, T. Kashiwagi, J. E. Fischer, K. I. Winey, *Journal of Polymer Science: Part B: Polymer Physics* **2006**, *44*, 1513.
[101]   N. Koratkar, B. Wei, P. Ajayan, *Advanced Materials* **2002**, *14*, 997.
[102]   N. A. Koratkar, B. Wei, P. M. Ajayan, *Composites Science and Technology* **2003**, *63*, 1525.
[103]   E. Lahiff, R. Leahy, J. N. Coleman, W. J. Blau, *Carbon* **2005**, *44*, 1525.
[104]   J. N. Coleman, W. J. Blau, A. B. Dalton, E. Munoz, S. Collins, B. G. Kim, J. M. Razal, M. Selvidge, G. Vieiro, R. H. Baughman, *Applied Physics Letters* **2003**, *82*, 1682.
[105]   Z. J. Z. Wang, C. Xu, J. Liang, B. Wei, D. Wu, S. Zhu, *Materials Science & Engineering* **1999**, *A271*, 395.
[106]   P. M. Ajayan, *Advanced Materials* **1995**, *7*, 489.
[107]   E. M. Moore, D. L. Ortiz, V. T. Marla, R. L. Shambaugh, B. P. Grady, *Journal of Applied Polymer Science* **2004**, *93*, 2926.
[108]   S. Kumar, H. Doshi, M. Srinivasarao, J. O. Park, D. A. Schiraldi, *Polymer* **2002**, *43*, 1701.
[109]   B. Vigolo, P. Poulin, M. Lucas, P. Luanois, P. Bernier, *Applied Physics Letters* **2002**, *81*, 1210.
[110]   J. N. Barisci, M. Tahhan, G. G. Wallace, S. Badaire, T. Vaugien, M. Maugey, P. Poulin, *Advanced Functional Materials* **2004**, *12*, 133.
[111]   P. Miauder, S. Badaire, M. Maugey, A. Derre, V. Pichot, P. Launois, P. Poulin, C. Zakri, *Nano Letters* **2005**, *5*, 2212.

[112]   T. V. Sreekumar, T. Liu, B. G. Min, H. Guo, S. Kumar, R. H. Hauge, R. E. Smalley, *Advanced Materials* **2004**, *16*, 58.
[113]   H. G. Chae, M. L. Minus, A. Rasheed, S. Kumar, *Polymer* **2007**, *48*, 3781.
[114]   S. Kumar, H. Chae, T. V. Sreekumar, T. Uchida, *Polymer* **2005**, *46*, 10925.
[115]   Z. Hao, Z. Wang, Z. Zhang, J. Wu, J. Zhang, J. He, *Advance Materials* **2007**, *19*, 698.
[116]   S. Ruan, P. Gao, T. X. Yu, *Polymer* **2006**, *47*, 1604.
[117]   S. Kumar, T. D. Dang, F. E. Arnold, A. R. Bhattacharyya, B. G. Min, X. Zhang, R. A. Vaia, C. Park, W. W. Adams, R. H. Hauge, R. E. Smalley, S. Ramesh, P. A. Willis, *Macromolecules* **2002**, *35*, 9039.
[118]   B. Ding, H. Y. Kim, S. C. Lee, D. R. Lee, K. J. Choi, *Fibers and Polymers* **2002**, *3*, 73.
[119]   F. Ko, Y. Gogotsi, A. Ali, N. Naguib, H. Ye, G. Yang, C. Li, P. Willis, *Advanced Materials* **2003**, *15*, 1161.
[120]   C. Seoul, Y.-T. Kim, C.-K. Berk, *Journal of Polymer Sciences: Part B: Polymer Chemistry* **2003**, *41*, 1572.
[121]   M. Motta, Y.-L. Li, I. Kinloch, A. Windle, *Nano Letters* **2005**, *5*, 1529.
[122]   M. E. Kozlov, R. C. Capps, W. M. Sampson, V. H. Ebron, J. P. Ferraris, R. H. Baughman, *Advance Materials* **2005**, *17*, 614.
[123]   X. Zhang, Q. Li, Y. Tu, Y. Li, J. Y. Coulter, L. Zheng, Y. Zhao, Q. Jia, D. E. Peterson, Y. Zhu, *Small* **2007**, *3*, 244.
[124]   M. Lucas, B. Vigolo, S. Badaire, D. L. Bolloc'h, A. Marucci, D. Durand, M. Hampton, C. Zakri, P. Poulin, P. Launois, "Alignment of Carbon Nanotubes in Macroscopic Fibers", presented at *Structural and Electronic Properties of Molecular Nanostructures*, **2002**.
[125]   C. Bower, R. Rosen, L. Jin, J. Han, O. Zhou, *Applied Physics Letters* **1999**, *74*, 33173319.
[126]   H. H. Chuah, B. T. A. Chang, *Polymer Bulletin* **2001**, *46*, 307.
[127]   D. Fischer, P. Potschke, H. Brunig, A. Janke, *Macromol Symp* **2005**, *230*, 167.
[128]   P. M. Ajayan, L. S. Schadler, C. Giannaris, A. Rubio, *Advanced Materials* **2000**, *12*, 750.
[129]   C. A. Cooper, R. J. Young, M. Halsall, *COMPOSITES Part A: Applied science and manufacturing* **2001**, *32*, 401.
[130]   E. K. Hobbie, H. Wang, H. Kim, S. Lin-Gibson, E. A. Grulke, *Physics of Fluids* **2003**, *15*, 1196.
[131]   S. Lin-Gibson, J. A. Pathak, E. A. Grulke, H. Wang, E. K. Hobbie, *Physical Review Letters* **2004**, *92*, 0483021.
[132]   A. B. Dalton, S. Collins, J. Razal, E. Munoz, V. H. Ebron, B. G. Kim, J. N. Coleman, J. P. Farraris, R. H. Baughman, *Journal of Materials Chemistry* **2004**, *14*, 1.
[133]   P. Miaudet, S. Badaire, M. Maugey, A. Derre, V. Pichot, P. Launois, P. Poulin, C. Zakri, *Nano Letters* **2005**, *5*, 2212.
[134]   R. Blake, J. N. Coleman, M. T. Byrne, J. E. McCarthy, T. S. Perova, W. J. Blau, A. Fonseca, J. B. Nagy, Y. K. G. ko, *The Royal Society of Chemistry 2006* **2006**, *16*, 4206.
[135]   B. Wang, H. Wang, B. Hong, Y. Zhang, *Polymer* **2005**, *37*, 376.
[136]   M. V. Jose, D. Dean, J. Tyner, G. Price, E. Nyairo, *Journal of Applied Polymer Science* **2007**, *103*, 3844.
[137]   S. Singh, Y. Pei, R. Miller, P. R. Sundararajan, *Advanced Functional Materials* **2003**, *13*, 868.
[138]   J. N. Coleman, M. Cadek, K. P. Ryan, A. Fonseca, J. B. Nagy, W. J. Blau, M. S. Ferreira, *Polymer* **2006**, *47*, 8556.
[139]   F. Ko, Y. Haihui, H. Lam, N. Titchenal, Y. Gogotsi, *Applied Physics Letters* **2004**, *85*, 1775.
[140]   D. Qian, C. Dickey, R. Andrews, T. Rantell, *Applied Physics Letters* **2000**, *76*, 1.
[141]   O. Lourie, H. D. Wagner, *Applied Physics Letters* **1998**, *73*, 3527.
[142]   B. Marrs, R. Andrews, D. Pienkowski, T. Rantell, "Mulitwall Carbon Nanotubes Enhance the Fatigue Life of Bone Cement", presented at *Orthopaedic Research Society*, San Francisco, March 7-10, **2004**.
[143]   B. Marrs, R. Andrews, D. Pienkowski, *Carbon* **2007**, *45*, 2098.
[144]   W. Zhang, A. Joshi, Z. Wang, R. S. Kane, N. Koratkar, *Nanotechnology* **2007**, *18*, 185703.
[145]   J. Yang, Z. Zhang, K. Friedrich, A. K. Schlarb, *Communications* **2007**, *28*, 955.
[146]   J. K. W. Sandler, S. Pegel, M. Cadek, F. Gojny, M. v. Es, J. Lohmar, W. J. Blau, K. Schulte, A. H. Windle, M. S. P. Shaffer, *Polymer* **2004**, *45*, 2001.
[147]   P. K. Mallick, *Fiber Reinforced Composites: Materials, Manufacturing, and Design*, Marcel Dekker, Inc., New York **1993**.

[148]   H. L. Cox, *British Journal of Applied Physics* **1952**, *3*, 72.
[149]   R. D. Bradshaw, F. T. Fisher, L. C. Brinson, *Composites Science and Technology* **2003**, *63*, 1705.
[150]   L. Berhan, Y. B. Li, A. M. Sastry, *Journal of Applied Physics* **2004**, *95*, 5027.
[151]   Y. B. Yi, L. Berhan, A. M. Sastry, *Journal of Applied Physics* **2004**, *96*, 1318.
[152]   E. T. Thostenson, T.-W. Chou, *Journal of Physics D: Applied Physics* **2003**, *36*, 573.
[153]   A. H. Barber, S. R. Cohen, H. D. Wagner, *Applied Physics Letters* **2003**, *82*, 4140.
[154]   K. A. Narh, L. Zhu, *Polymer International* **2004**, *53*, 1461.
[155]   J. Hilding, E. A. Grulke, Z. G. Zhang, F. Lockwood, *Journal of Dispersion Science and Technology* **2003**, *24*, 1.
[156]   A. Wall, J. N. Coleman, M. S. Ferreira, *The American Physical Society* **2004**, *B*, 125421.
[157]   F. Lux, *Journal of Materials Science* **1993**, *28*, 285.
[158]   J. Z. Kovacs, B. S. Velagala, K. Schulte, W. Bauhofer, *Composites Science and Technology* **2007**, *67*, 922.
[159]   C. A. Martin, J. K. W. Sandler, M. S. P. Shaffer, M. K. Schwarz, W. Bauhofer, K. Schulte, A. H. Windle, *Composites Science and Technology* **2004**, *64*, 2309.
[160]   H. M. Kim, M.-S. Choi, J. Joo, *Physical Review B* **2006**, *74*, 054201.
[161]   R. Ou, S. Gupta, C. A. Parker, R. a. Gerhardt, *Journal Physics Chemistry B* **2006**, *110*, 22365.
[162]   M. T. Connor, S. Roy, T. a. Ezquerra, F. J. B. Calleja, *Physical Review B* **1998**, *57*, 2286.
[163]   C. Guthy, F. Du, S. Brand, J. E. Fischer, K. I. Winey, *Mater.Res.Soc.Symp.Proc.* **2005**, *858E*, HH3.31.1.
[164]   Y. A. Kim, S. Kamio, T. Tajiri, T. Hayashi, S. M. Song, M. Endo, M. Terrones, M. S. Dresselhaus, *Applied Physics Letters* **2007**, *90*, 093125.
[165]   M. J. Biercuk, M. C. Llaguno, M. Radosvljevic, J. K. Hyun, A. T. Johnson, *Applied Physics Letters* **2002**, *80*.
[166]   M. B. Bryning, D. E. Milkie, M. F. Islam, J. M. Kikkawa, A. G. Yodh, *Applied Physics Letters* **2005**, *87*, 161909.
[167]   S. T. Huxtable, D. G. Cahill, S. Shenogin, L. Xue, R. Ozisik, P. Barone, M. Usrey, M. S. Strano, G. Siddons, M. Shim, P. Keblinski, *Nature Materials* **2003**, *2*, 731.
[168]   S. Shaikh, K. Lafdi, E. Silverman, *Carbon* **2007**, *45*, 695.
[169]   Q. Ngo, B. A. Cruden, A. M. Cassell, M. D. Walker, Q. Ye, J. E. Koehne, M. Meyyappan, J. Li, C. Y. Yang, *Mat.Res.Soc.Sym.Proc.* **2004**, *812*, F3.18.1.
[170]   A. Oberlin, M. Endo, T. Koyama, *Carbon* **1976**, *14*, 133.
[171]   Toray, Vol. 2005, **2007**.
[172]   R. Andrews, D. Jacques, D. Qian, E. C. Dickey, *CARBON* **2001**, *39*, 1681.
[173]   R. Andrews, D. Jacques, A. M. Rao, T. Rantell, F. Derbyshire, Y. Chen, J. Chen, R. C. Haddon, *Applied Physics Letters* **1999**, *75*, 1329.
[174]   D. D. L. Chung, *Carbon Fiber Composites*, Butterworth-Heinemann, Newton **1994**.
[175]   R. J. Zaldivar, G. S. Rellick, J. M. Yang, *Journal of Materials Research* **1993**, *8*, 501.
[176]   R. J. Zaldivar, G. S. Rellick, J. M. Yang, *Journal of Materials Research* **1995**, *10*, 609.
[177]   J. Brandup, E. H. Immergut, E. A. Grulke, Eds., *Polymer Handbook*, John Wiley & Sons Inc., New York **1999**.
[178]   S. Suresh, *Fatigue of Materials*, Cambridge University Press, Cambridge **1998**.
[179]   B. Marrs, *Journal of Biomedical Materials Research Part A* **2006**, *77*, 269.
[180]   S. Janna, D. P. Dwiggins, G. Lewis, *Bio-Medical Materials and Engineering* **2005**, *15*, 349.
[181]   A. Koganemaru, Y. Bin, Y. Agari, M. Matsuo, *Advanced Functional Materials* **2004**, *14*, 842.
[182]   N. Li, Y. Huang, F. Du, X. He, X. Lin, H. Gao, Y. Ma, F. Li, Y. Chen, P. C. Eklund, *Nano Letters* **2006**, *6*, 1141.

VITA

Matthew Collins Weisenberger
Born January13, 1977, Versailles, KY

EDUCATION

Master of Science, Materials Science and Engineering, University of Kentucky, December 2002. Thesis: Synthesis and Characterization of Multi-Wall Carbon Nanotube/Polyacrylonitrile Composite Fibers and Resulting Carbon Fibers

Bachelor of Science, Chemistry, Georgetown College, May 1999.

PROFESSIONAL POSITIONS

2000-2000 **Engineering co-op** student/engineer at Lexmark International, Lexington, Kentucky.

2000-2001 **Teaching assistant / research assistant** at The University of Kentucky and The Center for Applied Energy Research (CAER).

2001-2002 **Research Assistant**, Chemical and Materials Engineering Department and CAER, University of Kentucky, Lexington, KY.

2002-2007 **Engineer Associate II**, CAER, University of Kentucky, Lexington, KY.

PUBLICATIONS

1. Andrews, R.; **Weisenberger, M.C.**; Qian, D.; Meier, M.: Cassity, K.; Yeary, P. "Carbon Nanotubes: Multiwall Carbon Nanotubes" <u>Nanomaterials: Inorganic and Bioinorganic Perspectives.</u>, Charles M. Lukehart and Robert A. Scott, Editors. Part of <u>The Encyclopedia of Inorganic Chemistry</u>, John Wiley & Sons, Ltd. (Submitted for publication 2007)

2. **Weisenberger, M.C.**; Andrews, R.; Rantell, T. "Carbon Nanotube Polymer Composites: Recent Developments in Mechanical Properties" <u>Physical Properties of Polymers Handbook 2nd Ed.</u>, James E. Mark Editor. Chapter 35. Springer (2007)

3. Andrews, R.; **Weisenberger, M. C.** "Carbon nanotube polymer composites," Current Opinion in Solid State and Materials Science, 18(1) 31-37, 2004.

4. **Weisenberger, M.C.**; Grulke, E.A.; Jacques, D.; Rantell, T.; Andrews, R. "Enhanced mechanical properties of polyacrylonitrile/multiwall carbon nanotube composite fibers," Journal of Nanoscience and Nanotechnology, 3(6) 535-539, 2004.

5. **Weisenberger, M.C.** "Synthesis and Characterization of Mulit-Wall Carbon Nanotube / Polyacrylonitrile Composite Fibers and Resulting Carbon Fibers"

2002 University of Kentucky, Master's Thesis

PRESENTATIONS
Weisenberger M.C., Meier M, Andrews R. "Developments in Nanotube Reinforced Carbon fiber", SAMPE Fall 2007 Conference, October 29-November 1, Cincinatti, OH, Proceedings (ITAR), 2007

Marrs B, **Weisenberger M.C.**, D Bortz. "Fatigue Performance of Multiwall Carbon Nanotube – Polymer Composites," Carbon 2007 Conference, July 15-20, Seattle, WA, Proceedings, 2007.

Meier M, Andrews R, Cassity K, **Weisenberger M.C.**, Yeary P, "Functionalized Carbon Nanotubes for Composite Materials" Carbon 2007 Conference, July 15-20, Seattle, WA, Proceedings, 2007.

Martin-Gullon I, Vera-Agullo J, Varla H, **Weisenberger M.C.**, Andrews R, Qian D, Merino C. "Structural Changes Versus Graphitization Temperature For Stacked-Cup Carbon Nanofibers" Carbon 2007 Conference, July 15-20, Seattle, WA, Proceedings, 2007.

Weisenberger, M.C.; Andrews, R.; Jacques, D.; Rantell, T; Grulke, E.; Meier, M. "MWNT Reinforcement of PAN-based carbon fibers," Carbon 2004 Conference, July 11-16, Providence, RI, Proceedings, 2004.

INVITED PRESENTATIONS
Weisenberger M.C., Meier M, Andrews R. "Developments in Nanotube Reinforced Carbon fiber", Nanotailored Carbon Fiber Interchange Meeting, November 6-7, Dayton, OH, 2007

Weisenberger M.C., "High Strength Multifunctional Carbon Nanotube-Reinforced Composites for Advanced Composite Missile Structures", Workshop on *Reconfigurable Systems, Microsystems and Nanotechnology,* Bob Jones Auditorium at the Sparkman Center Redstone Arsenal, Alabama, May 8, 2007